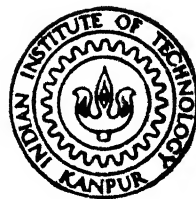


**STUDIES ON HYPERFINE STRUCTURE OF La,
RYDBERG SPECTRA OF Cs AND FINE
STRUCTURE OF La AND Eu USING
LASER OPTOGALVANIC SPECTROSCOPY**

by

J. GOVINDARAJAN



DEPARTMENT OF PHYSICS

INDIAN INSTITUTE OF TECHNOLOGY, KANPUR

JULY, 1987

PHY

1987

D

GOV

STU

**STUDIES ON HYPERFINE STRUCTURE OF La,
RYDBERG SPECTRA OF Cs AND FINE
STRUCTURE OF La AND Eu USING
LASER OPTOGALVANIC SPECTROSCOPY**

A Thesis Submitted
In Partial Fulfilment of the Requirements
for the Degree of

DOCTOR OF PHILOSOPHY

by

J. GOVINDARAJAN

to the

DEPARTMENT OF PHYSICS

INDIAN INSTITUTE OF TECHNOLOGY, KANPUR

JULY, 1987

10
535.24

- 9 NOV 1989

LIBRARY
106276

PHY-1987-D-GOV-STU

22

CERTIFICATE

Certified that the work "Studies on Hyperfine Structures of La, Rydberg States of Cs and Fine Structure of La and Eu using Laser Optogalvanic Spectroscopy" presented in this thesis has been carried out by Mr. J. GOVINDARAJAN under my supervision and the same has not been submitted elsewhere for a degree.


(G.N.Rao.)

Thesis Supervisor

Deptt. of Physics

I.I.T., KANPUR-208016

Kanpur

July, 1987.

ACKNOWLEDGEMENTS

The completion of this thesis work was possible by the active support and contribution of a number of people. I wish to thank each and every one of them.

First, I would like to express my deep sense of gratitude to my thesis supervisor Prof.G.N.Rao for his constructive criticisms throughout the programme and whose writing skill has put into this final form the contents of my research, observations and past writings. I thank him for providing me with the latest equipment which made my journey into the field of Laser Spectroscopy so much enjoyable. I thank him once again for much patience shown to the dilatory author and for the efforts spent in helping him complete the work in a reasonable time.

It is indeed a pleasure to thank Drs.B.P.Singh, Bansilal and K.V.Rao for their interest, which was always present, in the thesis work of mine in general and the welfare of mine in particular. I also like to thank the later for lending me the much needed equipment whenever I needed them.

I am obliged to Dr.Pramila for enthusiastic assistance in analyzing the hyperfine structure data of my experiments, without whose help it would not have been possible for me to present those results in that form in such a short time.

Words are inadequate to express my gratitude for B.R.Srinivasan, S.C.Sivasubramanian, G.Ravindrakumar and P.K.Choudhary. Their contributions to the fruitfulness of my stay in I.I.T. Kanpur extend far beyond those one would expect out of colleagues, intellectual companions and friends.

I thank my laboratory colleagues Ranjit and Reddy for toiling along with me many days and nights among unpredictable lasers and moody electronic instruments. I am also thankful to them for bearing the brunt of my ill-temper patiently many a times.

I am obliged to the personnel of CELT workshop for the technical support extended to me. I thank Mr. Kuldip Singh for his contagious enthusiasm and generous assistance.

I acknowledge the help of Mr.N.V.G.Swami and Mr.Prasad of Chemical Engg. department for all the help given to me. It is also a pleasure to acknowledge the help rendered by Mr.J.N.Sharma, Mr.Bhaskaran and Mr.Sairam of Glass blowing section.

I am thankful to Prof.T.M.Srinivasan and Prof.H.S.Mani for the kindness shown to me.

I am thankful to the members of LIGHT TALK group for all the intellectual adventures into the realm of Light and Lasers.

I also wish to convey my gratitude to all my friends of Hall IV, past and present, for making my stay in I.I.T. Kanpur a pleasant experience.

It is a pleasure to acknowledge the hospitality extended by Dr.I.K.Bhat and his family, Mr.Raghuram and Ms.Pramila Raghuram during my stay in Campus.

I am extremely grateful to my friend Ashish Agarwal for helping me in my computer work. I also owe the present format of the thesis to his cheerful assistance in word processing during many long and late hours of the night.

Finally, I owe the reality of this work to my mother and father. I will for ever remain grateful for their faith in me and pride in my work.

J.Govindarajan

SYNOPSIS

In this thesis, the results of the Laser Optogalvanic Spectroscopy (LOGS) experiments conducted in the areas of Rare - earth spectroscopy, Hyperfine structure studies and the Rydberg spectroscopy are reported.

Research on rare - earth elements has been going on for almost sixty years by now. Yet the knowledge of these elements is far from complete owing to the intrinsic complexities of their energy structures and due to the experimental difficulties encountered while working with these elements. New techniques are constantly being pressed into service to gain more and more information about these elements. Increased knowledge of these elements is not only of fundamental theoretical importance but also leads to many practical benefits. Investigations of the hyperfine structures of atoms reveal the nature of interactions between the nucleus of the atom and its electrons. From these studies we can, not only measure the magnitudes and signs of the various nuclear moments but also learn more about the nature of electric and magnetic fields that exist at and near the nucleus. Another area of current spectroscopic interest is the study of highly excited atoms or the Rydberg atoms as they are called. The properties of the Rydberg atoms are very different from the atoms at low excited states. The nature of these properties fall between that of classical and quantum properties. They can be easily treated semi - classically and the deviations from the predicted semi - classical behavior gives much insight into the nature of the interactions between the valence and the core

electrons. Understanding of Rydberg atoms leads to many practical applications like frequency standards, isotope separation, single atom maser etc.

Laser spectroscopy has emerged in the past two decades as an important field for the study of atoms and molecules due to the development of stable, high intensity, narrow linewidth, very collinear, highly coherent and tunable lasers. This field has revolutionized the spectroscopy in an unprecedented manner and resulted in the development of many high resolution techniques with good sensitivity. In this thesis we used Laser Optogalvanic Spectroscopy (LOGS) techniques, where the species of interest, in the form of an electric discharge, absorbs laser light and the resonance transitions of the species are detected by the change in the discharge impedance. In these experiments the high resolution is achieved due to the narrow linewidth of the laser used and the high sensitivity is obtained due to the optogalvanic detection.

Laser optogalvanic experiments were conducted to record the spectra of La I, La II and Eu I. High resolution optogalvanic experiments were performed to study the hyperfine structure of different levels of the naturally occurring ^{139}La isotope. Optogalvanic experiments were also carried out to study many Rydberg states of Cesium.

The thesis begins with the Introductory chapter, where the aims of the thesis work are presented. This chapter also gives the layout of the thesis.

In Chapter II, the experimental arrangements employed for conducting experiments like Pulsed optogalvanic spectroscopy, CW optogalvanic spectroscopy and High resolution spectroscopy are described. Details of the optimization and the calibration of the different experimental setups are also given in this chapter.

Chapter III describes the LOGS work conducted on Lanthanum and Europium. We report 40 lines of La I, 7 lines of La II and 35 lines of Eu I that could be easily identified by this technique. This is the first time LOGS spectra of La and Eu has been reported over such a broad range. This chapter also points out the suitability of LOGS for the study of rare - earth elements.

In Chapter IV, the results of the high resolution work conducted to study the hyperfine structure of 14 lines of La I are presented. From these, the Nuclear magnetic dipole constant A were extracted and presented. The A values are compared with the values available in the literature wherever applicable. We report A values for about 7 levels of La I for the first time.

The final Chapter presents the results of the investigations on the Rydberg states of Cesium. We employed optogalvanic detection technique in Cesium discharge and identified the following four Rydberg series:

$$5d^2D_{3/2} \rightarrow np^2P_{1/2,3/2} \text{ for } n = 14 \text{ to } 21$$

$$5d^2D_{5/2} \rightarrow np^2P_{3/2} \text{ for } n = 16 \text{ to } 24$$

$$5d^2D_{3/2} \rightarrow nf^2F_{5/2} \text{ for } n = 10 \text{ to } 34$$

$$5d^2D_{5/2} \rightarrow nf^2F_{5/2,7/2} \text{ for } n = 10 \text{ to } 36$$

quantum defects have been calculated for $np^2P_{1/2,3/2}$ levels for $n=14$ to 24 and for $nf^2F_{5/2,7/2}$ levels for $n=10$ to 34 and the results discussed.

T A B L E O F C O N T E N T S

I. INTRODUCTION

II. LASER OPTOGALVANIC SPECTROSCOPY - EXPERIMENTAL DETAILS

II.1 INTRODUCTION

II.2 THEORY OF OPTOGALVANIC EFFECT

II.3 EXPERIMENTAL DETAILS

II.3.1. Pulsed optogalvanic spectroscopy

II.3.2. Continuous wave optogalvanic spectroscopy

II.3.3. High resolution CW optogalvanic spectroscopy

II.4. OPTIMIZATION AND CALIBRATION

II.4.1. Introduction

II.4.2. Pulsed Optogalvanic spectroscopy of neon

II.4.3. CW Optogalvanic spectroscopy of neon

II.5. CONCLUSIONS

REFERENCES

III. CONTINUOUS WAVE LASER OPTOGALVANIC SPECTROSCOPY OF LANTHANUM AND EUROPIUM

III.1. INTRODUCTION TO THE SPECTROSCOPY OF RARE - EARTHS

III.2. EXPERIMENTAL TECHNIQUES OF RARE-EARTH SPECTROSCOPY

III.3. SPECTROSCOPY OF LANTHANUM

III.3.1. Energy Levels of La I and La II

III.3.2. Experimental procedure

III.3.3. Results and Discussion

III.4. SPECTROSCOPY OF EUROPIUM

III.4.1. Energy Levels of Eu I

III.4.2. Experimental procedure

III.4.3. Results and Discussion

III.5. CONCLUSIONS

REFERENCES

IV.	HYPERFINE STRUCTURE STUDIES OF LANTHANUM	69
IV.1.	THEORY OF HYPERFINE INTERACTIONS	69
IV.1.1.	Historical sketch	69
IV.1.2.	Introduction to hyperfine interactions	70
IV.1.3.	Hfs Hamiltonian and the effective operators	71
IV.2.	HYPERFINE STRUCTURE OF La I	77
IV.3.	EXPERIMENTAL PROCEDURE	79
IV.4.	RESULTS AND DISCUSSION	80
IV.5.	CONCLUSIONS	106
	REFERENCES	107
V.	STUDY OF RYDBERG STATES OF ATOMIC CESIUM	109
V.1.	INTRODUCTION	109
V.1.1.	Rydberg states and Rydberg spectroscopy	109
V.1.2.	Experimental techniques of Rydberg spectroscopy	111
V.1.3.	Theoretical framework for the analysis of Rydberg spectra	115
V.1.4.	Rydberg spectroscopy of cesium	121
V.2.	EXPERIMENTAL	122
V.2.1.	Experimental Arrangement	122
V.2.2.	Glow discharge lamp construction	123
V.2.3.	Experimental Procedure	127
V.3.	RESULTS AND DISCUSSION	128
V.4.	CONCLUSIONS	139
	REFERENCES	140

LIST OF TABLES

II.1	Specification of the nitrogen lasers employed in the experiments.	12
II.2	Specification of the pulsed dye laser employed for the experiments.	16
II.3	Specification of the Spectra physics Model No. 380D Ring dye laser.	28
II.4	Results of pulsed OGS of Neon	32
II.5	Unidentified lines in the OGS of Ne.	35
II.6	Results of CW OGS of Neon.	38
II.7	Calculated saturation parameters for some transitions of Neon and Lanthanum.	47
III.1	Melting and Boiling Temperatures of rare-earth elements.	52
III.2	Transitions of LaI by optogalvanic spectroscopy.	57
III.3	Transitions of LaII by optogalvanic spectroscopy.	59
III.4	Transitions of EuI by optogalvanic spectroscopy.	63
IV.1	List of transition of LaI for which hfs is studied.	81
IV.2	Comparison of observed CW relative O.G. intensities with relative theoretical intensities of some of the hfs components of 574.441 nm and 576.997 nm transitions of LaI.	85

IV.3	Experimental A Constants (in MHz) for lower levels of some transitions of ^{139}La .	99
IV.4	Experimental A constants (in MHz) for upper levels of some transitions of ^{139}La .	101
IV.5	Pertinent data for hfs components of the transition $^4\text{P}_{3/2} \rightarrow ^4\text{S}_{3/2}$ (582.972 nm) shown in Fig IV.9.	103
IV.6	Pertinent data for hfs components of the transition $J'' = 5/2 \rightarrow J' = 7/2$ (near 584.8 nm) shown in Fig IV.10.	105
V.1	Properties of Rydberg atoms and their dependence on 'n'.	110
V.2	Neon calibration lines.	130
V.3	Transitions classification chart.	132
V.4	Wavenumbers (cm^{-1}), Effective quantum number (n^*) and Quantum Defects (δ) of $n^2\text{P}_j$ levels.	136
V.5	Wavenumbers (cm^{-1}), Effective quantum number (n^*) and Quantum Defects (δ) of $n^2\text{F}_j$ series of cesium.	138

LIST OF FIGURES

II.1	Pulsed optogalvanic experimental arrangement.	11
II.2	Molelectron model no. DL200 Hansch type dye laser.	14
II.3	CW optogalvanic spectroscopy setup.	18
II.4	Spectra physics model 375A CW jet stream dye laser.	19
II.5	High resolution Doppler limited OGS experimental arrangement.	22
II.6	SP380D Ring Dye Laser.	23
II.7	Single frequency selection in ring dye laser.	25
II.8	Frequency locking of laser to external etalons.	27
II.9	Optogalvanic spectrum of Neon.	31
II.10	Part of the optogalvanic spectrum of hollow cathode Europium/Neon spectral lamp.	37
II.11	Variation of optogalvanic signal with lamp current.	41
II.12	Variation of optogalvanic signal with laser	43
III.1	Part of the optogalvanic spectrum of hollow cathode Lanthanum/Neon spectral lamp.	55
III.2	Part of the optogalvanic spectrum of hollow cathode Europium/Neon spectral lamp.	62

IV.1	Sketch of the fine structure level scheme of the La I Spectrum.	83
IV.2	Hyperfine level scheme and theoretical hfs of the La I line $\lambda=574.441$ nm.	87
IV.3	Recorded hyperfine structure of 574.441 nm transition of La I.	88
IV.4	Hyperfine level scheme and the theoretical hfs of the La I line $\lambda=585.558$ nm.	89
IV.5	Recorded hyperfine structure of 585.558 nm transition of La I.	90
IV.6	Hyperfine level scheme and theoretical hfs of the La I line $\lambda=579.134$ nm.	91
IV.7	Recorded hyperfine structure of 579.134 nm transition of La I.	92
IV.8	Hyperfine level scheme and theoretical hfs of the La I line $\lambda=582.972$ nm.	93
IV.9	Recorded hyperfine structure of 582.972 nm transition of La I.	94
IV.10	Recorded hyperfine structure of some transition of La I near 584.8 nm.	95
IV.11	Recorded hyperfine structure of 576.997 nm transition of La I.	96
IV.12	Recorded hyperfine structure of 582.199 nm transition of La I.	97
V.1	Optical excitation of various Rydberg states.	113
V.2	Partial energy diagram of Cesium.	113

V.3	Experimental setup for Cesium optogalvanic spectroscopy.	124
V.4	Cesium discharge cell.	125
V.5	Schematic of Cesium filling station.	126
V.6	Optogalvanic spectrum of Cs/Ne discharge.	129
V.7	$5d^2D_{5/2} \rightarrow nf^2F_{5/2,7/2}$ and $5d^2D_{3/2} \rightarrow nf^2F_{5/2}$ series of Cesium.	139

CHAPTER I

INTRODUCTION

Atomic Spectroscopy contributed quite significantly to our knowledge on the structure of atoms and molecules and provided the base to test quantum mechanics.

The spectra of Hydrogen and alkali atoms are relatively easy to explain. However, as the number of electrons in the valence shell increases, the spectra become highly complicated owing to the vast number of electronic configurations, energy levels and the enormous number of allowed transitions that become possible. Examples of such complex spectra are the spectra of transition elements, rare earth elements and elements of actinide group of the periodic table. Spectra of rare earth elements have not been fully explained satisfactorily even at present. Newer and newer techniques are constantly pressed into service to acquire better and better rare-earth spectra. Rare-earth spectroscopy is currently a very active area of research.

Another area of Spectroscopy where vigorous research is still going on is the study of hyperfine interactions and isotope shifts in atoms and molecules. The fine structure of energy levels of atoms can be explained by the interaction between the orbital motion and the intrinsic spin of electrons. The still finer structure to these fine structures called Hyperfine Structure (HFS), is attributed to the interaction between fields produced by the electrons and the electric and magnetic moments of the nucleus. Hence study of hyperfine structures not only

helps in measuring the nuclear spins and moments but also helps in gaining knowledge about the nature of the hyperfine fields that are present at the nuclei. In multi-isotopic elements there are relative shifts of fine and hyperfine lines in different isotopes called Isotope Shifts (IS). These are due to the differences in masses, sizes and shapes of nuclei in different isotopes. Hence isotope shift studies reveal the changes in the shapes of the nuclei of different isotopes. These changes are primarily due to the differences in proton charge distribution in different isotopes.

Another emerging area of spectroscopy, called Rydberg Spectroscopy, is the study of atoms with their valence electrons in highly excited states. The properties and behavior of these atoms are very different from that of the atoms in low excited states. Though these large and fragile atoms with strange properties are difficult to produce and maintain, they are very simple to treat theoretically. Even semiclassical treatments using a few parameters like quantum defect seem to account many of their properties. The deviations from this semiclassical behavior give much insight into the nature of the interactions between the valence electrons and the core electrons.

This thesis reports the results of the experimental work carried out in all the three areas of spectroscopy mentioned above.

Though optical spectroscopy is a very old branch of science it is still a very active area of research due to the development of many new instruments, new methods and new techniques. One of the instruments which made a great impact on the spectroscopy is

the Laser. The development of very intense, highly monochromatic, exceedingly collinear, extremely coherent and broadly tunable lasers with good frequency and intensity stabilization has revolutionized the field of spectroscopy in an unprecedented way. Because of these developments a new branch of spectroscopy called Laser Spectroscopy has come into existence in the past few decades. Also making use of lasers, many high resolution techniques like saturation spectroscopy, two photon spectroscopy, fast beam spectroscopy, etc. have been developed. Simultaneously high sensitive detection techniques like optogalvanic spectroscopy and field ionization have emerged.

In this thesis, Laser optogalvanic spectroscopic experiments conducted to extract the fine structure of rare-earth elements lanthanum and europium; high resolution experiments conducted to obtain hyperfine structure of some transitions of Lanthanum I; optogalvanic Rydberg spectroscopic experiments carried out to study the Rydberg states of Cesium are reported.

Chapter II of the thesis describes the different experimental arrangements employed for conducting Laser optogalvanic spectroscopy. It also presents the experiments on neon to optimize and calibrate these experimental setups.

In chapter III the optogalvanic experiments conducted on La I, La II and Eu I are presented. The aim of the experiments conducted was to judge the suitability of laser optogalvanic spectroscopy for the elucidation of rare-earth spectra. This chapter presents the results and discussion of these experiments.

The High Resolution Optogalvanic Spectroscopy experiments conducted on some transitions of La I to study the Hyperfine Structure and the results obtained are presented in chapter IV. Here the resulting spectra is presented and analyzed. This chapter also gives the Nuclear magnetic dipole constants (A 's) of the levels of the transitions studied. Comparison with previously reported values is given wherever applicable.

Chapter V describes the Rydberg spectroscopy experiments conducted to study some Rydberg levels of Cesium. By analyzing the spectra four Rydberg Series were identified. From the series identified, term values, effective quantum numbers and quantum defects of a number of Rydberg states of cesium are presented.

C H A P T E R I I

LASER OPTOGALVANIC SPECTROSCOPY - EXPERIMENTAL DETAILS

II.1 INTRODUCTION

A variety of lasers developed in the past two decades have revolutionized the field of spectroscopy. High spectral densities of presently available continuous wave (CW) lasers have enabled many weak transitions to be detected. This has also ushered in many new non-linear spectroscopic techniques, like, saturation and multiphoton spectroscopy. High degree of collinearity of the lasers helps in achieving long interaction paths between the laser beams and atoms. This has improved the detection sensitivity in a dramatic way. The available narrow linewidth lasers have improved the selectivity of the levels studied. Advent of tunable lasers has brought many a new solutions to old problems. Presently highly stable, single frequency, high intensity, and tunable CW lasers are available which can operate in a broad wavelength range from UV to IR. Presently pulsed lasers with very high peak power and extremely short pulse width are also available. These lasers are employed whenever very high sensitivity or very good time resolution are needed.

In laser spectroscopy, absorption of laser radiation by an atomic sample of interest is detected. Usually this is done by monitoring the fluorescence emitted by the sample. Though this is a very sensitive technique, it is not convenient all the time. For example in discharge studies, the fluorescence of interest is generally drowned in very high background light. Good

filtering techniques are needed to extract the signal. In cases like this some other ways of detecting light absorption is employed. Optogalvanic detection is one such method.

Optogalvanic spectroscopy (OGS) is based on the Optogalvanic effect (OGE) , which is the change in the impedance of a discharge due to resonant light absorption. This technique of detection is simple and convenient when the sample to be investigated is in the form of a discharge. Absorption of resonant light perturbs the populations of different atomic and ionic levels of the discharge. Since each level has different ionization probability, these population changes inturn vary the total ionization of the discharge. This is monitored by the current or voltage change in the external circuit. OGE is a well developed detection technique in the field of spectroscopy [1-2].

All the experimental setups in this thesis employed optogalvanic detection for the following reasons,

(1) In the low resolution setup for Lanthanum and Europium spectroscopy it was easier to sputter these elements in a discharge than to use an oven to get enough vapour pressure to conduct experiments. Since the sample was in the form of discharge it was convenient to detect the absorption of laser radiation by OGE than by any other method.

(2) For the high resolution spectroscopy of lanthanum OG detection method was retained for the same reason.

(3) In the experiments conducted to study the Rydberg states of cesium the fluorescence yield from the Rydberg levels to lower levels is small. Besides , the transitions studied were

from the excited states and not from the ground state. These excited levels are well populated in a discharge. Hence Rydberg spectroscopy of cesium was also studied employing OG detection technique.

II.2. THEORY OF OPTOGALVANIC EFFECT

Optogalvanic effect has been known for more than five decades [3-8]. Experiments have been conducted on this effect by the name of Joshi effect from times as early as 1944 [9-10]. Systematic use of this effect for absorption spectroscopy was started by Roumanian researchers in 1964 [11]. This effect was demonstrated as a simple and efficient detection technique for laser spectroscopy by Green et al. [12] in 1976, where they have coined the name Optogalvanic effect. Smyth and Shenck [13] had tried to explain the magnitudes and signs of the optogalvanic signals. However a full explanation of this effect will require simultaneous solutions of plasma, rate and Maxwells equations. One such attempt was made by Pepper [14] by assuming rate analysis approach and modified Schottky approximation for the glow discharge. It was pointed out there that the model proposed failed to explain the change of sign or time evolution of the signal. In 1979 Eraz et al. [15] have presented a simplified phenomenological theory of the optogalvanic effect. This theory could explain the relative magnitudes, sign changes and time evolutions of the signals qualitatively.

Eraz et al. [15] considered a D.C. discharge tube in series with a ballast resister, with the pressure of the buffer gas and the current in the tube corresponding to a positive internal tube

resistance. A multiplication factor α was defined as the number of electrons arriving at the anode, by avalanche, for each electron emitted by the cathode. For steady state $\alpha = 1$. If $\alpha > 1$ current in the tube increases. This causes more voltage drop across the ballast resistor, which in turn decrease the value of α . In this way α is self regulated. If $\alpha < 1$, current decreases, and the reverse happens to regulate the α . In an OG experiment the laser beam illuminates the discharge region through which these electrons flow. In small signal domain, which is mostly the case, $\alpha = 1$ and $d\alpha = 0$. Now $d\alpha$ can be written as,

$$d\alpha = (\delta\alpha/\delta V)_{n_i} \Delta V + \sum_j (\delta\alpha/\delta n_i)_{V, n_j, j \neq i} \Delta n_i = 0 \quad \text{-----(1)}$$

where,

- V = Voltage across the tube
 ΔV = The optogalvanic signal which is the deviation of the above voltage from its steady state value
 n_i = Population of the i^{th} level of the atomic/ionic species of the discharge
 Δn_i = Deviation of the above population from its steady state

now equation - (1) can be written as ,

$$\Delta V = -\beta \sum_i a_i \Delta n_i \quad \text{-----(2)}$$

where ,

$$\beta = (d\alpha / dV)_{n_i}^{-1} \quad \text{-----(3)}$$

$$a_i = (\delta\alpha / \delta n_i)_{V, n_j} \quad \text{-----(4)}$$

Qualitatively it can be deduced that β and a_i are always > 0 and generally when $E_i > E_j$, a_i is greater than a_j . The rate of change of population can now be written as,

$$d(\Delta n_i)/dt = \sum_j \gamma_{ij} \Delta n_j - \sum_j (n_i - n_j) \sigma_{ij} I_{ij} \quad \text{---(5)}$$

where,

γ_{ij} = Rate coefficient for $i \rightarrow j$ transition without illumination

$\sigma_{ij} = (\sigma_{ji})$ = Optical cross section of transition from $i \rightarrow j$

If the laser frequency is assumed to be monochromatic and at some resonance frequency $1 \rightarrow 2$, then

$$d(\Delta n_1)/dt = \sum_j \gamma_{j1} \Delta n_j - (n_1 - n_2) \sigma_{12} I_{12} \quad \text{---(6a)}$$

$$d(\Delta n_2)/dt = \sum_j \gamma_{j2} \Delta n_j - (n_2 - n_1) \sigma_{12} I_{12} \quad \text{---(6b)}$$

Now all the other levels can be collectively treated as a bath with a characteristic energy relaxation time T_1 . With this assumption equations (6a) and (6b) become

$$d(\Delta n_1)/dt = \Delta n_1/T_1 - (n_1 - n_2) \sigma_{12} I_{12} \quad \text{---(7a)}$$

$$d(\Delta n_2)/dt = \Delta n_2/T_2 - (n_2 - n_1) \sigma_{12} I_{12} \quad \text{---(7b)}$$

The above equations can be used to deduce the behaviour of the OG signal ΔV for various modes of laser illuminations. In the case of CW laser illumination, $d(\Delta n_1)/dt = 0$ and this leads to a condition,

$$\Delta V = -\beta \sigma_{12} I_{12} \frac{(a_2 T_2 - a_1 T_1)}{(n_2 - n_1)} \quad \text{---(8)}$$

If $E_1 < E_2$ then $n_1 > n_2$ and $a_2 > a_1$. From this the following deductions can be made,

(1) The optogalvanic signal ΔV is always negative unless $a_1 T_1 > a_2 T_2$. For metastable states it may so happen that $a_1 T_1$ becomes greater than $a_2 T_2$. This can make the signal positive. Relaxation times T_1 and T_2 are very sensitive to the plasma conditions, which are controlled by the pressure and the current of the tube which in turn may change the sign of OG signal.

(2) In the small signal limit OG signal is proportional to $(n_1 - n_2)$ and $\sigma_{12} I_{12}$. Hence when σ_{12} saturates ,OG signal also saturates.

(3) The time profile of ΔV is the same as that of I_{12} . In CW experiments it is usual to chop the laser beam to permit phase sensitive detection of the OG signal to avoid discharge noise.

II.3. EXPERIMENTAL DETAILS

In the work reported in this thesis three different types of experimental arrangements were used. The first one to be described is the setup for Pulsed Optogalvanic Spectroscopy. This was used to conduct experiments on neon discharge. The second being the set up for CW Optogalvanic Spectroscopy experiments. Using this setup investigations were done on neon, lanthanum and europium discharges. A similar experimental arrangement was used to conduct experiments on Rydberg Spectroscopy of Cesium. The last setup described in this section is for conducting High Resolution Optogalvanic experiments of lanthanum.

II.3.1. Pulsed Optogalvanic Spectroscopy

Experimental arrangements for the pulsed optogalvanic spectroscopy is shown in Fig II.1. In these experiments a nitrogen laser pumped dye laser was used as the source of tunable, narrow linewidth light. The nitrogen laser used was either a Molectron Model No UV1000 laser or a Molectron Model No UV12 laser. The specifications of these lasers , which emit 337.1 nm UV pulses of 10 nsec width are given in Table II.1. Dye

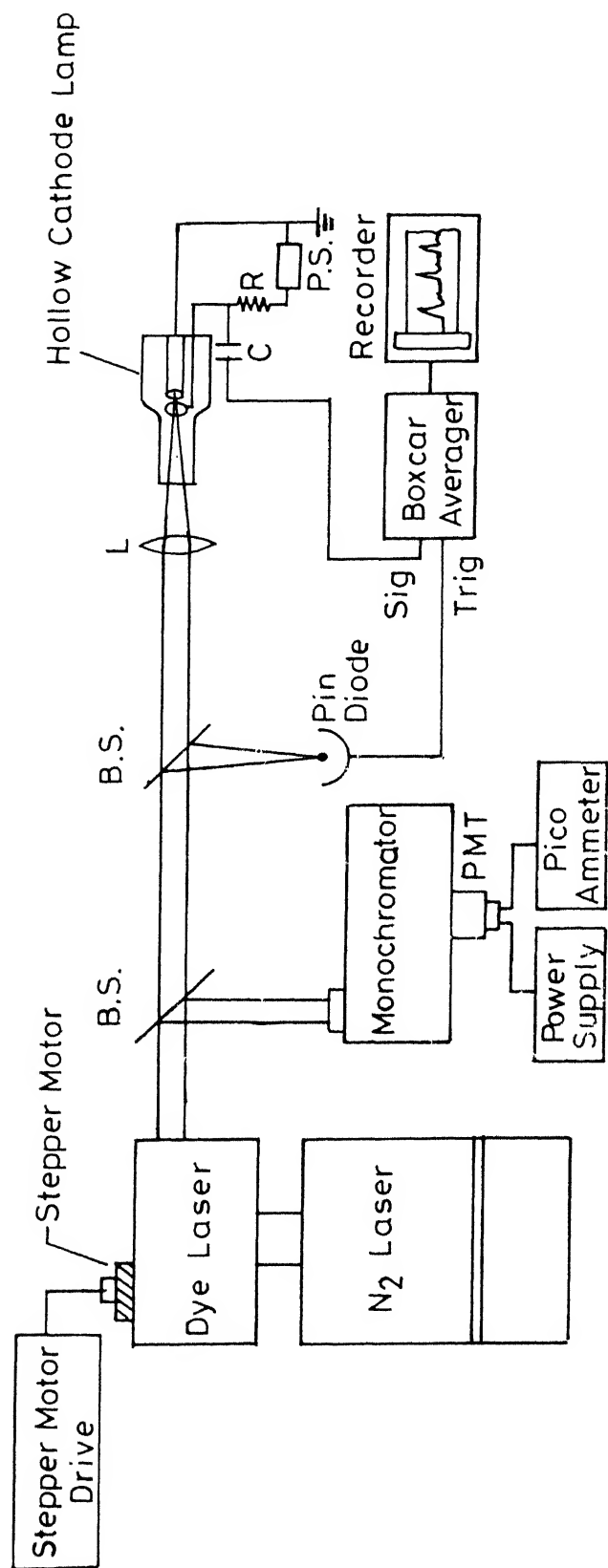


Fig.II.1 Pulsed optogalvanic experimental arrangement.

Table II.1

Specifications of the nitrogen lasers employed in the experiments

	UV1000	UV12	Units
Wavelength of lasing	331.7	331.7	nm
Peak output power	1000	250	kW
Average power	250	90	mW
Pulse width	10	10	ns
Repetition rate	1 - 50	1 - 50	Hz
Beam dimensions	6 x 25	6 x 25	mm
Beam divergence	1 x 7	1 x 7	mrad
Stability	± 5	± 5	%

lasers are tunable. They use some organic dye as a gain medium. Many organic dyes have more than 1000 cm^{-1} wide absorption and emission bands. The emission bands are shifted towards the larger wavelengths compared to the absorption bands. Lasing action takes place between singlet levels of these molecules. These molecules also have triplet levels. When a molecule is excited to a triplet state it stays there for a long time. Hence, triplet levels quench the lasing action or degrade the gain of the medium. To prevent the build up of population in the triplet states either the dye should be pumped by a very short light pulse or the dye should be circulated or stirred.

In the experiments conducted either a Molelectron Model No DL 200 or a Molelectron Model No DL 12 was used tunable dye laser was used. These are side pumped Hansch type dye lasers [16]. Schematic of this types of laser is given in Fig II.2. The dye is kept in a magnetically stirred cuvette. The UV beam of the N_2 laser is focused by an aspheric lens into this dye cell. Laser cavity is formed by a reflection grating at one end and a low reflection mirror at the other end. The grating acts as a wavelength selector besides acting as the end reflector. A beam expander is introduced between the dye cuvette and the grating to illuminate more lines of the grating. This further narrows the linewidth of the laser. Introduction of the beam expander also increases the laser output power. The beam expanders used in the two types of the lasers were different. DL 200 uses an achromatic telescope as the beam expander. The magnification of this beam expander is 22.5 X. Model DL 12 uses a multiprism beam expander

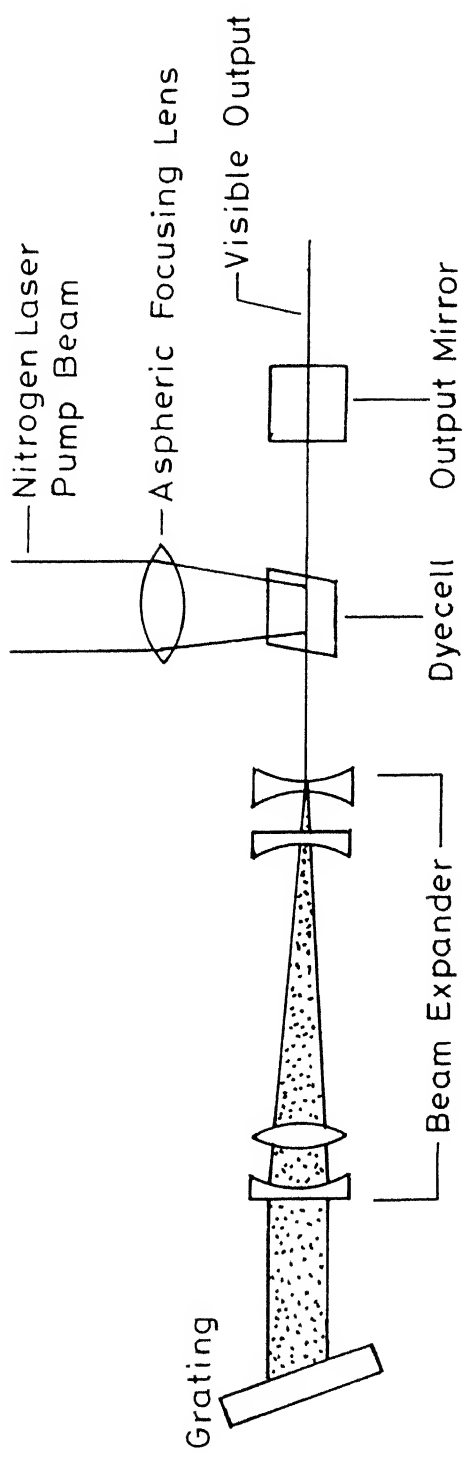


Fig.II.2 Molelectron model no. DL 200 Hänsch type dye laser

of magnification 40 X. Prism beam expanders have some advantages over telescopic beam expanders. In the former case, the beam is expanded only in the direction perpendicular to the grooves of the grating and its tilt axis. Hence in this type of lasers grating tilt is less of a problem. This type of beam expanders shorten the laser cavity length. Besides the output beam is polarized.

Tuning of the laser is achieved by rotating the grating around its axis. In both the models this is accomplished by a sine drive assembly. This mechanism converts the linear motion of the hand crank to the sine function response of the grating. The result is a linear relationship between the hand crank rotation and the wavelength increment of the dye laser output. In the experiments conducted the hand crank was rotated by a stepper motor which was controlled by a stepper motor drive. The output specifications of these dye lasers are given in Table II.2. The output power of the laser was measured by a Scientech model no. 362 calorimetric power meter.

In the experimental setup one small part of the laser beam was directed to a SPEX model no. 1402 double monochromator for monitoring the wavelength of the dye laser. The wavelength accuracy of the monochromator was 0.003 nm. Its entrance and exit slits were adjusted to 100 μm . An FW 130 photomultiplier tube (PMT) was attached to its exit slit. The output current of the PMT was measured by a Keithley model no. 417 picoammeter. Other small part of the laser beam was directed to an RCA 30808 PIN diode for trigger signal generation. The main part of the laser beam was directed coaxially into a hollow cathode lamp. In the

Table II.2

Specifications of the pulsed dye lasers employed for the experiments

	DL200	DL12	Units
Fundamental tuning range	360 - 750	360 - 950	nm
Laser linewidth	0.01	0.01	nm
Energy conversion efficiency	12.5	6.0	%
Peak output power (at 580 nm and 1 MW pump power)	125	60	kW
Pulse duration	5 - 7	5 - 7	ns
Stability	± 5	± 10	%
Beam diameter	0.5	0.3 - 0.5	mm
Beam divergence	1.5	1.0	mrad
Beam polarization	Unpolarized	Linear	

lamp the discharge was struck by a Fluke model no. 407D high voltage power supply. This supply could generate a maximum voltage of 600 VDC at a current of 350 mA. The ripple and other noise of the power supply was less than 0.05 mV. The ballast resistor is of 25 k Ω and the signal was picked off by a 0.01 μ F DC blocking capacitor. It was found that averaging was necessary to obtain good signal to noise ratio. This was accomplished by a PAR model no. 160 Boxcar averager. Boxcar averagers sample signal for a short time called Aperture Time (AT) a short time after the reception of the trigger, called Delay Time (DT). By repetitively sampling this portion and averaging in a capacitor, noise which is random, is averaged and signal extracted. During the experiments the laser scan speed, trigger point, DT and AT are optimized to get the maximum signal to noise ratio.

II.3.2. Continuous Wave Optogalvanic spectroscopy

The experimental arrangement used is shown in Fig II.3. The light source used for these experiments was an Argon ion laser pumped CW jet stream dye laser. The pump laser used was a Spectra Physics model no. 2020 Argon ion laser, which was capable of generating 5 Watts of all line power. Generally 3 Watts of pump power was used. The narrow band tunable dye laser used was a Spectra Physics model no. 375A CW dye laser. Schematic of this laser is given in Fig II.4. Rhodamine 6G dye in a solution of methanol and ethylene glycol was circulated by a high pressure pump and was formed into a thin homogeneous jet inside the laser by a well machined nozzle. The pump beam, which was focused by the mirror M_p on this jet, excites these dye molecules. A folded

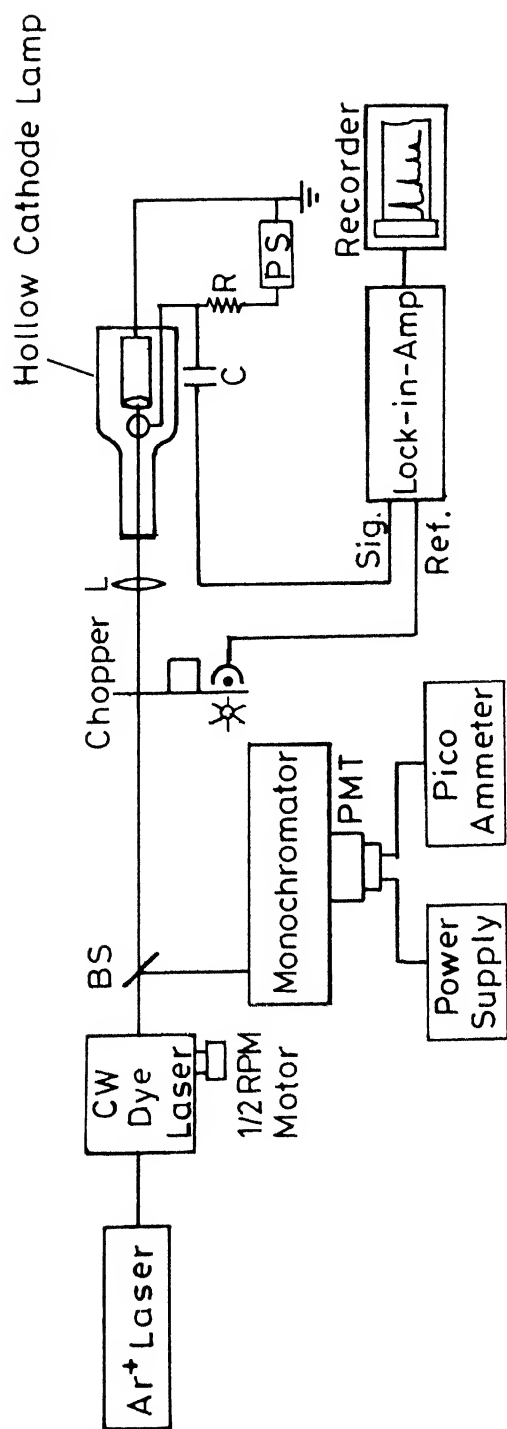


Fig.II.3 CW optogalvanic spectroscopy setup.

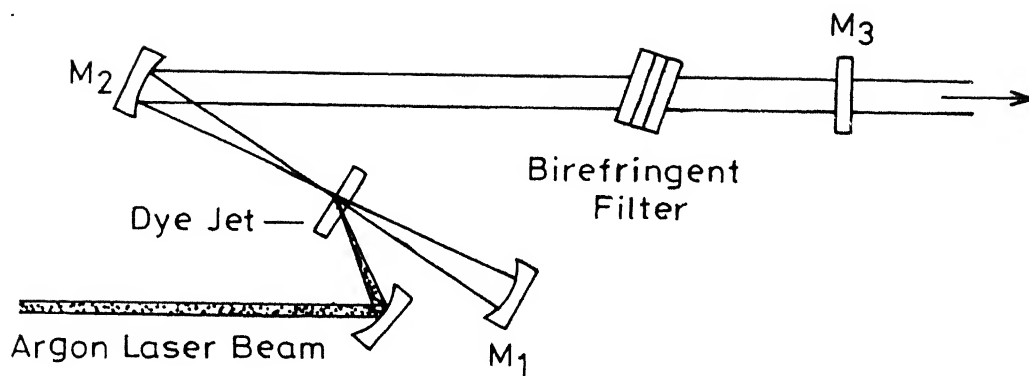


Fig.II.4 Spectra physics model 375A CW jet stream dye laser.

cavity was formed by the high mirror M_1 ($f=5\text{cm}$), the folding mirror M_2 ($f=5\text{cm}$), and the end mirror M_3 ($f=\infty$). These mirrors were rigidly held by holders fixed to a structure made of three invar rods. The wavelength of operation of the dye laser within the dye gain profile was selected by a three plate birefringent filter. Both the filter and the dye jet are held at Brewsters angle to the laser beam. Wavelength tuning was accomplished by tilting the filter within the cavity by a micrometer control. Smooth wavelength scanning was achieved by rotating this micrometer by a 1/2 RPM synchronous motor. The power of the output of the laser was measured by a Coherent model no. 210 light power meter. With this setup a peak output power of 300 mW could be generated in the 560 - 635 nm range. The linewidth of the laser was less than 0.05 nm or 0.3 cm^{-1} .

Wavelength of the laser was monitored by a SPEX double monochromator as described in the previous section. The main laser beam was chopped by an Ithaco model no. 222 light beam chopper to facilitate phase sensitive detection. This also generates a synchronous reference signal. This chopped beam was focused by a lens ($f=10\text{ cm}$) into the glow discharge tube. The discharge was ignited by an Aplab model no. 7323 high voltage power supply. This well regulated power supply can give a maximum voltage of 1000 VDC and a current upto 1.0 A. A 10 ballast resistor of 10 k Ω was used. The optogalvanic signal was picked off by a 0.01 μF capacitor and was fed to a Stanford Research Inc. model no. SR510 lock-in amplifier. The reference channel was triggered by the signal from the chopper. Lock-in amplifier

amplifies only the signal at reference frequency. All the asynchronous signals, which are mostly noise, are averaged to zero. In this way a significant increase in signal to noise ratio is obtained. The output of this amplifier is fed to a strip chart recorder. Values of the ballast resistor, blocking capacitor, chopper frequency and the RC constants of the lock-in amplifier were optimized to get maximum signal to noise ratio of the recorded signal.

II.3.3. High resolution CW Optogalvanic Spectroscopy

Schematic of the experimental setup is given in Fig II.5. To record a high resolution spectrum the light source should have a very narrow linewidth. The source should also be stable in intensity and frequency and should be tunable. In the high resolution experiments conducted, an argon ion laser pumped single frequency Ring dye laser was employed. The pump laser was a SPECTRA PHYSICS model no. 171-09 argon ion laser capable of generating 18 Watts of all line power. For pumping the ring dye laser this pump laser was operated at 514.5 nm using a prism inside the cavity. It was possible to generate 4.0 to 6.0 Watts of single line output power at this wavelength. This light was used to pump a SPECTRA PHYSICS model no. 380D Ring dye laser (Fig II.6). This is a travelling wave dye laser. In contrast to the standing wave dye lasers these lasers make use of the whole of the dye medium. Hence the output power is an order of magnitude more. In these dye lasers the nodes and antinodes are absent, hence there will be no spatial hole burning in the dye medium. This also helps in preventing multimode operation of

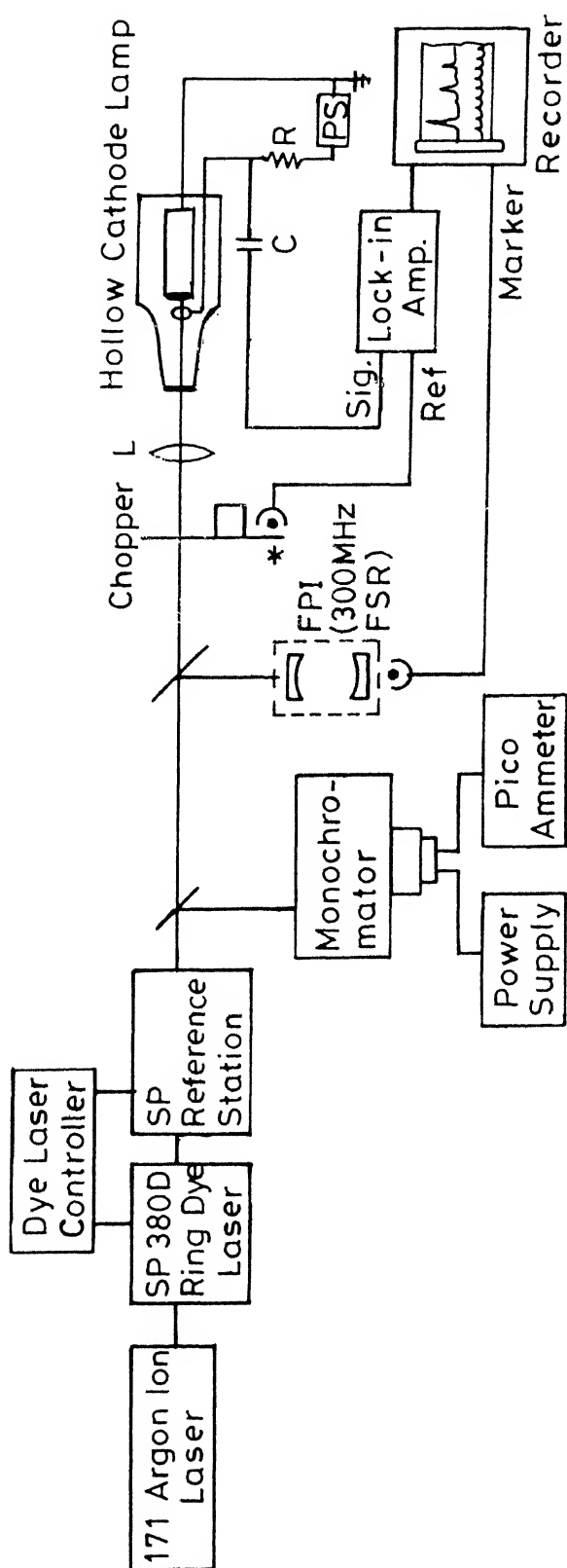
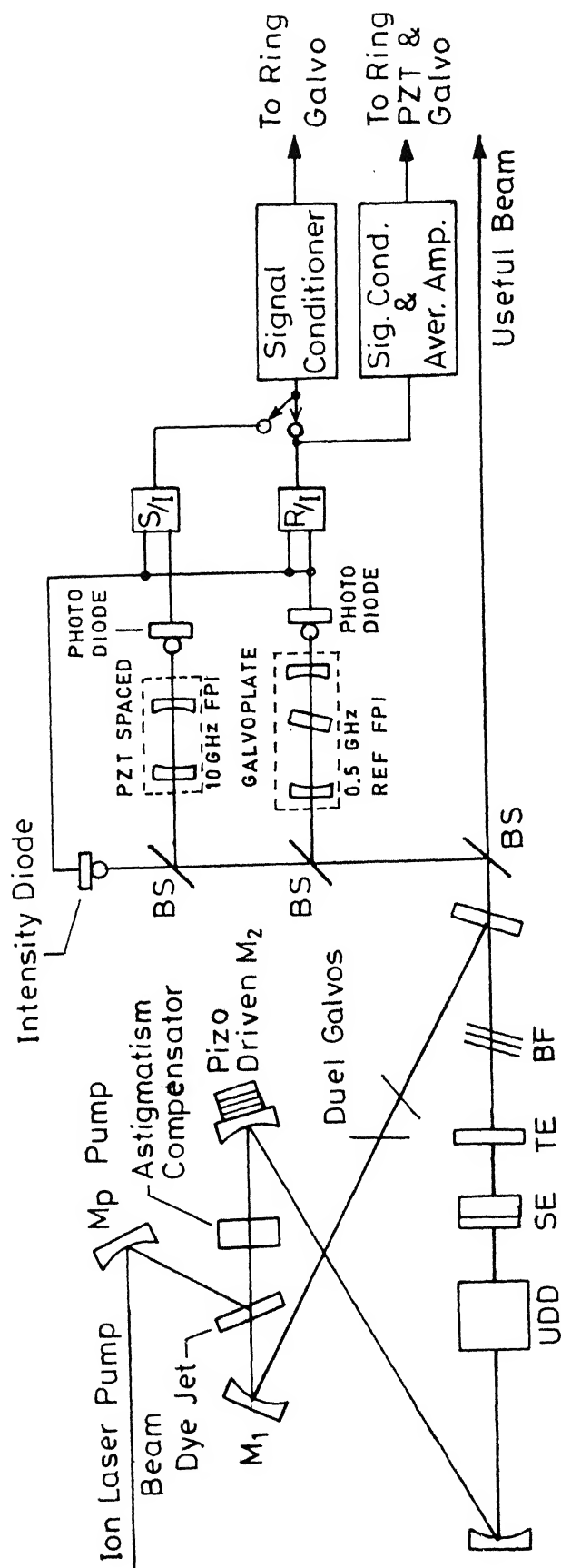


Fig.II.5 High resolution Doppler Limited OGS experimental arrangement.



UDD: Uni Directional Device

SE: Scanning Etalon

TE: Thin Etalon

BE: Birefringent Filter

BS: Beam Splitter

Fig.11.6 SP 380D Ring Dye Laser

the laser. In the ring dye laser the pump beam was focused on a vertical dye jet inside the dye laser cavity. This jet was positioned at Brewsters angle inside a folded cavity formed by mirrors M_1 ($f=3.5$ cm), M_2 ($f=10$ cm), M_3 ($f=23$ cm) and M_4 ($f=\infty$). This cavity can support two counter propagating travelling waves. One of this wave is suppressed by a unidirectional device consisting of a Faraday rotator and a quartz polarization rotator. In the laser used the cavity modes were spaced at 200 MHz apart. Since the dye gain extends to several hundred Angstroms, lasing can occur at very large number of modes. Single frequency operation is achieved by the introduction of frequency selective intercavity devices like birefringent filter, a thick etalon, and a thin etalon. Birefringent filter when introduced into the cavity selects the band of operation and helps in coarse wavelength tuning. A thick etalon of 75 GHz Free spectral range (FSR) selects one mode of these band of modes. This etalon was a plane parallel Fabry - Perot interferometer. However, the frequency of the laser may jump to an adjacent mode while scanning. To prevent this, a thin etalon of 100 μ m thickness and 900 MHz FSR is introduced into the cavity. Now the laser can be tuned by varying the optical path length of the laser. This was done by two counter rotating fused silica plates mounted at Brewsters angle in the cavity on two galvanometers. A single plate in the cavity will always cause beam walkoff. This was the reason for the introduction of two plates. While scanning the laser, the thick etalon was locked to a mode of the cavity to prevent mode hops. In this way a frequency scan of 30 GHz could be generated. Fig II.7 shows how a single frequency is selected

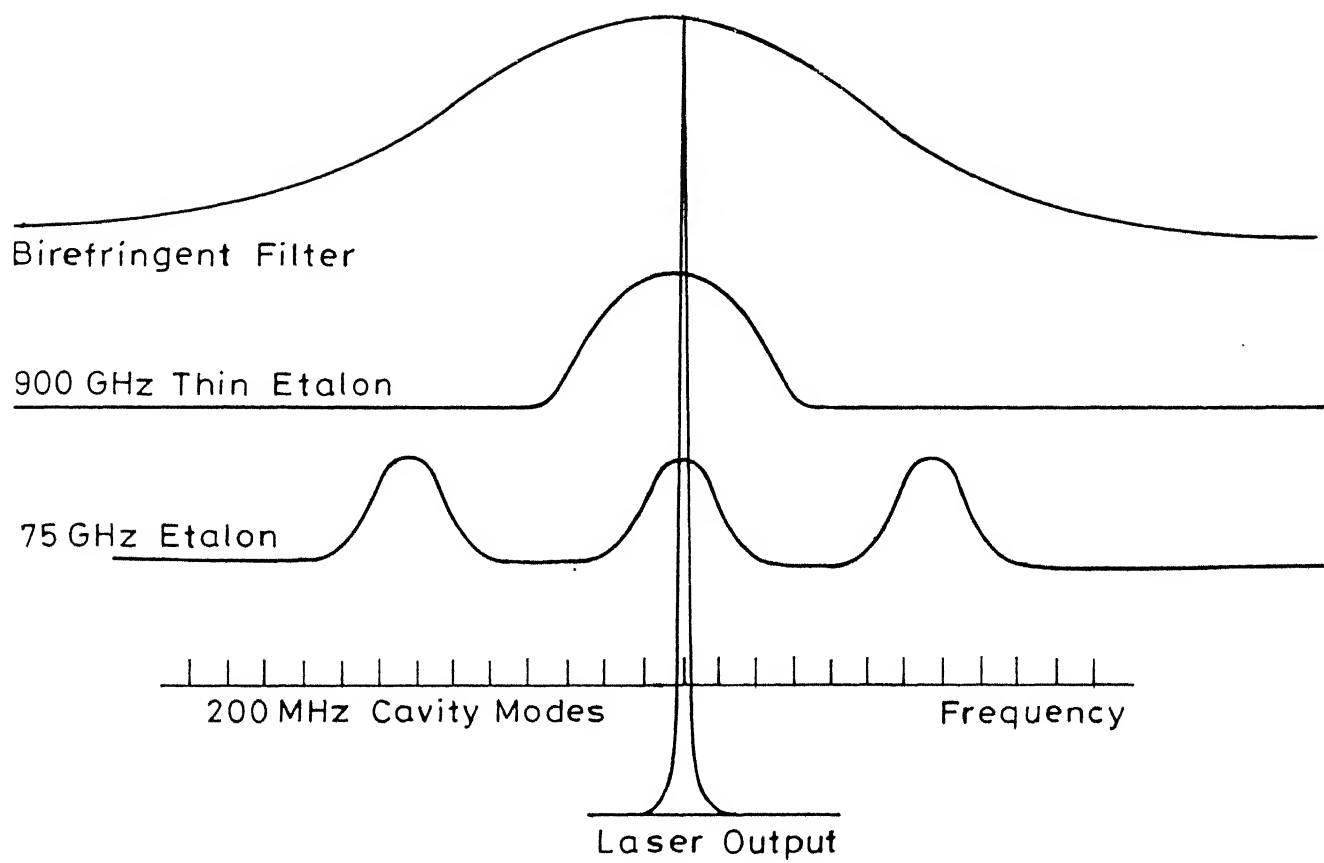
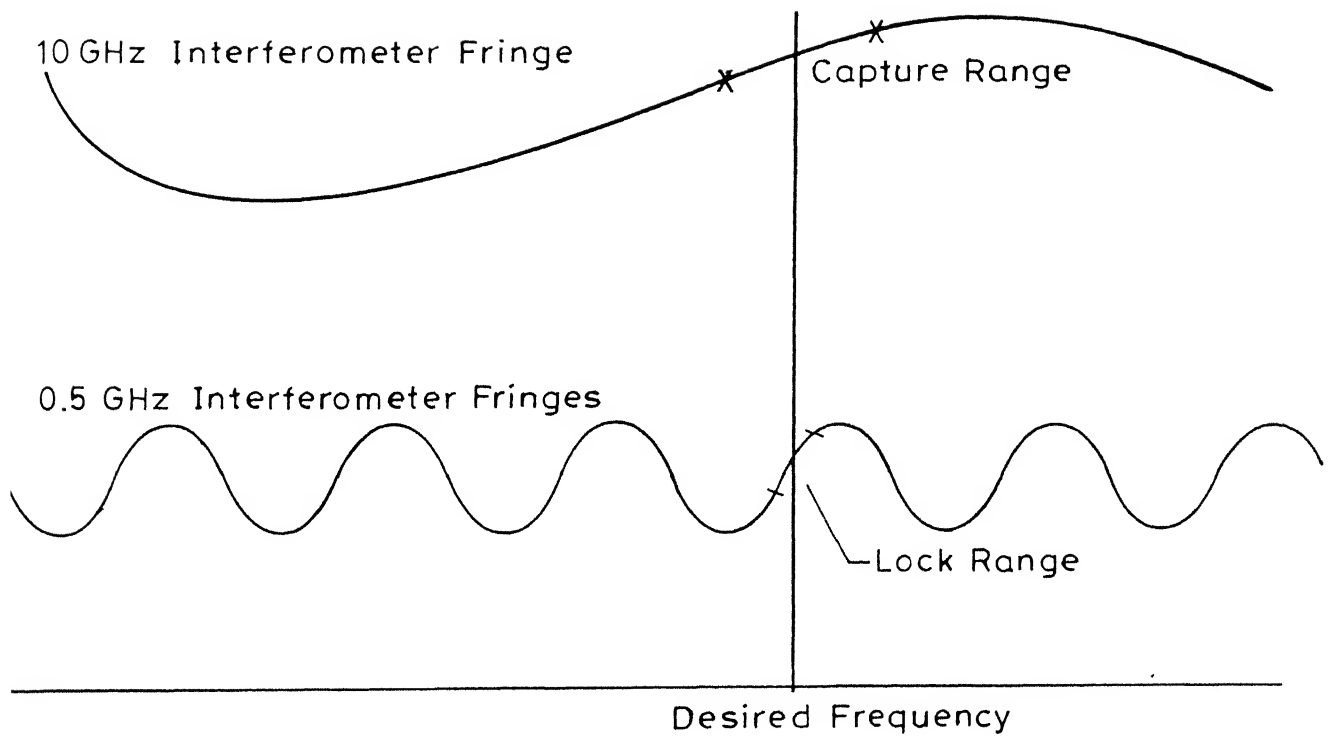


Fig.II.7 Single frequency selection in ring dye laser .

in a ring dye laser. Scans can be overlapped by observing the mode position with an external scanning interferometer and electronically readjusting the galvo and thick etalon positions.

Vibrations and microphonics in the cavity structure, bubbles and thickness variations in the dye jet varies the optical path length. This may cause mode hops of the laser. To prevent such mode hops the laser output is locked to two external interferometers by an electronic servoloop mechanism. One of these interferometers is a temperature stabilized etalon of 0.5 GHz FSR and the other an etalon of 10 GHz FSR. As shown in Fig II.8, the output frequency of the laser was locked to a fringe of the 0.5 GHz etalon. Whenever the frequency of the laser deviates from the lock point, an error signal was generated by the reference photodiode and the normalizing photodiode. This error signal is fed back to the PZT controlled mirror M_2 and the dual galvoplates to bring the frequency of operation of the laser back to the lock point. The 10 GHz etalon also monitors the frequency of the laser simultaneously. But this circuit is passive till a mode hop occurs. Then it takes control and returns the laser frequency to the correct fringe of the 0.5 GHz etalon. Then the control is returned to the electronics of 0.5 GHz etalon to make fine adjustments to the laser frequency. Scanning of the laser is achieved by varying the optical path of the 0.5 GHz etalon by rotating a galvomounted quartz plate within the interferometer cavity. The 10 GHz interferometer should also be scanned simultaneously. This is accomplished by varying the cavity length of this interferometer by PZT drives. Table II.3 gives the specifications of this laser.



g.II.8 Frequency locking of laser to external etalons .

Table II.3

Specifications of the Spectra Physics Model No. 380D Ring Dye Laser

Linewidth (RMS)	1 MHz ($3.3 \times 10^{-5} \text{ cm}^{-1}$) ($t < 5 \text{ s}$)
Scan range	30 GHz
Frequency drift	$< 50 \text{ MHz/hr}$
Scan time (30 GHz scan)	500 ms - 10 min
Amplitude stability	$< 2.5 \% \text{ @ peak of dye}$
Scan nonlinearity	$< 2 \%$
Polarization	Horizontal
Specified peak output power @pump power (60 % typical performance)	550 mW @ R6G/4W @ 514 nm 800 mW @ R6G/6W @ 514 nm
Mode hops	$< 1 / \text{hr}$
Output beam mode	TEM ₀₀

The high resolution setup shown in Fig II.5 is similar to the low resolution setup given in Fig II.3 except that in the high resolution experiment the laser frequency was monitored ; which was done by passing a small portion of the laser light through a 300 MHz FSR, high finesse (~ 200) Fabry - Perot Interferometer (Coherent model no. 216). The fringes of this etalon were recorded along with the signal on the chart recorder which served as frequency marker.

During the experiments the laser was coarsely tuned to a line with the help of the SPEX monochromator. Once the line is reached the electronic scan controls of the dye laser were used to record the complete profile of the line. Repeated scans were taken for each line.

II.4. OPTIMIZATION AND CALIBRATION

II.4.1. Introduction

In the field of Optogalvanic spectroscopy neon is a well studied species. This is the main reason why neon was chosen for testing and calibration. All the lamps used in the thesis contained neon as the buffer gas. In most cases the well known neon lines were used as the calibration lines for measuring the wavelengths. In the high resolution work conducted, neon OG lines helped in tuning the dye laser to the lines of interest.

II.4.2. Pulsed Optogalvanic spectroscopy of Neon

(a) Experimental Procedure:

A setup as described in Section II.3.1. was employed for conducting these experiments. The dye was either Rhodamine 6G in

ethanol or Rhodamine 6G solution with few drops of Rhodamine B solution in ethanol. Using these dyes, peak powers in excess of 30 kW in the range of 570.0 - 600.0 nm could be generated. The linewidth of the laser was measured to be less than 0.05 nm. The pulse repetition rate used was between 5 to 10 Hz. A Rb / Ne hollow cathode lamp (Instrumentations Laboratories Inc.) was used as the source of neon discharge. The lamp was operated between 6 to 20 mA of current. To minimize the electrical interference from the Nitrogen laser the power supply for sustaining the discharge and the boxcar averager were kept away from it and were operated on a separate power line. Use of shielded cables and isolated earthing of the detection and data processing instruments were necessary to minimize the noise pickup. Many runs were recorded with different laser powers and lamp currents

(b) Results and discussion:

Fig II.9 shows the observed optogalvanic spectrum of neon. All in all we observed 33 lines in the spectral range studied. From the results of Zalewski' [17] work we could identify 21 of these neon transitions. Zalewski in his work has reported 22 lines in this range and the missing line from our spectrum is at 590.278 nm. This is a very weak transition and is very near a strong transition at 590.246 nm. The wavelength separation is smaller than resolution of this setup and hence could not be observed. We have presented our results in Table II.4. The second column reports the wavelengths of the transitions in nm, as measured by our work. The third column presents the transitions of these lines. In the fourth and fifth columns we have presented

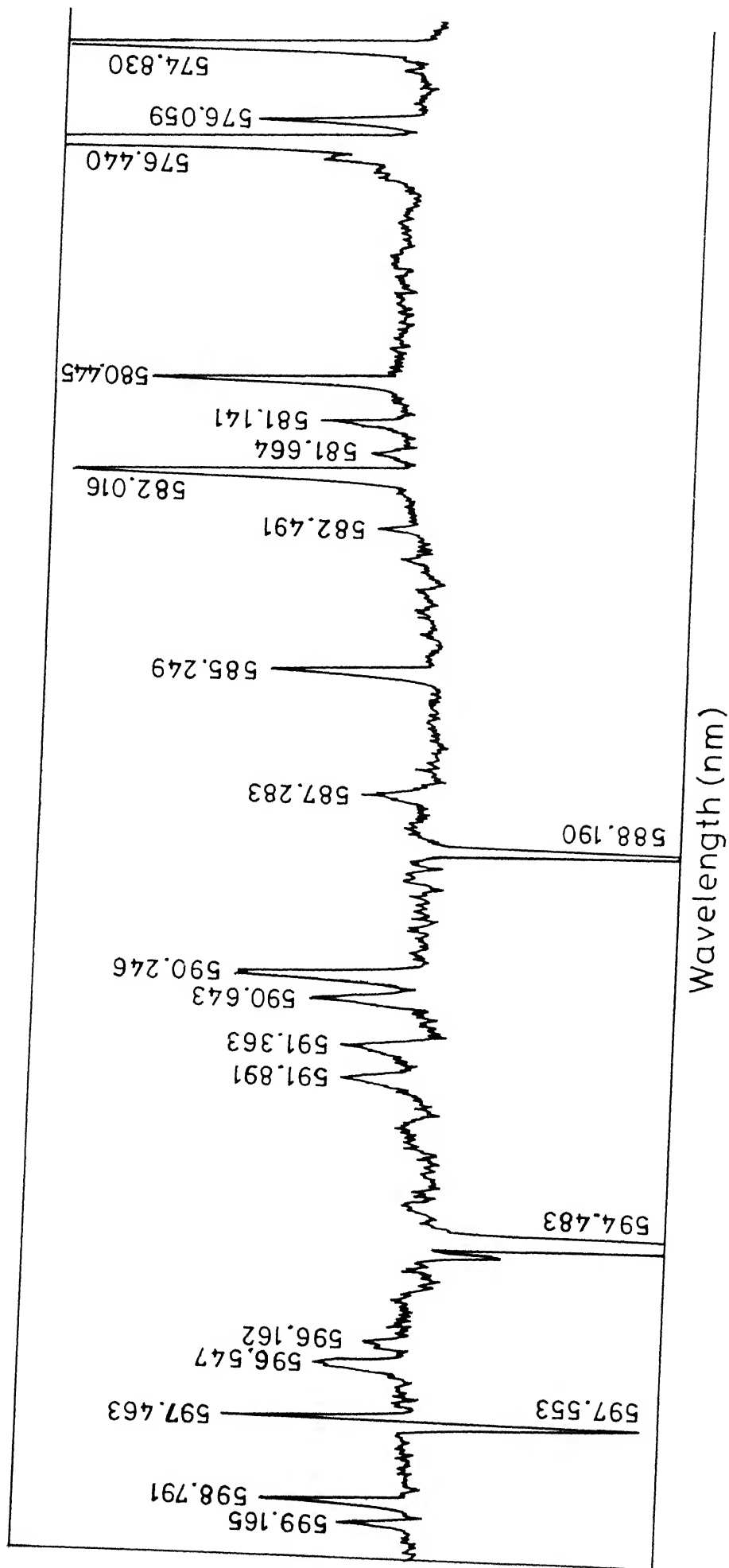


Fig.II.9 Optogalvanic spectrum of neon .

Table II.4

Results of Pulsed OGS of Neon

S. No.	Wavelength (nm) Present work	Transition	Wavelength (nm)		Com- ments
			Ref[17] *	Ref[18] *	
1	574.76	$3p[5/2]_3 - 4d[5/2]_3^0$	574.83	574.83	
2	576.02	$3p[5/2]_3 - 4d[3/2]_2^0$	576.06	576.06	
3	576.44	$3p[5/2]_3 - 4d[7/2]_4^0$	576.44	576.44	C
4	577.03	$3p'[1/2]^0 - 5d'[3/2]_1^0$	-	577.03	N
5	580.45	$3p[5/2]_2 - 4d[5/2]_2^0$	580.45	580.45	C
6	581.19	$3p[5/2]_2 - 4d[3/2]_1^0$	581.14	581.14	
7	581.67	$3p[5/2]_2 - 4d[3/2]_1^0$	-	581.65	N
8	582.02	$3p[5/2]_2 - 4d[7/2]_3^0$	582.02	582.02	
9	582.89	$3p[5/2]_2 - 4d[1/2]_1^0$	-	582.89	N
10	585.30	$3s'[1/2]_1^0 - 3p'[1/2]_0$	585.45	585.25	
11	586.84	$3p'[3/2]_1 - 4d'[3/2]_1^0$	586.84	586.84	
12	587.24	$3p'[3/2]_1 - 4d'[5/2]_2^0$	587.28	587.28	
13	588.19	$3s[3/2]_2^0 - 3p'[1/2]_1$	588.19	588.19	C
14	589.84	$3p'[3/2]_1 - 4d'[3/2]_1^0$	-	589.84	N
15	590.24	$3p'[3/2]_2 - 4d[5/2]_3^0$	590.25	590.25	
16	590.60	$3p'[3/2]_1 - 4d'[5/2]_2^0$	590.64	590.64	
17	591.39	$3p'[3/2]_1 - 4d[3/2]_1$	591.36	591.36	
18	591.89	$3p[1/2]_0 - 4d'[3/2]_1$	591.89	591.89	
19	592.36	$3p[1/2]_1 - 4d[3/2]_3^0$	-	592.27	N
20	593.44	$3p[3/2]_1 - 4d[3/2]_0^0$	-	593.45	N
21	593.88	$3p[5/2]_2 - 5s'[1/2]_1^0$	-	593.93	N

S. No.	Wavelength (nm) Present work	Transition	Wavelength (nm)		Com- ments
			Ref[17] *	Ref[18] *	
22	594.48	$3s[3/2]_2^0 - 3p'[3/2]_2$	594.48	594.48	C
23	596.08	$3p'[1/2]_1 - 4d'[3/2]_1^0$	596.16	596.16	
24	596.49	$3p'[1/2]_1 - 4d'[3/2]_2$	596.55	596.55	
25	597.36	$3p[3/2]_2 - 4d[5/2]_3$	597.46	597.46	
26	597.48	$3s[3/2]_2^0 - 3p'[3/2]_1^0$	597.55	597.55	
27	598.69	$3p[3/2]_2 - 4d[3/2]_2$	598.79	598.79	
28	599.06	$3p[3/2]_2 - 4d[7/2]_3$	599.17	599.17	

* Rounded off to second digit.

C Calibration line.

N Observed in optogalvanic spectroscopy for the first time.

the wavelengths of these lines as reported by Zalewski [17] and Striganov and Sventiski [18]. We could identify seven more lines of our spectrum from the emission tables of Striganov and Sventiski [18]. These lines were also reported in Table II.4. We observe that all our reported values compare very well with those reported by others within the limits of our experimental error. We could not identify the remaining five lines observed in our spectrum. The measured wavelengths of these lines are given in Table II.5.

II.4.3. CW Optogalvanic spectroscopy of Neon

(a) Experimental Procedure:

These experiments on neon were conducted with a setup similar to that described in Section II.3.3.. The dye laser was operated with Rhodamine 6G, which delivered a peak output power of 300 mW in the 568.0 - 633.5 nm range. The beam was chopped at 240 Hz for lock-in detection. A commercial Eu / Ne hollow cathode lamp (Instrumentations Laboratories Inc.) with 5 Torr of neon buffer gas in it was used as the source of neon discharge. In the first set of experiments conducted the peak laser power was held fixed at 200 mW and many scans were made for different lamp currents. This is to study the relationship between the OG signals of different lines and lamp current. The lamp current was varied in the range of 1 - 12 mA. The lamp was found to be unstable above this range of currents.

In the second set of experiments the lamp current was held fixed at 6.0 mA and scans were taken for different laser peak powers upto 150 mW. Laser power was varied by the introduction of

Table II.5

Unidentified lines in the OGS of Ne

S.No.	Wavelength (nm)
1	576.72
2	591.06
3	592.16
4	594.04
5	594.69

neutral density filters in the laser beam. These experiments were conducted to find the saturation characteristics of the transitions and for studying signal optimization.

(b) Results and discussion:

Fig II.10 shows an Optogalvanic spectrum of Eu / Ne hollow cathode lamp in the 568.0 - 633.5 nm range. In this we could identify 62 lines of neon. The measured wavelengths and transition assignments of these lines are given in the Table II.6. Wavelengths of these lines as measured by the other workers are also given in Table II.6. We see that our results agree very well with the results of Zalewski [18] within the limits of our experimental errors.

The optogalvanic signal as a function of the lamp current for some of the transitions of Neon is plotted in Fig II.11 (a), (b), (c), and (d). We see that the signal initially increases with lamp current, reaches a maximum and then falls. This behaviour is found to be followed by many of the lines studied. The optogalvanic signal observed as a function of the laser power for some transitions for Neon are plotted in Fig II.12 (a), (b), (c), (d) and (e). Some of the lines, particularly those originating from metastable states saturate at very low laser powers. The following formula was used to obtain the saturation behaviour of the observed signals

$$V_{OG} = \alpha I = \alpha_0 I / [1 + I/I_{sat}] \quad \text{-----(9)}$$

where,

V_{OG} = Magnitude of the OG signal;

α = $\alpha(I)$ = Absorption coefficient;

α_0 = Absorption coefficient for low level signals;

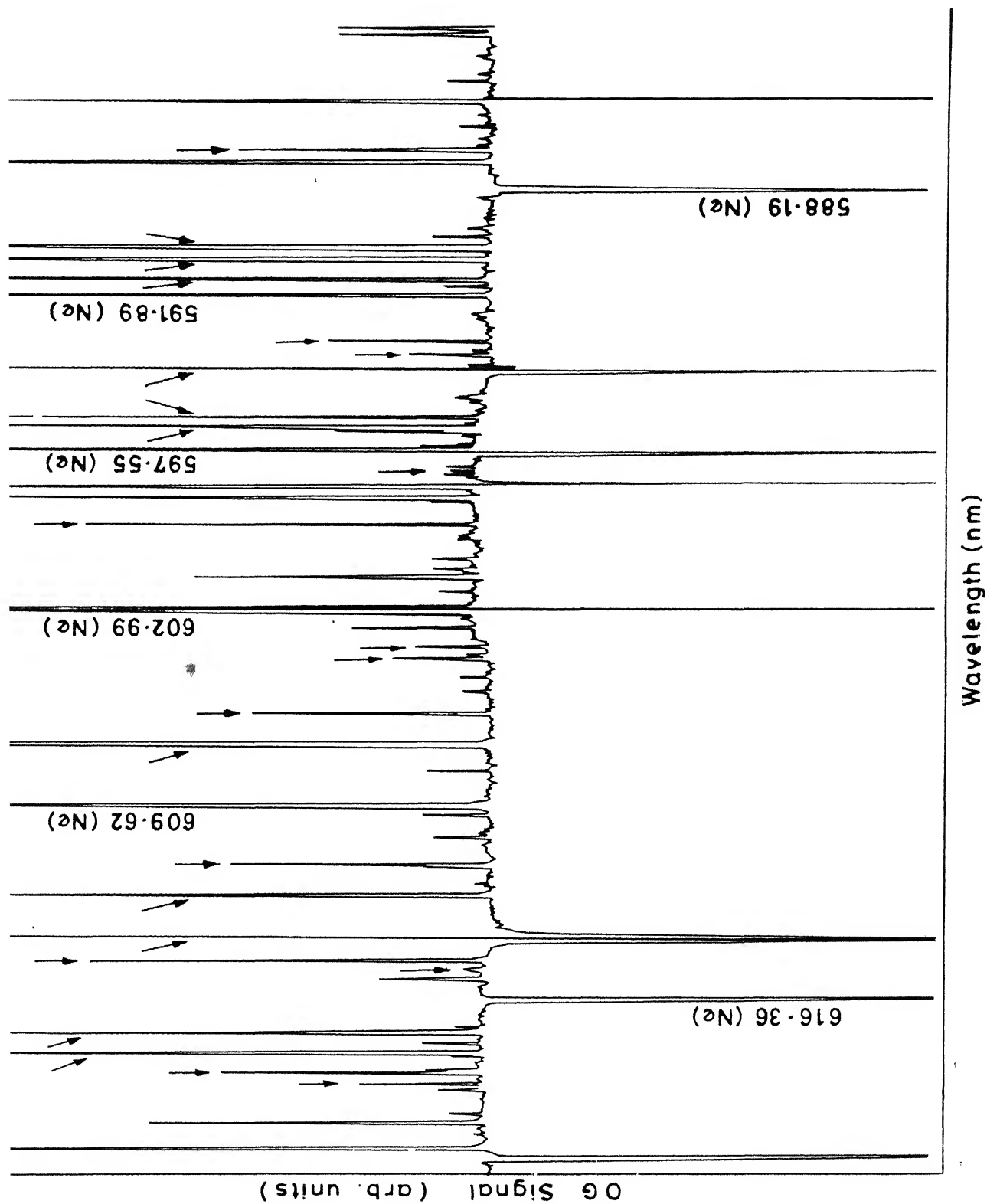


Fig. II.10 Part of the optogalvanic spectrum of hollow cathode Europium/neon spectral lamp. The peaks marked with arrows are neon transitions.

Table II.6

Results of CW OGS of Neon

S. No.	Wavelength (nm)	Transition	Wavelength (nm) Ref [18]	Comments
1	568.490	$3p'[1/2]_0 - 7s[3/2]_1^0$	568.465	
2	571.955	$3p[5/2]_2 - 4d'[5/2]_2^0$	571.953	
3	574.848	$3p[5/2]_3 - 4d[5/2]_2^0$	574.865	
4	576.076	$3p[5/2]_3 - 4d[3/2]_2^0$	576.059	
5	576.441	$3p[5/2]_3 - 4d[7/2]_4^0$	576.442	
6	577.007	$3p'[1/2]_0 - 5d'[3/2]_1^0$	577.031	
7	580.464	$3p[5/2]_2 - 4d[5/2]_2^0$	580.445	
8	581.141	$3p[5/2]_2 - 4d[3/2]_1^0$	581.141	
9	581.663	$3p[5/2]_2 - 4d[3/2]_2^0$	581.665	
10	582.016	$3p[5/2]_2 - 4d[7/2]_3^0$	582.016	
11	582.881	$3p[5/2]_2 - 4d[1/2]_1^0$	582.891	
12	585.249	$3s'[1/2]_1^0 - 3p'[1/2]_0$	585.249	C
13	586.863	$3p'[1/2]_1 - 4d'[3/2]_1^0$	586.842	
14	587.283	$3p'[1/2]_1 - 4d'[5/2]_2^0$	587.283	C
15	588.189	$3s[3/2]_2^0 - 3p'[1/2]_1$	588.189	C
16	589.821	$3p'[3/2]_2 - 4d'[3/2]_1$	589.841	
17	590.246	$3p'[3/2]_2 - 4d'[5/2]_3^0$	590.246	C
18	590.643	$3p[3/2]_1 - 4d[5/2]_2^0$	590.643	C
19	591.363	$3p[3/2]_1 - 4d[3/2]_1^0$	591.363	C
20	591.891	$3p[1/2]_0 - 4d'[3/2]_1^0$	591.891	C
21	593.465	$3p[3/2]_1 - 4d[3/2]_0^0$	593.446	
22	593.932	$3p[5/2]_2 - 5s'[3/2]_1^0$	593.932	

S. No.	Wavelength (nm)	Transition	Wavelength (nm) Ref [18]	Comments
23	593.967	-	-	X
24	594.483	$3p[3/2]_2^0 - 3p'[3/2]_2$	594.483	C
25	596.254	$3p'[1/2]_1 - 4d'[3/2]_1^0$	596.162	
26	596.623	$3p'[1/2]_1 - 4d'[5/2]_2^0$	596.317	
27	597.553	$3s[3/2]_2 - 3p'[3/2]_1^0$	597.553	C
28	598.217	$3p[3/2]_2 - 4d[3/2]_1^0$	598.240	
29	598.726	$3p[3/2]_2 - 4d[3/2]_2^0$	598.791	
30	599.165	$3p[3/2]_2 - 4d[7/2]_3^0$	599.165	
31	599.066	-	-	X
32	599.999	$3p[3/2]_2 - 4d[1/2]_1^0$	600.093	
33	602.999	$3s[3/2]_1^0 - 3p'[1/2]_1$	602.999	C
34	604.217	$3p'[1/2]_0 - 5d[3/2]_1^0$	604.201	
35	604.604	$3p[3/2]_1 - 5s'[1/2]_1^0$	604.614	
36	606.416	$3p[3/2]_1 - 5s'[1/2]_0^0$	606.454	
37	607.434	$3s[3/2]_1^0 - 3p[1/2]_0$	607.434	C
38	609.616	$3s[3/2]_1^0 - 3p'[3/2]_2$	609.616	C
39	611.770	$3p[3/2]_2 - 5s'[1/2]_1^0$	611.803	
40	612.767	$3s[3/2]_1^0 - 3p'[3/2]_1$	612.846	
41	614.306	$3s[1/2]_2^0 - 3p[3/2]_2$	614.306	C
42	615.017	$3p'[3/2]_1 - 4d[3/2]_1^0$	615.030	
43	615.594	$3p[3/2]_1 - 4d[3/2]_2^0$	615.615	
44	616.359	$3s'[1/2]_0^0 - 3p'[1/2]_1$	616.359	C
45	617.515	$3p'[3/2]_2 - 4d[5/2]_2^0$	617.529	
46	618.223	$3p'[3/2]_2 - 4d[3/2]_1^0$	618.317	

S. No.	Wavelength (nm)	Transition	Wavelength (nm) Ref [18]	Comments
47	618.938	$3p'[3/2]_2 - 4d[3/2]_2^0$	618.907	
48	619.287	$3p'[3/2]_2 - 4d[7/2]_3^0$	619.307	
49	620.291	$3p'[3/2]_2 - 4d[1/2]_1^0$	620.298	
50	620.542	$3p[3/2]_0 - 4d[3/2]_1^0$	620.578	
51	621.379	$3p[5/2]_2 - 5s[3/2]_1^0$	621.388	
52	621.728	$3s[3/2]_2^0 - 3p[3/2]_1$	621.728	C
53	622.680	$3p[1/2]_0 - 4d[1/2]_0$	622.574	
54	625.004	$3p'[1/2]_0 - 6s[3/2]_0$	624.959	
55	625.291	$3p'[1/2]_1 - 4d[3/2]_1^0$	625.273	
56	625.941	$3p'[1/2]_1 - 4d[3/2]_2^0$	625.879	
57	626.650	$3s'[1/2]_0^0 - 3p'[3/2]_1$	626.650	C
58	627.316	$3p'[1/2]_1 - 4d[1/2]_1^0$	627.302	
59	627.643	$3p'[1/2]_1 - 4d[1/2]_0^0$	627.604	
60	631.416	$3p'[3/2]_1 - 5s'[1/2]_0^0$	631.369	
61	633.130	$3p[3/2]_1 - 3s[3/2]_1^0$	633.090	
62	633.386	$3s[3/2]_2^0 - 3p[5/2]_2$	633.443	

C Calibration line.

X Unidentified line.

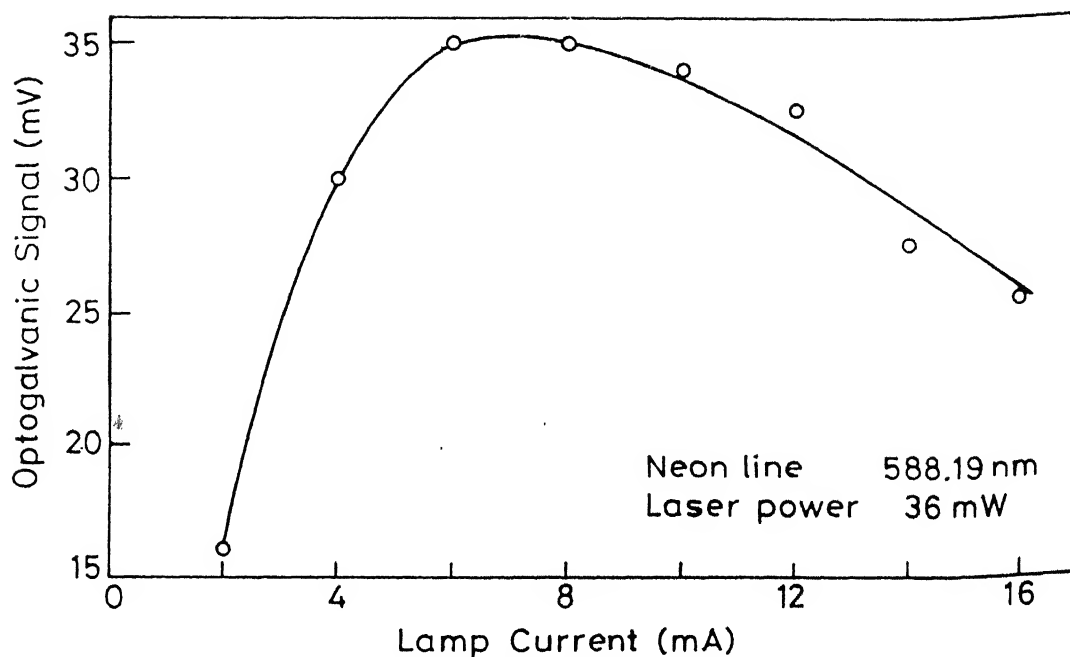


Fig.II.11(a) Variation of optogalvanic signal with lamp current.

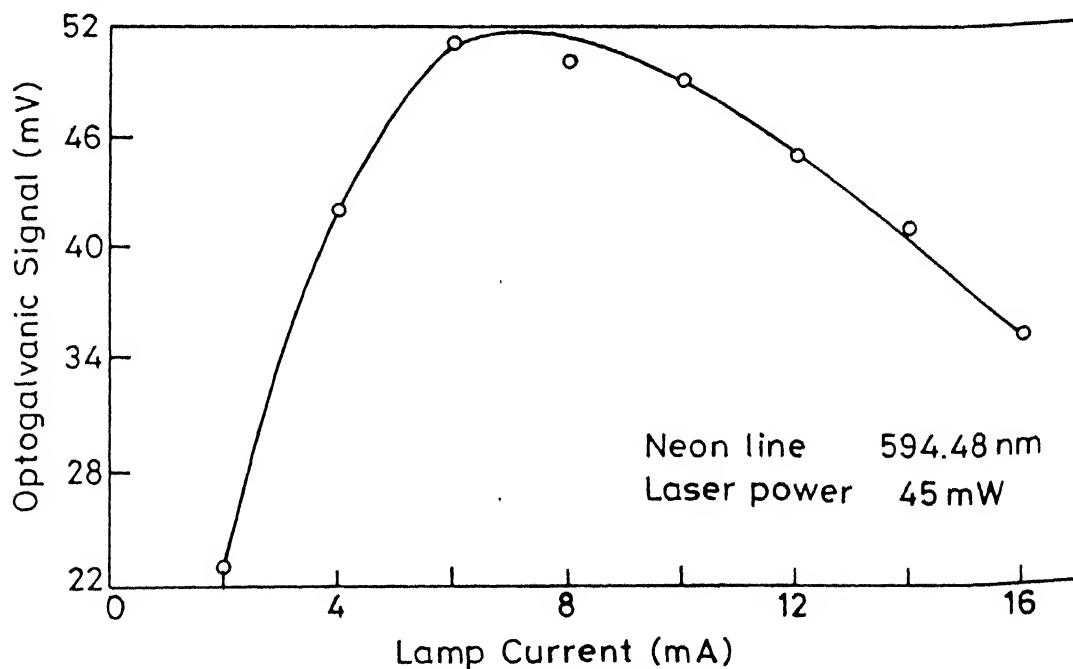


Fig.II.11(b) Variation of optogalvanic signal with lamp current.

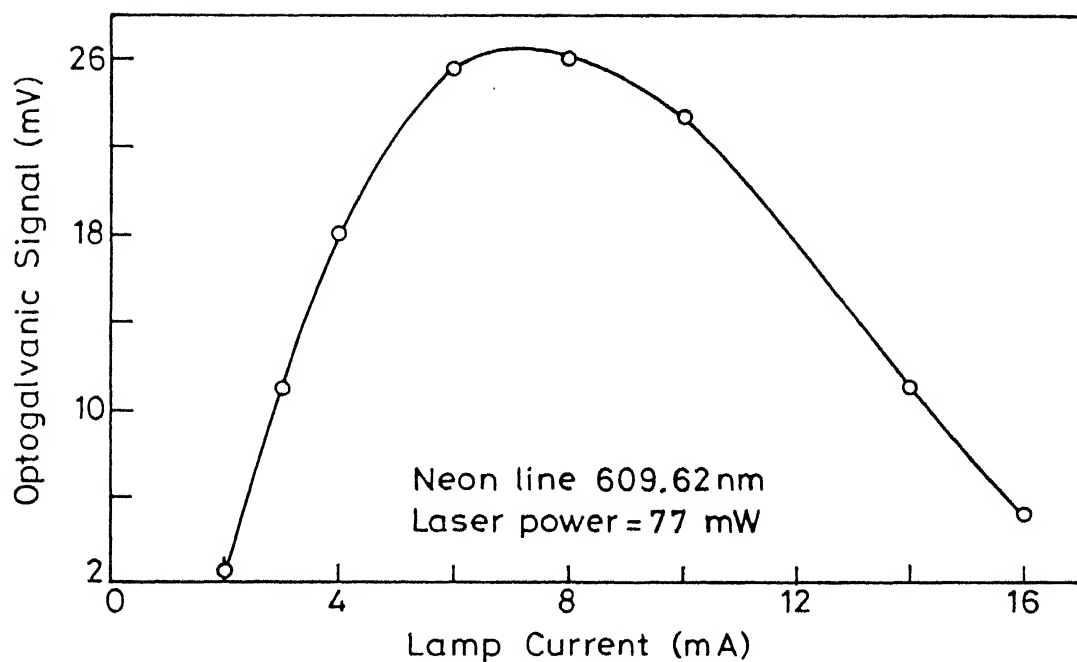


Fig.II.11(c) Variation of optogalvanic signal with lamp current.

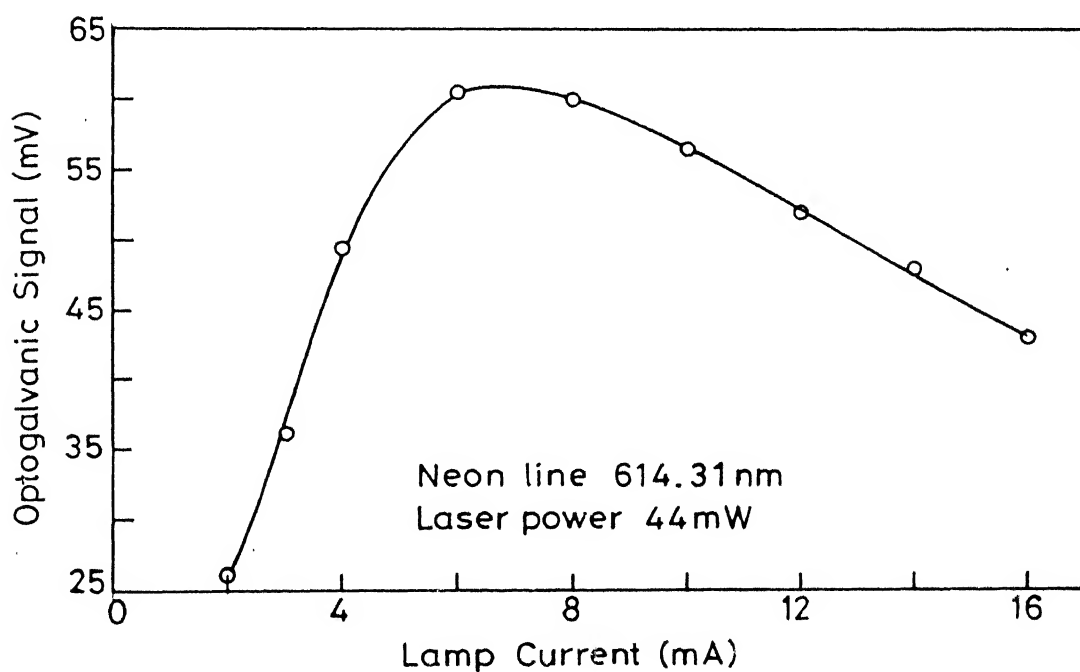


Fig.II.11(d) Variation of optogalvanic signal with lamp current.

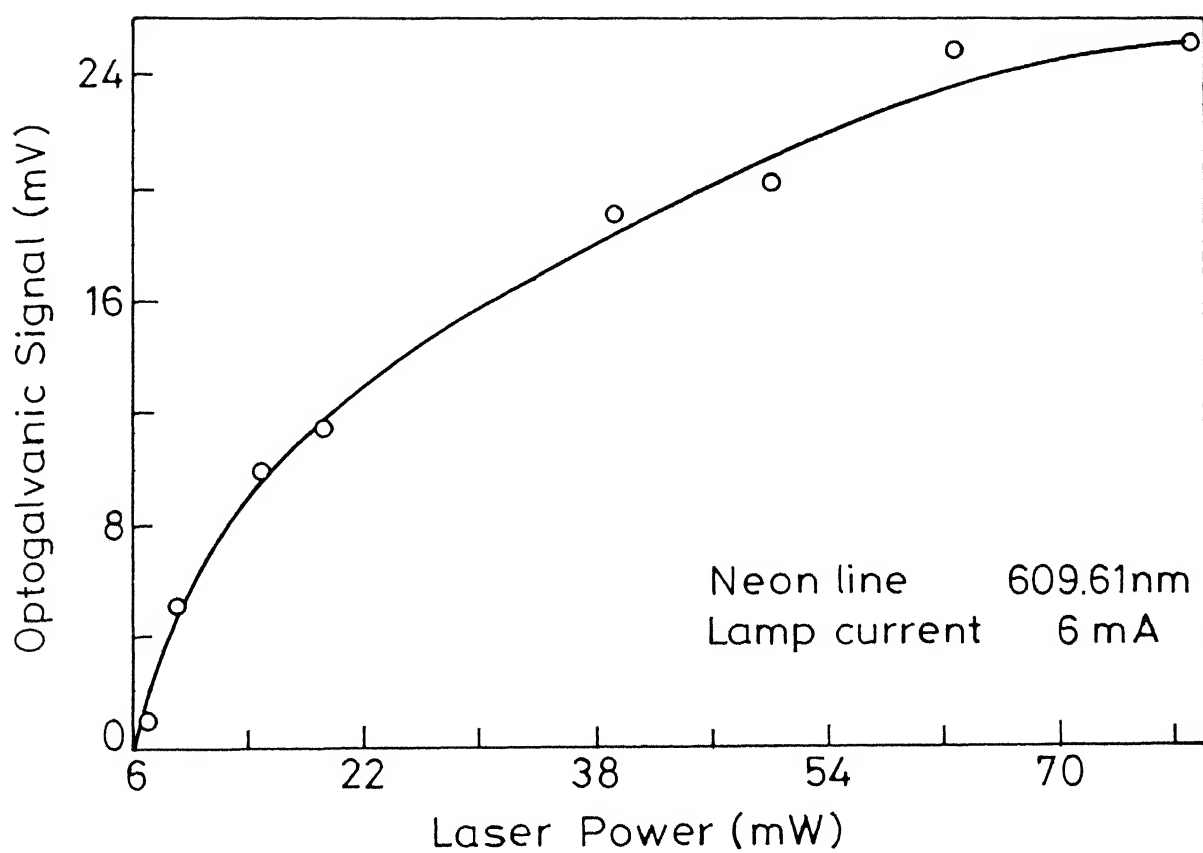


Fig.II.12(a) Variation of optogalvanic signal with laser power.

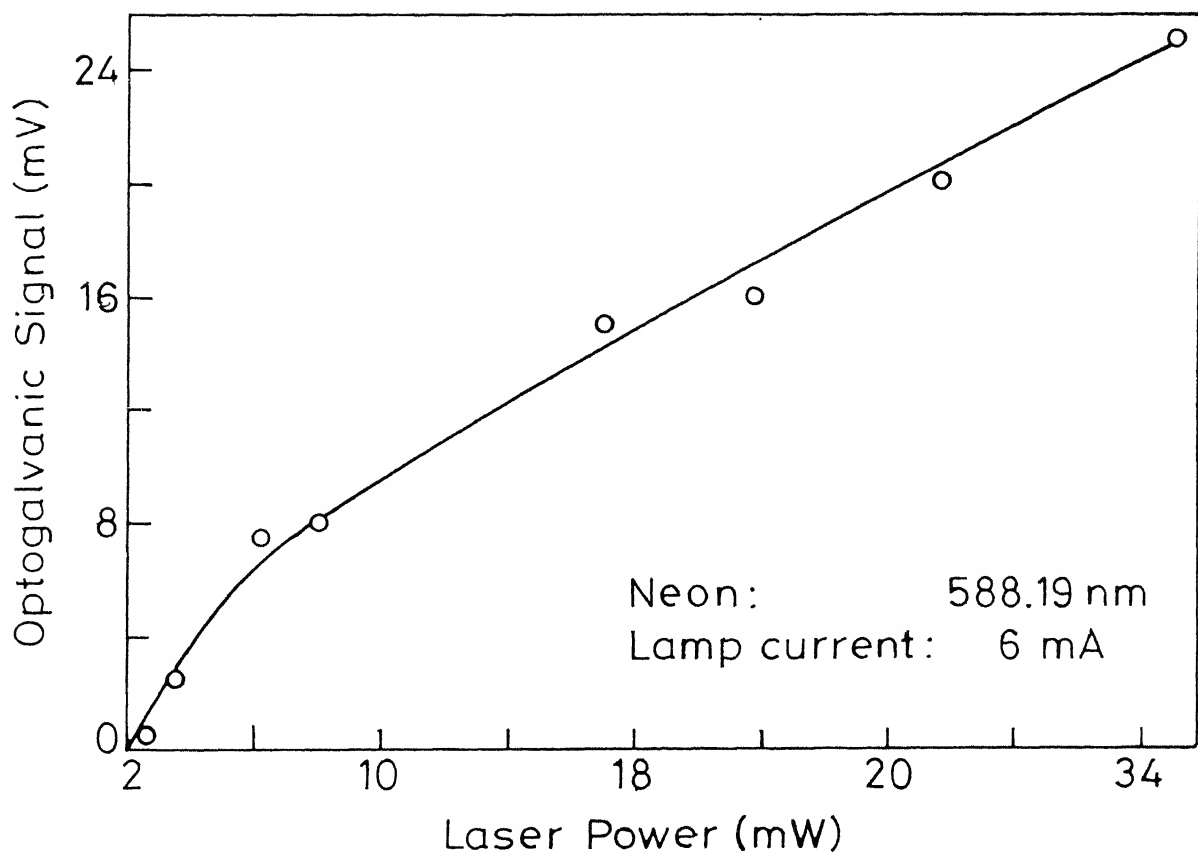


Fig.II.12(b) Variation of optogalvanic signal with laser power.

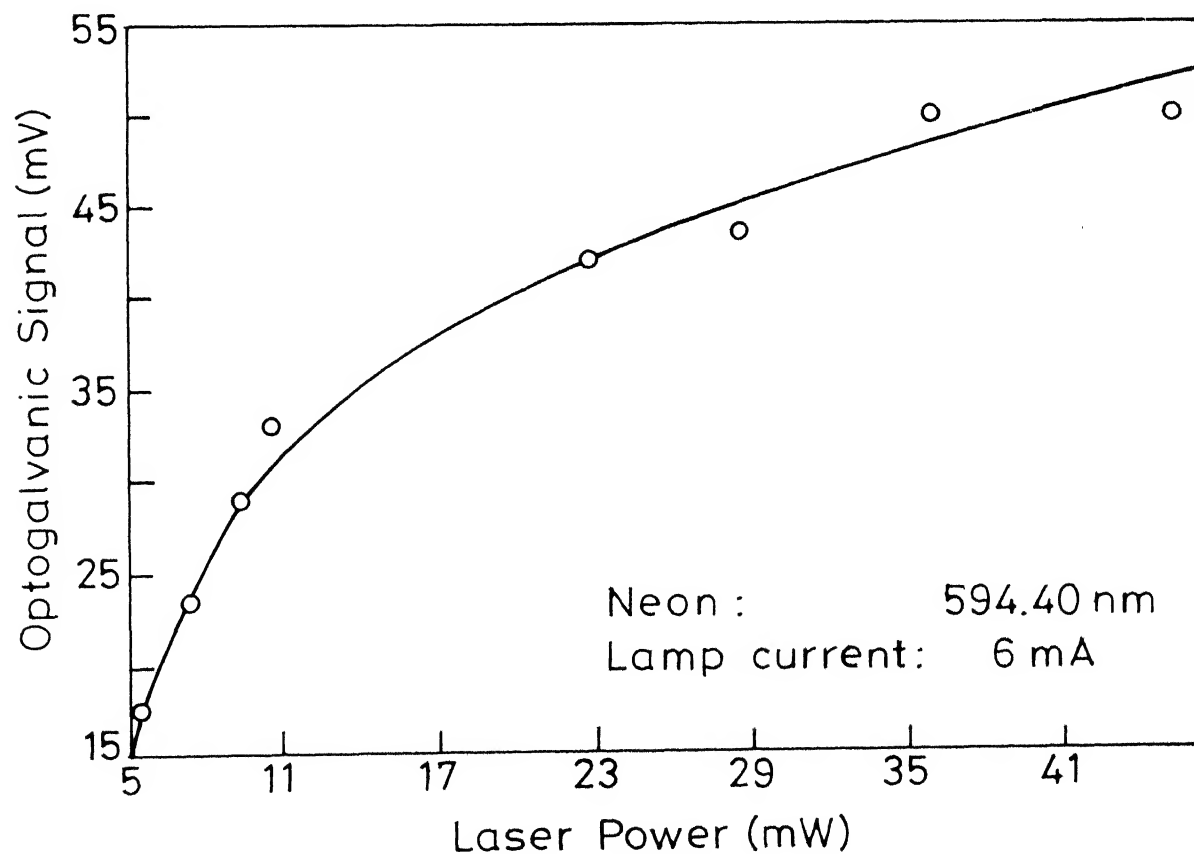


Fig.II.12(c) Variation of optogalvanic signal with laser power.

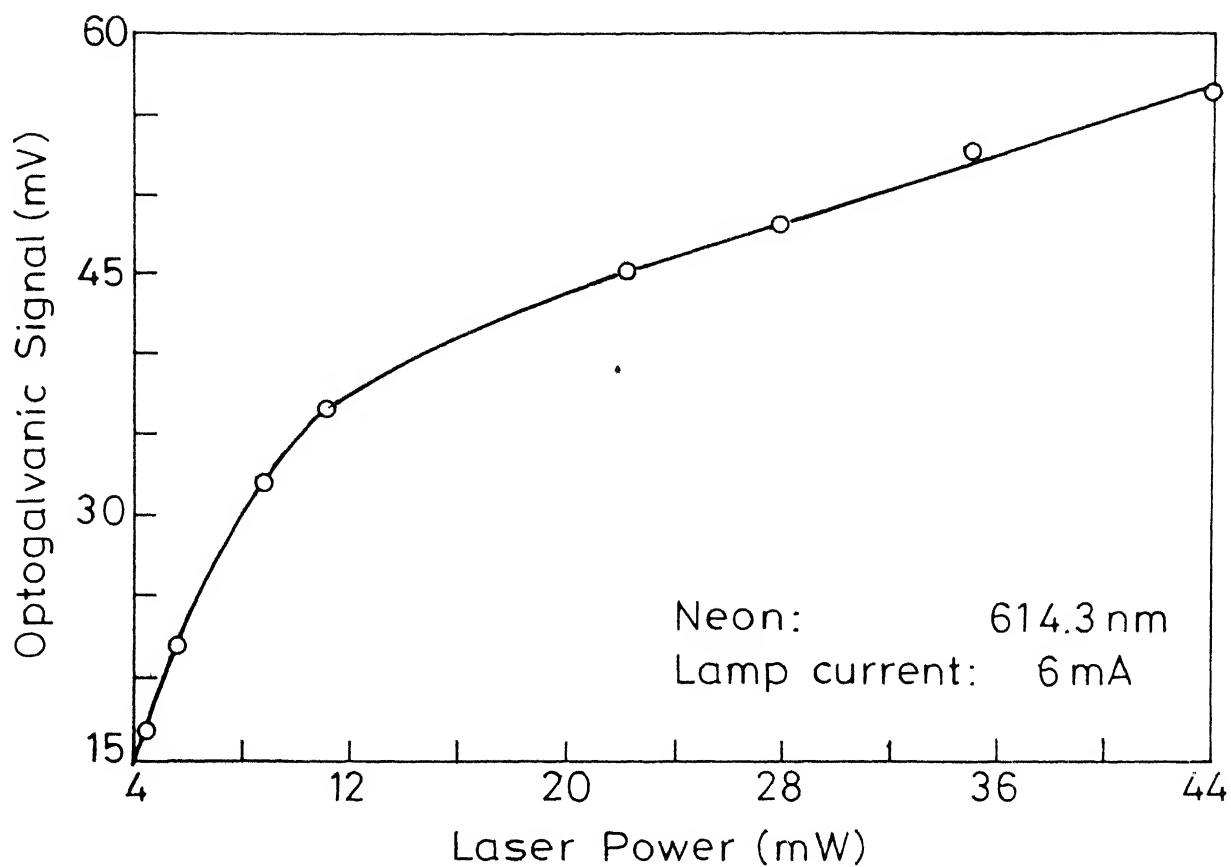


Fig. II.12(d) Variation of optogalvanic signal with laser power.

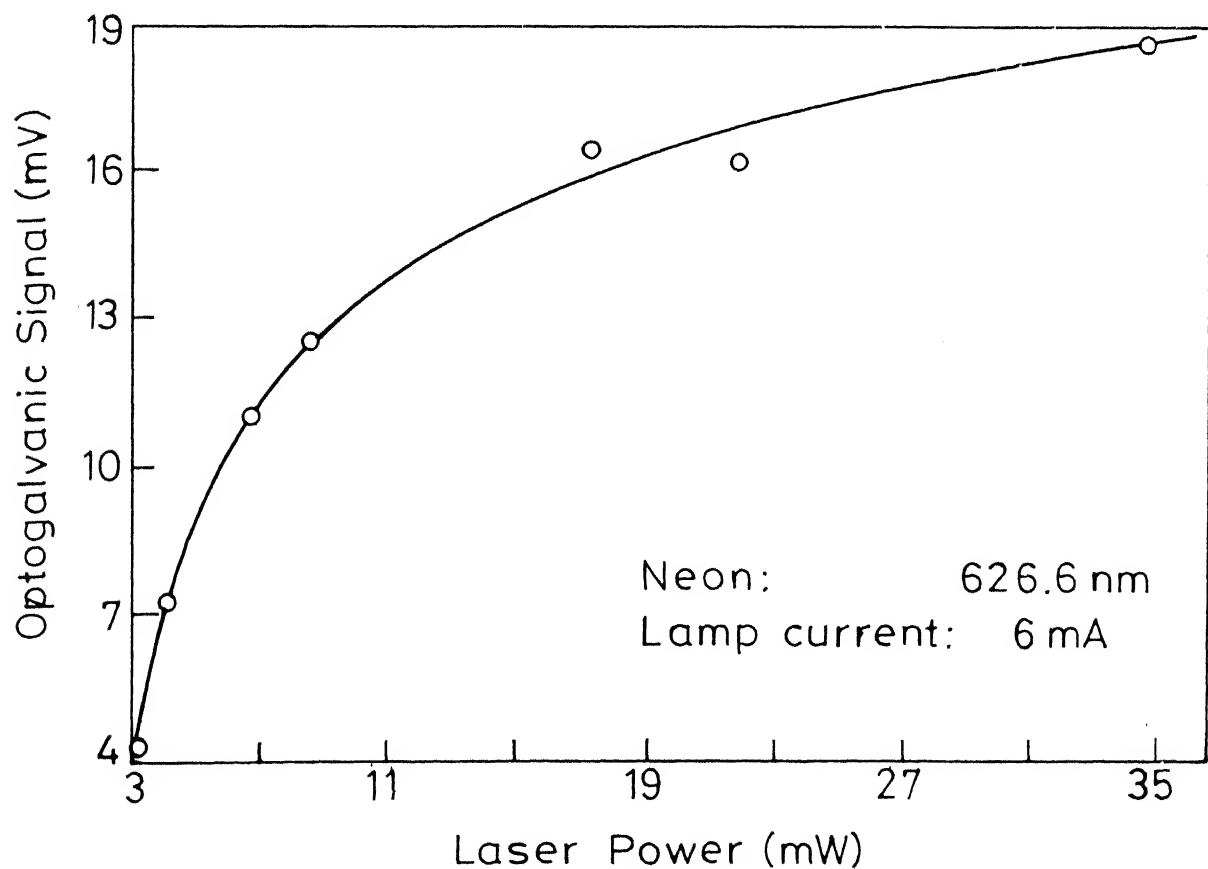


Fig. II.12(e) Variation of optogalvanic signal with laser power.

I_{sat} = Saturation power;

I = Laser power.

We have analyzed these curves with the help of a computer program which fits a least squares straight line for the data points $1/V_{\text{OG}}$ vs. $1/I$. From these fits we have extracted I_{sat} values for the transitions. These values are reported in Table II.7.

II.5. CONCLUSIONS

In conclusion it can be stated from these experiments that Optogalvanic spectroscopy is a simple and convenient technique. The spectra of neon is easily identifiable and reproducible over extended periods of time with a number of lines covering a broad range of the wavelengths making it quite suitable and convenient for calibration of the spectra and the wavelengths of the dye lasers.

We report here some lines of neon which are not hitherto reported in OGS. This is possible, probably because of the fact that we used high intensity lasers for these experiments and a setup with a good signal to noise ratio for detection. This work also demonstrated that even weak transitions can be conveniently studied using OGS.

Table II.7

Calculated saturation parameters for some transitions of Neon and Lanthanum

Element	Wavelength (nm)	Lamp current (mA)	Saturation parameter (mW)
Neon	588.1	6.0	19.0
	594.4	,,	34.3
	609.6	,,	47.1
	614.3	,,	14.9
	626.6	,,	25.6
Lanthanum	578.9	12.0	7.9
	593.0	,,	13.1
	608.4	,,	9.2
	579.1	8.0	6.5
	,,	10.0	37.3
	,,	12.0	16.1
	,,	14.0	10.5

REFERENCES

- [1] Goldsmith, J.E.M., and Lawler, J.F., *Comtemp. Phys.*, **22**, 235, (1981)
- [2] "International Colloquium on Optogalvanic Spectroscopy and its Applications" ed. Camus, P.J., *J. de Physique (Paris)*, **44**, Coll-c-7, (1983)
- [3] Foote, P.D., and Mohler, F.L., *Phys. Rev.*, **26**, 195, (1925)
- [4] Penning, F.M., *Physica*, **8**, 137, (1928)
- [5] Penning, F.M., *Phil. Mag.*, **11**, 961, (1931)
- [6] Kenty, C., *Phys Rev.*, **80**, 95, (1950)
- [7] Phelps, A.V., Molner, J.P., *Phys. Rev.*, **92**, 896, (1953)
- [8] Meissner, K.W., Miller, W.F., *Phys. Rev.*, **92**, 896, (1953)
- [9] Joshi, M.M., *Nature*, **154**, 147, (1944)
- [10] Venkateswarlu, V., Ramaiah, N.A., *J. Opt. Soc. Japan.*, **9**, 225, (1955)
- [11] Badareu, E., Popescu, I., Ghita, C., *Brit. J. Appl. Phys.*, **15**, 1171, (1964)
- [12] Green, R.B., Keller, R.A., Luther, G.G., Schenck, R.K., and Travis, J.J., *Appl. Phys. Lett.*, **29**, 727, (1976)
- [13] Smyth, K.C., and Shenck, P.K., *Chem. Phys. Letter.*, **55**, 466, (1977)
- [14] Pepper, D.M., *IEEE J. Quantum Electronics*, **QE-14**, 971, (1978)
- [15] Erez, G., Lavi, S., Miron, E., *IEEE J. Quantum Electronics*, **QE-15**, 1328, (1979)
- [16] Hansch, T.W., *Appl. Opt.*, **11**, 895, (1972)
- [17] Zalewski, E.F., Keller, R.A., and Engelman, R., Jr., *J. Chem. Phys.*, **70**, 1015, (1979)
- [18] Striganov, A.R., and Sventiski, "Tables of Spectral Lines of Neutral and Ionized Atoms", (IFI, Plenum, New York, 1968), 335 - 336

C H A P T E R I I I

CONTINUOUS WAVE OPTOGALVANIC SPECTROSCOPY
OF LANTHANUM AND EUROPIUM

III.1. INTRODUCTION TO THE SPECTROSCOPY OF RARE-EARTHS

Rare-earths are elements of the sixth period of the periodic table, starting with lanthanum ($Z=53$) and ending with lutecium ($Z=71$). Lanthanum has a xenon electronic core and some electrons in 4f, 5d and 6s shells. Rare-earth elements do not differ very much in their chemical properties. This is due to the fact that on an average the 4f electrons are held considerably closer than the 5p and 6s electrons and the chemical properties are basically determined by these peripheral electrons. However the optical properties of the rare-earth elements are drastically diverse. Spectra of rare-earth elements are rich in number of lines and very complex in structure. This is because electron configurations containing f electrons give rise to extremely large number of terms and levels. Moreover a configuration containing for example f^k electrons and s, p, and d electrons the number of terms can be upto several thousands and the number of levels may exceed 10,000. The complex spectra of rare-earths is due to the vast number of allowed transitions between these levels. It should also be noted that the ionization potentials of these elements are very low. Hence ion spectra is always present along with the neutral atom spectra even in mild arcs. This further complicates the spectra and prevents easy assignment of

energy levels and classification of transitions.

Experimental and theoretical investigations have been going on in the field of rare-earth spectroscopy for the past six decades. Even though a tremendous amount of information has been gathered about the energy levels, ionization limits, lifetimes transition probabilities etc., owing to the complexities mentioned before, the analysis is by no means complete for all the rare-earth atoms and their ionic species. Information on rare-earth elements is extremely useful in several areas of research like astrophysics, isotope separation, laser materials development, etc.. Hence more complete data on energy levels and wavelength of transitions are needed.

III.2. EXPERIMENTAL TECHNIQUES OF RARE-EARTH SPECTROSCOPY

In the past, information regarding rare-earth elements were mainly obtained from arc and spark spectroscopy. Analysis of emission spectra of electrodeless discharge lamps and hollow-cathode lamps were also useful in gathering information about these elements. The wavelengths of the lines were mostly measured by prism and grating spectrographs. Better resolutions were obtained by the use of Fourier transform spectroscopy. Low lying levels of these atoms were investigated by RF and Microwave spectroscopy. Further information was obtained by Absorption spectroscopy. Here the rare-earth element vapor is produced in a cell maintained at high temperatures in an oven and often a broad band high intensity light source is used for the experiments on absorption spectroscopy. The assignment of transitions and classification of energy levels were done by Zeeman spectroscopy

of these elements. Moreover if nuclear properties like nuclear spin etc. were known the hyperfine structure of the transition lines helped in these classifications and assignments. These works call for high resolution setups like Photoelectrically recording Fabry-Perot Interferometers.

Lasers and laser spectroscopic techniques have also made an impact in the field of rare-earth spectroscopy. Childs and Goodman [1-3] have employed Laser induced fluorescence in atomic beams to investigate many rare-earth elements. Owing to their high peak power pulsed lasers have been used by Paisner et al. [4] to study the Rydberg levels and auto-ionizing levels of many of these elements. The main problem in rare-earth atom spectroscopy is the high refractory nature of these elements (Table III.1). One can conveniently sputter these elements in a discharge and produce adequate number of atoms and ions for spectroscopy work. As mentioned in Chapter II, Optogalvanic detection scheme is a very elegant and a simple technique while working with discharges. Optogalvanic spectroscopy of rare-earth elements have been conducted in the past by investigators like Keller et al. [5] on Eu and Behrens et al. [6] on La, Eu and Yb.

In our group, a program was initiated to investigate the energy level spectra, Hyperfine structures and Isotope shifts of rare-earth elements by Optogalvanic spectroscopy. This chapter reports the results of CW Optogalvanic Spectroscopy of lanthanum and europium. The data clearly demonstrates the suitability of this technique for rare-earth spectroscopy.

106276

Table III.1

Melting and Boiling temperatures
of rare-earth elements

Element	Melting Point °C	Boiling Point °C
La	920	3469
Ce	795	3468
Pr	935	3127
Nd	1024	3027
Pm	1035	2730
Sm	1072	1900
Eu	826	1439
Gd	1312	3000
Tb	1356	2800
Dy	1407	2600
Ho	1461	2600
Er	1497	2900
Tm	1545	1727
Yb	824	1427
Lu	1652	3327

III.3. SPECTROSCOPY OF LANTHANUM

III.3.1. Energy Levels of La-I and La-II

The arc and spark spectra containing 700 lines of La-I was reported by Meggers [7] in the 264.7-1095.2 nm range in 1932. Fischer et al. [8] have reported 10 lines in the IR region (1.11-1.41 μm). Giacchetti et al. [9] have reported spectrum of RF-excited electrodeless Lanthanum lamp in the 250 - 900 nm range. Ben Ahmed [10] has conducted Fourier transform spectroscopy in the 690.0 nm - 2.3 μm range and has reported transition wavelengths to a higher accuracy. High accuracy Zeeman data of 151 lines of La I have been reported by Harrison et al. [11]. Further Zeeman work on La-I was conducted at the Argonne National Laboratory; and the analyzed results of these experiments were reported by Ben Ahmed [10]. The g-factors of 13 low lying even levels were reported by Childs and Goodman [12] from their atomic beam magnetic resonance experiments.

Russel and Meggers [13] have classified 540 of the La I lines in 1932. This work is yet to be superseded in that range. Fischer et al. [8] have also classified 10 IR lines. More lines have been classified and levels found to a better accuracy by Giacchetti et al. [9] and Wilson [14]. By now many even and odd configurations have been identified and tabulated by Martin et al. [15] for the National Bureau of Standards (U.S.A.). From this table it can be seen that the identified even configurations are $5d6s^2$, $5d^26s$, $5d^3$, $4f6s6p$, $5d^27s$, $5d6s7s$ and $5d^26d$. The identified odd configurations are $5d6s6p$, $5d^26p$, $6s^26p$, $4f5d6s$, $4f6s^2$ and $6s^28p-23p$. Observed transitions are between the energy levels formed by these configurations.

Meggers' [7] in his work has reported 800 lines of La-II. 700 of them were assigned by the work of Russel and Meggers [13]. Harrison et al. [11] have reported g-factors of 504 La-II lines. The energy levels of La-II were also tabulated in the NBS tables [15]

III.3.2. Experimental procedure

Optogalvanic Experiments were conducted to get the spectra of La-I and La-II with an arrangement as described in Chapter II. The Dye Laser was scanned in the 578.5 - 621 nm range. The linewidth of laser was 0.05 nm. Lanthanum was sputtered in a hollow cathode lamp (HCL) (Laboratory Instruments Inc.), which also contained 5 Torr of neon as the buffer gas. The value of the ballast resistor used was 25 k Ω . The signal was picked off by a 0.01 μ F capacitor. The laser beam was chopped at 241 Hz for Lock-in detection. This frequency was found to give optimum signal to noise ratio. Many runs were made with lamp current in the range of 4.0 - 16.0 mA and laser power in the 10 - 300 mW range. The resulting spectra of La-I and La-II along with Ne-I were recorded.

III.3.3. Results and Discussion

We report for the first time a broad band optogalvanic spectrum of lanthanum. Fig III.1 shows a sample Optogalvanic spectrum of La/Ne HCL. The Neon lines were first identified and were used for calibration. La-I and La-II lines were identified with the help of the NBS Table of wavelengths [16]. In

Table III.2 results of the La-I spectra are presented. The first column shows the wavelengths of transitions as measured by this work. The second column gives transition assignments for them as reported by Russel and Meggers [13]. In the third column we present the wavelengths of these transitions as reported in the NBS tables [16]. The fourth and fifth columns present the lower and upper level energies (in cm^{-1}) of the transitions. In the sixth column the relative Optogalvanic signal strengths of these lines as measured by us are presented. The final column presents the relative intensities of these lines from arc spectra data [16]. Table III.3 presents similar results for La-II.

From Fig. III.1 one notices that the signal to noise ratio of the spectra is good. We could identify 40 distinct transitions of La I in the 578.5-621 nm range. From Table III.2 we notice that OG intensities do not follow the emission intensities. This is expected since the OG signal strengths depend in a complicated way on the characteristics of the discharge plasma. However it should be noted that many signals of La-I are very strong. Commercial hollow cathode lamps operate with small currents (<20 mA). Hence the number of atoms sputtered will be very low. However most of the transitions are observed even at these currents. This shows the high sensitivity of the Optogalvanic detection. With these lamps we could observe transitions not only from ground state but also from highly excited states. Even at low currents of about 10 mA used, we could get reasonable number of atoms in excited states as high energy as 16856.83 cm^{-1} and use the laser to further excite these atoms to higher energy states. In this way, the highest level reached in this work was

Table III.2

Transitions of La I by Optogalvanic Spectroscopy

Measured Wave- length Å	Transition	Wave- length Ref [16] Å	Energy(cm ⁻¹)		Rel. Signal Strength	
			Lower Level	Upper Level	OGS	Emis- sion
6207.19	--	6206.76	-	-	110	2
6165.93	$a^4P_{3/2} - x^4D_{3/2}^o$	6165.70	7490.46	23704.76	43	30
6145.78	$z^4F_{7/2} - e^4D_{7/2}$	6145.30	15019.55	31287.65	23	3
6136.66	$a^4F_{5/2} - y^4D_{7/2}^o$	6136.48	7011.90	23303.31	17	2
6134.18	$a^4P_{1/2} - x^4D_{1/2}^o$	6134.39	7231.36	23528.38	22	20
6123.73	--	6123.75	-	-	23	2
6121.60	--	6121.27	-	-	9	
6120.68	$z^4F_{3/2} - 34$	6120.38	13260.36	29594.81	14	
6112.28	$a^2F_{7/2} - w^2F_{7/2}$	6111.72	8052.15	24409.70	27	20
6109.17	$a^4P_{5/2} - x^4D_{5/2}^o$	6108.48	7679.94	24046.06	60	40
6106.82	$a^4F_{5/2} - y^2D_{5/2}^o$	6107.27	3010.01	19379.44	6	4
5091.84	$\{ a^2P_{1/2} - x^2P_{1/2}^o$	6092.22	9044.21	25453.92	4	2
	$\{ z^4D_{3/2}^o - e^2F_{3/2}$		14708.96	31119.08		
5088.43	--	6088.00	-	-	9	2
5085.09	$y^2F_{5/2}^o - 35$	6084.89	16856.82	33286.50	106	5
5071.60	$b^2D_{3/2} - x^4F_{3/2}^o$	6072.05	8446.03	24910.39	3	3
5068.72	$a^4P_{1/2} - x^4F_{3/2}^o$	6068.68	7231.36	23704.76	32	20
5044.67	$b^2D_{3/2} - x^4F_{5/2}^o$	6044.80	8446.03	24984.33	13	20
5042.26	--	6041.60	-	-	39	2
5039.16	$a^4P_{3/2} - x^4D_{5/2}^o$	6038.59	7490.46	24046.06	43	20
5032.98	$a^2P_{1/2} - y^4P_{1/2}^o$	6032.38	9044.21	25616.90	20	5

cont'd..

Measured Wave- length \AA	Transition	Wave- length Ref [16] \AA	Energy(cm^{-1})		Rel. Signal Strength	
			Lower Level	Upper Level	OGS	Emis- sion
6025.54	--	6025.09	-	-	15	2
6017.57	$z^4F_{3/2}^o - e^4F_{3/2}$	6017.16	13260.36	29874.89	35	3
6016.77		6017.16			20	3
6007.60	$a^4F_{5/2} - y^4P_{1/2}^o$	6007.34	2668.20	25616.90	52	50
5982.40	$a^2F_{3/2} - y^2D_{5/2}^o$	5982.34	7490.46	19379.44	35	10
5962.36	{ b ² D _{5/2} - x ² P _{3/2}	5962.30	-	-	Sat.	4
		5962.59	9183.77	23950.39	Sat.	4
5935.67	$a^2F_{7/2} - y^4F_{5/2}^o$	5935.29	8052.15	20338.30	42	20
5930.51	{ a ² D _{3/2} - y ² F _{5/2} ^o	5930.68	0.00	16856.82	Sat.	100
	{ a ² D _{5/2} - y ² F _{5/2} ^o	5930.62	1053.20	17910.28	Sat.	200
5928.44	$a^2F_{5/2} - w^2F_{5/2}^o$	5928.49	7011.90	23875.00	19	5
5917.34	$a^2D_{5/2} - z^4G_{5/2}^o$	5917.63	1053.20	17947.16	140	20
5901.13	$a^4P_{1/2} - 4^o_{3/2}$	5900.75	7231.36	24173.86	18	3
5895.18	$a^4P_{5/2} - z^4S_{3/2}^o$	5894.85	7679.94	24639.27	16	20
5875.11	$a^4P_{3/2} - v^2F_{5/2}^o$	5874.73	7490.46	24507.89	10	8
5870.39	$a^2F_{7/2} - x^4D_{7/2}^o$	5869.95	8052.15	25083.44	45	2
5848.39	$z^4F_{3/2}^o - e^4F_{5/2}$	5848.37	13260.36	30354.32	12	15
5845.20	$a^2D_{5/2} - z^4P_{5/2}^o$	5845.02	1053.20	18157.00	10	10
5830.20	$a^4P_{3/2} - z^4S_{3/2}^o$	5829.72	7490.46	24639.27	45	21
5822.21	$a^2G_{7/2} - y^2G_{7/2}^o$	5821.99	9960.96	27132.50	45	30
5791.12	$a^4F_{9/2} - y^4F_{9/2}^o$	5791.34	4121.61	21384.06	128	200
5789.14	$a^4F_{7/2} - y^4F_{7/2}^o$	5789.22	3494.58	20763.31	92	150

Table III.3

Transitions of La II by Optogalvanic Spectroscopy

Measured Wave- length (Å)	Transition	Wave- length Ref. [16] (Å)	Energy(cm ⁻¹)	
			Lower Level	Upper Level
6203.96	$z^3D_3^0 - e^3D_2$	6203.51	22537.3	38221.49
6173.54	$a^3F_3 - y^3F_2^0$	6172.73	1016.10	17211.93
6147.59	$a^3F_4 - y^3F_3^0$	6146.53	1970.70	18235.56
6126.01	$b^1D_2 - x^3F_3^0$	6126.09	10094.86	26837.66
5948.34	$z^3G_3^0 - a^1F_3$	5948.30	20402.82	
5808.94	$a^3F_2 - y^3F_2^0$	5808.32	0.00	17211.93
5805.11	$a^3F_3 - y^3F_3^0$	5805.78	1016.10	18235.56

33281.5 cm^{-1} above the ground level.

Our main aim was to study the hyperfine structure of as many strong lines of La as possible. For doing so we needed the optogalvanic spectra of these transitions. Study of broad band Optogalvanic spectrum greatly helped to choose the transitions on which high resolution work can be carried out. Details of the high resolution experiments conducted are presented in Chapter-IV of this thesis.

III.4. SPECTROSCOPY OF EUROPIUM

III.4.1. Energy levels of Eu I

Europium is a rare-earth element with a half filled $4f$ shell. King [17] in 1939 had observed the spectra of Europium in $210.0 - 1016.5 \text{ nm}$ range. He reported 2200 lines of Eu-I in that range. In 1975 Smith and Tomkins [18-19] have conducted absorption spectroscopy experiments in $210.0 - 1016.5 \text{ nm}$ range in Europium. All the lines reported by them were transitions from ground state of Eu-I to upper even parity states. As early as 1939 Russel and King [20] have classified 1100 lines. This accounted for almost all the strong lines of Eu-I. Further classification was done by Smith and Tomkins [18-19] from their Zeeman spectroscopy work. From the theoretical interpretations of the results of the above mentioned experiments it was found that Eu-I has many odd configurations like $4f^7 6s^2$, $4f^7 5d 6s$, $4f^7 6s 7s$, $4f^7 5d^2$, $4f^7 6s 6d$, $4f^7 6s 8s$, $4f^7 6s 7d$ and $4f^7 6p^2$. The even configurations identified were $4f^7 6s 6p$, $4f^7 5d 6p$, $4f^6 5d 6s^2$, $4f^6 5d^2 6s$, $4f^7 6s 7p$ - $18p$, and $4f^7 6s 42p$ - $67p$. The ground state of Eu-I is $4f^7 6s^2 \text{ } ^8S_{7/2}^0$. All the terms and levels from the above

configurations are tabulated in the NBS tables [15].

III.4.2. Experimental procedure

Optogalvanic spectroscopy of an Eu/Ne HCL was conducted with a setup similar to that used for La/Ne work. This lamp, which was purchased from Laboratory Instruments Inc., contained 5 Torr of Neon as the buffer gas. The dye laser with R6G dye, was scanned in 595.0-634.0 nm range. The peak output power of the dye laser was around 250 mW. The chopping frequency was 241 Hz. The lamp was operated in the 4.0-14.0 mA current range. In this range the lamp was found to be stable and noise was low. As in the previous experiments many scans were taken and the spectra recorded.

III.4.3. Results and Discussion

Most of the scans were recorded with very good signal to noise ratio. Fig. III.2 shows one such scan. Using the neon lines in the spectrum as the calibration lines all other lines were measured. The Europium lines were identified by comparing these lines with the work of Russel and King [20]. Table III.4 reports the observed Eu-I lines along with the transition assignments and the energies of the lower and upper levels of the transition. For comparison previously reported wavelengths of these transitions are also presented. No Eu-II lines were observed in this work. This may be due to the low current values used.

All in all 35 Eu-I lines were observed in the 595.0-634.0 nm range. Many lines were found to be very near the neon lines. It may be noted that majority of the transitions recorded

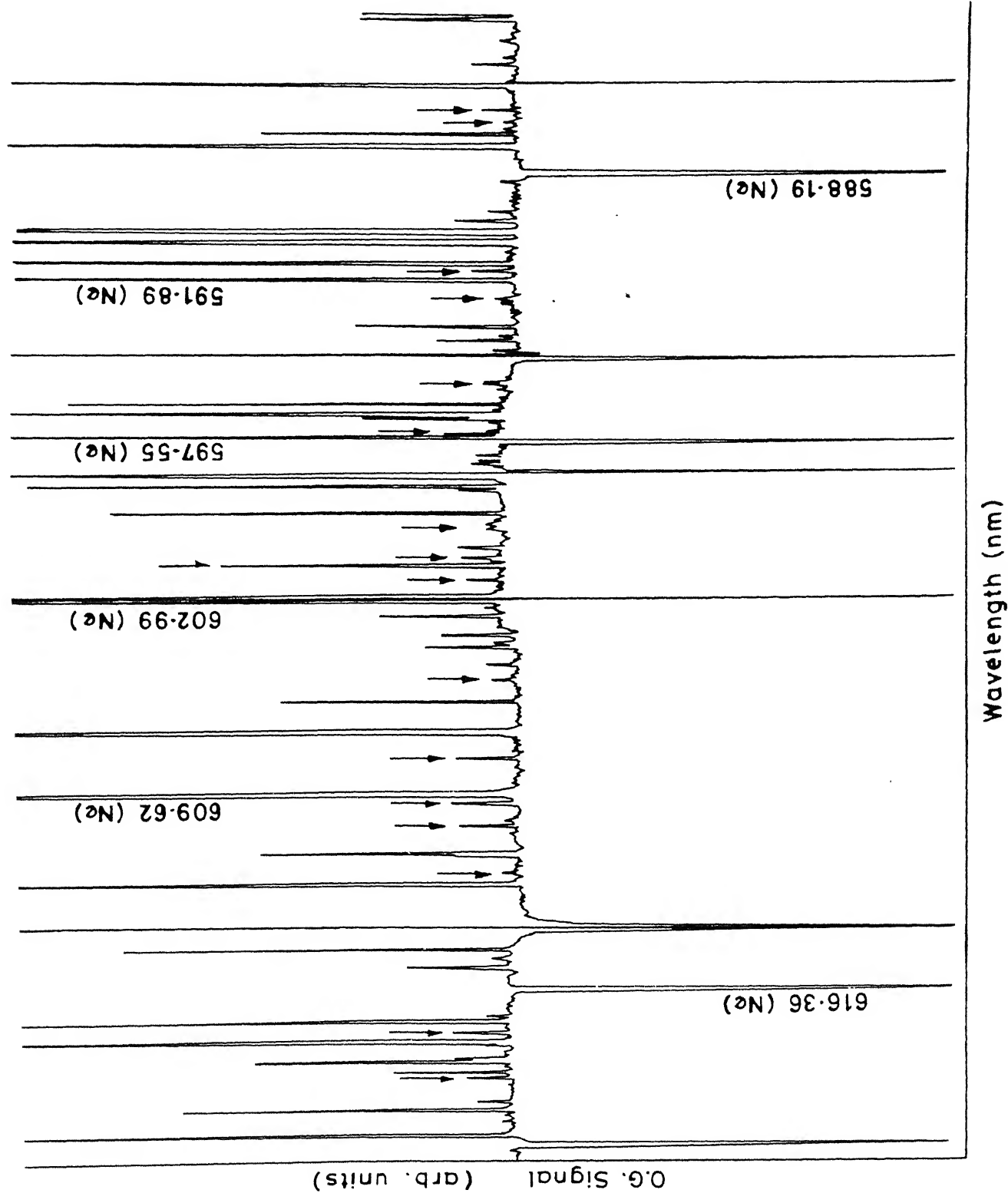


Fig.III.2 Part the optogalvanic spectrum of hollow cathode europium/neon spectral lamp. The peaks marked with arrows are the Eu I transition. The rest are

Table III.4

Transitions of Eu I by Optogalvanic Spectroscopy

Measured Wave- length (nm)	Transition	Wave- length Ref[16] (nm)	Energy(cm ⁻¹)	
			Lower Level	Upper Level
631.42	$a^{10}D_{13/2}^o - z^{10}F_{11/2}$	631.38	13778.68	29612.69
626.65	$a^8S_{7/2}^o - z^8P_{7/2}$	626.69	0.00	15952.31
626.25	$a^{10}D_{9/2}^o - z^{10}F_{9/2}$	626.23	13222.04	29186.32
625.00	$a^{10}D_{5/2}^o - z^{10}F_{7/2}$	625.05	12923.72	28918.17
619.45	$a^{10}D_{7/2}^o - z^{10}F_{9/2}$	619.51	13048.90	29186.32
618.94	$a^{10}D_{11/2}^o - z^{10}F_{11/2}$	618.81	13457.21	29612.69
617.93	$a^6D_{9/2}^o - z^6F_{11/2}$	617.88	19273.24	35453.23
612.46	$a^8D_{5/2}^o - z^8F_{7/2}$	612.47	15248.76	32003.24
611.77	$b^8D_{7/2}^o - 12 (5/2)$	611.88	19712.15	36052.65
610.85	$a^6D_{7/2}^o - z^6F_{9/2}$	610.82	19364.50	35731.62
609.97	$a^{10}D_{9/2}^o - z^{10}F_{11/2}$	609.94	13222.04	29612.69
608.39	$\{ a^{10}D_{13/2}^o - z^{10}F_{13/2} \}$	608.38	13778.68	30211.09
	$\{ y^8P_{7/2}^o - e^6P_{7/2}^o \}$		21606.17	37584.98
605.69	$a^8D_{9/2}^o - z^8F_{9/2}$	605.74	15680.28	32184.65
604.49	$a^8D_{5/2}^o - z^8F_{3/2}$	604.47	15248.76	31787.71
602.33	$a^8D_{3/2}^o - z^8F_{1/2}$	602.32	15137.72	31735.76
601.73	$a^8S_{7/2}^o - z^8P_{9/2}$	601.82	0.00	16611.79
601.58	$a^6D_{5/2}^o - z^6F_{7/2}$	601.56	19462.05	36081.01
601.26	$a^8D_{5/2}^o - z^8F_{5/2}$	601.26	15248.76	31876.09
600.57	$a^8D_{9/2}^o - 116$	600.56	15680.28	32326.73
600.46	$a^8D_{3/2}^o - z^8F_{3/2}$	600.44	15137.72	31787.71

cont'd...

Measured Wave- length (nm)	Transition	Wave- length Ref[16] (nm)	Energy(cm ⁻¹)	
			----- Lower Level	Upper Level
598.41	$a^6D_{7/2}^o - 129(7/2, 9/2)$	598.38	19364.50	36071.71
598.27	$a^8D_{7/2}^o - 115(9/2)$	598.31	15421.25	32130.25
598.09	$a^6D_{7/2}^o - z^6F_{5/2}$	598.05	19364.50	36284.82
597.24	{ $a^8D_{9/2}^o - z^8F_{11/2}$	597.28	15680.28	32418.38
	{ $a^6D_{7/2}^o - z^6F_{5/2}$	597.18	19364.50	36284.82
	{ $b^8D_{3/2}^o - y^8D_{5/2}$	595.43	19794.21	36584.31
595.41	{ $a^6D_{3/2}^o - 131(3/2)$	595.39	19543.69	36334.52
592.58	$a^8D_{11/2}^o - y^{10}P_{11/2}$	595.53	16079.76	32948.41
590.98	$a^8D_{9/2}^o - y^{10}P_{9/2}$	590.99	13222.04	32596.31
590.25	$b^8D_{5/2}^o - y^8D_{7/2}$	590.29	19763.78	36700.39
586.12	$b^8D_{11/2}^o - u^8P_{9/2}$	586.09	19447.19	36504.49
584.63	$b^8D_{11/2}^o - v^8P_{9/2}$	584.58	19447.19	36548.83
583.08	$a^{10}D_{13/2} - z^{10}F_{15/2}$	583.09	13778.68	30211.09
579.36	$b^8D_{9/2}^o - y^8D_{9/2}$	579.27	19631.26	36889.62
578.41	$z^{10}P_{9/2} - e^{10}P_{9/2}^o$	578.37	14563.57	32209.88
573.89	$b^8D_{11/2}^o - y^8D_{11/2}$	573.90	19447.19	36867.04
573.09	$a^{10}D_{11/2}^o - z^8D_{9/2}$	573.09	13457.21	30901.84

originated from $a^{10}D_J^0$, $a^8D_J^0$, $a^6D_J^0$ levels. This shows that these levels are well populated at these current and pressure values. Even at low currents, we could get reasonable number of atoms in excited states with energy as high 21606.17 cm^{-1} and use the laser to further excite these atoms to higher energy states. In this way, the highest level reached in this work was 37584.98 cm^{-1} above the ground level.

Assignments of many Eu-I transitions are still doubtful. One example is the transition with wavelength 608.39nm . It is alternatively assigned either as $a^{10}D_{13/2}^0 \rightarrow z^{10}F_{13/2}$ or $y^8P_{7/2} \rightarrow e^6P_{7/2}^0$. This doubt can be resolved by conducting high resolution experiments and extract the hyperfine structure of the line. This structure may help in assigning the lower and upper levels of the transitions. Presently such high resolution Optogalvanic work is being carried out by us.

Again, this is the first time a broad band Optogalvanic spectrum of Europium is reported.

III.5. CONCLUSIONS

In conclusion it is seen that spectroscopy of rare earths can be conducted conveniently by Optogalvanic techniques. It is also demonstrated that signal to noise ratios of the spectra are very high. Transitions between highly excited levels can be easily studied with this technique. Ionic species of rare earths can also be investigated by this method. This work is necessary as a prelude for conducting high resolution spectroscopy experiments to investigate hyperfine structures of the transitions and

isotope shifts. The saturation characterization studies which are done for neon and lanthanum and presented in Chapter II will help in assessing transitions suitable for conducting Doppler free saturation spectroscopy like Intermodulated Optogalvanic Spectroscopy [IMOGS],[21].

REFERENCES

- [1] Childs, W.J., and Goodman, L.S., *Phy. Rev.*, A24, 1324, (1981)
- [2] Childs, W.J., and Goodman, L.S., *Phy. Rev.*, A33, 1469, (1986)
- [3a] Childs, W.J., and Goodman, L.S., *J.Opt.Soc.Am.*, 73, 151
(1983)
- [3b] Childs, W.J., and Goodman, L.S., *J.Opt.Soc.Am.*, B1, 22,
(1984)
- [4] Paisner, J.A, Solaraz, R.W, Worden, E.F., and Conway, J.G.,
'Laser Spectroscopy III' ed. Hall, J.L., and Carlsten, J.L.,
Opt. Sci.-V7, Springer Verlag (Berlin)
- [5] Keller, R.A., and Zalewski, E.F., *Appl. Opt.*, 19, 3301,
(1980)
- [6] Behrens, H.O., and Guthohrlein, *J.Phys. (Paris)*, Colloq.Sup.,
44, C-7, 149, (1983)
- [7] Meggers, W.F., *J.Res.Nat.Bur.Stand.(USA)*, 9, 239, (1932)
- [8] Fischer, R.A., Knopf, Jr., W.C., and Kinney, F.E., *Astrophys. J.*,
130, 683, (1959)
- [9] Giacchetti, A., and Wilson, M., *J.Opt.Soc.Am.*, 58, 740A,
(1968)
- [10] Ben Ahmed, Z., Verges, J., Wilson, M., and Giacchetti, A.,
Phisica (Utrecht), 84C, 275, (1976)
- [11] Harrison, G.R., Rosen, N., and Mc Nully, Jr., J.R.,
J.Opt.Soc.Am., 35, 658, (1945)
- [12] Childs, W.J., and Goodman, L.S., *Phy. Rev.*, A3, 25, (1971)
- [13] Russel, H.N., and Meggers, W.F., *J.Res.Nat.Bur.Stand.(USA)*, 9,
625, (1932)
- [14] Wilson, M., *Phy. Rev.*, A3, 45, (1971)
- [15] Martin, W.C., Zulubas, R., and Hagen, L., 'Atomic Energy
Levels - Rare-earth elements', NBS-60, *Nat.Stand.Ref.Data.Se*
Nat. Bur. Stand. (USA), April-(1978)
- [16] Meggers, W.F., Corliss, C.H., Scribner, B.F., 'Tables of
spectral intensities - Part II' NBS-MONO-145,
Nat.Bur.Stand.(USA), May -(1975)

- [17] King,A.S., Astrophys. J.,89, 377, (1939)
- [18] Smith,G., and Tomkins,F.S., Proc. Roy. Soc. London,Ser. A 149, 149, (1975)
- [19] Smith,G., and Tomkins,F.S., Philo. Trans. R. Soc. London, Ser. A283, 345, (1976)
- [20] Russel,H.N., and King,A.S., Astrophys. J., 90, 155, (1939)
- [21] Lawler,J.E., Ferguson,A.I., Goldsmith,J.E.M., Jackson,D.J., and Shawlow,A.L., Phy. Rev. Lett., 42, 1046, (1979)

C H A P T E R I V

HYPERFINE STRUCTURE STUDIES OF La I

IV.1. THEORY OF HYPERFINE INTERACTIONS

IV.1.1. Historical sketch

As early as in 1891 Michelson [1] observed still finer structure in the fine structure transitions of atoms. This was further confirmed by the observations of Fabry and Perot in 1897 [2] and Lummer and Geherke in 1903 [3]. Initially it was thought that the whole effect was due to the difference in masses of different isotopes of an element. But the known masses of the different isotopes of an element could not satisfactorily explain the magnitude and structure of the splittings. These splittings of the fine structure are called the hyperfine splittings and the structure the hyperfine structure (HFS). In 1924 Pauli [4] suggested that the structure could be explained by assuming the existence of nuclear dipole moment and its interaction with the valence electrons.

On the theoretical front Fermi [5], Breit [6] and Goudsmith [7] treated HFS quantum mechanically. Relativistic effects were incorporated into the theory by Breit [8] and Racah [9]. Meanwhile Schuler and Schmidt [10] in 1935 demonstrated the existence of quadrupole moments of the nuclei. From these observations Casimir [11] evaluated the magnitude of the quadrupole moment. Besides Casimir and Karreman [12] derived expressions for the octupole moment in 1942. Between the years

1942 and 1949 Racah [13] developed a very elegant and powerful theoretical technique for atomic structure calculations. This theory was applied to explain HFS by Trees [14] in 1953. Schwartz in 1955 [15] combined the Racah's technique and Dirac's relativistic equations to explain the HFS of single electron atoms. Though this method is very elegant it is very unwieldy for numerical calculations. So a new formalism called effective operator formalism was developed by Sanders and Beck [16] in 1965. This simplifies numerical calculations enormously.

The theory of HFS has been reviewed by Lindgren and Rosen [17] and by Armstrong [18]. The theory of HFS of one and two electron atoms was first treated in the book by Kopfermann [19]. The following subsection briefly reviews the theory of HFS of free atoms.

IV.1.2. Introduction to hyperfine interactions

In the theory of atomic structure, as a first approximation the nucleus is assumed to be a point charge of infinite mass. This gives rise to the fine structure of the atomic lines. When the restriction on the mass is removed the fine structure of the different isotopes of an element shift and this is called the isotope shift (IS). There is also a contribution to this due to the distribution of the charge over the nucleus. If now the restriction on the shape and size of the nucleus is also removed, then one can understand and explain the HFS.

Any charge or current distribution can be expanded in terms of multipole moments. Hence a non - spherical nucleus can be considered to possess multipole moments. These nuclear moments

can be electric or magnetic in nature. But due to the symmetry of the nuclear wavefunctions only even magnetic and odd electric moments can exist.

Among magnetic moments of the nucleus the dipole term is dominant. The next order magnetic moment, the octupole moment, is very small and can be inferred only by ultra high resolution spectroscopy. Hence it is neglected in most of the treatments. Similarly among the electric moments only the quadrupole term is retained and the rest of the terms like hexadecapole moments are neglected.

Compared to the Coulomb interaction and the spin orbit interaction the interactions between the nuclear moments and the fields created by the electrons at the nuclei are very weak. Hence the hyperfine interactions can be considered as perturbations to the fine structure Hamiltonian. This approach is followed in the remaining subsections of this chapter.

IV.1.3. Hfs Hamiltonian and the effective operators

The interaction Hamiltonian between the electrons and the nucleus can be expanded in terms of the scalar products of the multipole tensors of rank k. Following the treatment by Schwartz [15] the Hamiltonian can be written as,

$$H = \sum T^k(e) T^k(n) \quad \text{-----(1)}$$

$$= T^0(e) T^0(n) + \sum T^k(e) T^k(n) \quad \text{-----(2)}$$

$$= H_{fs} + H_{hfs} \quad \text{-----(3)}$$

where, $T^k(e)$ and $T^k(n)$ are the spherical tensors representing the electron and the nuclear part respectively. Even k valued tensors

represent the electric moment interactions and the odd k valued tensors represent the magnetic moment interactions. In the above $k = 0$ represents the interaction between the electrons and the spherical part of the nuclear interaction, which is the Coulomb interaction term. Along with the spin - orbit interactions of the electrons this part of the interaction causes the fine structure splittings and the Hamiltonian is given by

$$H_{fs} = \frac{1}{2}m_e \sum_i p_i^2 - \sum_i Ze^2/r_i + \sum_{i \neq j} e^2/(r_i - r_j) + \sum_i \epsilon_i l_i \cdot s_i \quad (4)$$

The summation is over all the electrons, p_i is the momentum of the i^{th} electron and m_e and e are the mass and the charge of the electron respectively. The first term in equation (4) represents the kinetic energy operator of the electrons. The second term represents the monopole electrostatic interaction between the electrons and the nucleus. The third term takes into account electron - electron repulsion and the final term the spin - orbit interaction. l_i and s_i are the orbital and spin angular momenta of the i^{th} electron respectively and ϵ_i the spin - orbit interaction constant. As mentioned previously this gives rise to the fine or the multiplet structure. It is of no further interest here but for the fact that the l_i and s_i join to form J , the total angular momentum. The multiplet states are denoted by $|LSJM\rangle$.

Magnitudes of the hyperfine splittings strongly depend upon the electron wave function near the nucleus. In this region the electrons travel at relativistic velocities. This necessitates the use of relativistic Dirac wave functions for the electrons. As shown by Schwartz [15] calculations with the above wave functions are complicated. However Sanders and Beck [16] have

shown that the matrix elements of true Hamiltonian between LS coupled relativistic state eigen functions can be made equal to the matrix elements of an effective Hamiltonian between corresponding LS coupled non-relativistic eigen functions. It also turns out that the effective Hamiltonian is the same as that in equation (1).

It has been shown that the coupling between the electron and the nucleus gives rise to the HFS. An electronic state can be represented by a wave function with total angular momentum \overline{J} and the nucleus with a nuclear spin momentum \overline{I} . Due to hyperfine interaction \overline{I} and \overline{J} combine to give rise to total angular momentum \overline{F} given as

$$\overline{F} = \overline{J} + \overline{I} \quad \text{-----}(5)$$

Here \overline{I} and \overline{J} are not individually conserved but precess around \overline{F} . This gives rise to a good quantum number F given by

$$F = (I + J), (I + J - 1), \dots, |I - J| \quad \text{-----}(6)$$

These hyperfine structure states are represented by state vectors $|IJFM\rangle$.

To derive HFS splittings of the fine structure levels one has to calculate the first order expectation values of the Hamiltonian, H_{hfs} of equation (2) as

$$E_f = \langle IJFM | H_{\text{hfs}} | IJFM \rangle \quad \text{-----}(7)$$

This is given as

$$E_f = \sum_{k=1}^2 (-1)^{J+I+F} \left\{ \begin{matrix} IJF \\ JIK \end{matrix} \right\} \langle J || T^k(e) || J \rangle \langle I || T^k(n) || I \rangle \quad \text{----}(8)$$

The reduced matrix elements are independent of the magnetic quantum number M. The hyperfine interaction removes the

degeneracy with respect to F . The F dependency is entirely contained in the phase factor and the quantity within the bracket. The 6-j symbols are tabulated in many books [20].

Equation (7) can also be written as

$$E_f = \sum_{k=1}^2 A_k M(IJ;F;k) \quad \text{-----(9)}$$

where A_k 's are denoted by

$$A_k = \langle II | T^k(n) | II \rangle \langle JJ | T^k | JJ \rangle \quad \text{-----(10)}$$

By the application of Wigner - Eckart theorem A_k 's can be related to the reduced matrix elements

$$A_k = \begin{bmatrix} IKJ \\ -IOI \end{bmatrix} \langle I || T^k(n) || I \rangle \begin{bmatrix} JKJ \\ -JOJ \end{bmatrix} \langle J || T_k(e) || J \rangle \quad \text{-----(11)}$$

The quantities in the parenthesis are the 3-j symbols and are tabulated [20].

Nuclear moments: Following the treatment of Lindgren and Rosen [17] the generalized electric multipole moment of the nuclei can be given by

$$Q^k = \langle II | \sum r^k C^k | II \rangle \quad \text{-----(12)}$$

where $|II\rangle$ is the nuclear wavefunction in the state $M_I = I$ and the operator is summed over all the nucleons (with charge q) of the nucleus. Similarly one can get the magnetic moments as

$$\mu^k = \mu_N \langle II | \text{grad}(r^u C^k) [(2/k+1)g_l l + g_s s] | II \rangle \quad \text{-----(13)}$$

Further analysis leads to the following expressions for the requisite nuclear moments

$$\text{Nuclear magnetic dipole moment} = \mu_I = \langle II | T^1(n) | II \rangle$$

$$\text{Nuclear electric quadrupole moment} = Q_I = 2/e \langle II | T^2(n) | II \rangle$$

Substituting the equations (9), (10) and (11) in (8) and

using the explicit values of 3-j and 6-j symbols one gets the Casimir formula

$$E_f = \frac{\hbar A}{2} K + \frac{\hbar B}{4} \frac{(3/2) K(K+1) - 2I(I+1)J(J+1)}{I(2I-1)J(2J-1)} \quad \text{-----(14)}$$

where $K = F(F+1) - I(I+1) - J(J+1)$ and A and B are constants defined as

$$A = A_1/IJ = \langle II | T^1(n) | II \rangle \langle JJ | T^1(e) | JJ \rangle / IJ \quad \text{-----(15)}$$

$$\text{and } B = 4A_2 = 4 \langle II | T^2(n) | II \rangle \langle JJ | T^2(e) | JJ \rangle \quad \text{-----(16)}$$

where A and B are the magnetic dipole constant and the electric quadrupole constant respectively. They can be related to the reduced matrix elements of the tensors $T^1(e)$ and $T^2(e)$ as

$$A = (u_I/I)(J(J+1)(2J+1))^{1/2} \langle J || T^1(e) || J \rangle \quad \text{-----(17)}$$

$$\text{and } B = (2eQ_I)[2J(2J+1)/(2J+3)(2J+2)]^{1/2} \langle J || T^2(e) || J \rangle \quad \text{-----(18)}$$

The explicit operators for the effective tensor operators can be given as

$$T^1(e) = 2u_o \sum_{i=1}^N [1 \langle r_i^{-3} \rangle_{01} - \sqrt{10} (s_i \cdot C_i^2)^1 \langle r_i^{-3} \rangle_{12} + s_i \langle r_i^{-3} \rangle_{10}] \quad \text{-----(19)}$$

and

$$T^2(e) = e \sum_{i=1}^N [-C_i^2 \langle r_i^{-3} \rangle_{02} + (s_i \cdot (C_i \cdot l_i)^3)^2 \langle r_i^{-3} \rangle_{13} + (s_i \cdot l_i)^2 \langle r_i^{-3} \rangle_{10}] \quad \text{-----(20)}$$

where the summation is taken over all the electrons in the open shells, l_i and s_i are the orbital and spin angular momenta of the i^{th} electron, C_q^k are the q^{th} component of a tensor operator of rank k, given as

$$C_q^k = [4\pi/(2k+1)]^{1/2} Y_q^k \quad \text{-----(21)}$$

where Y_q^k are the normalized spherical harmonics. In equations (20) and (21) the radial averages $\langle r_i^{-3} \rangle$ represent the radial

integrals of the type $\int R(r_i) r_i^{-3} R(r_i) dr$, where $R(r_i)$ are the radial parts of the relativistic wave functions.

In the non-relativistic limit $\langle r_i^{-3} \rangle_{01}$ and $\langle r_i^{-3} \rangle_{12}$ go over to $\langle r^{-3} \rangle_{n1}$. $\langle r_i^{-3} \rangle_{10}$ is non zero only for s - electrons and becomes $8\pi |\Psi_s(0)|^2$. In equation (20) the first term represents the magnetic field produced by the orbital motion of the electrons at the nucleus and the second term represents the field produced by the intrinsic spins of the electrons there. The last term is the Fermi contact term of the s - electrons.

Similarly in the non-relativistic limit $\langle r_i^{-3} \rangle_{11}$ and $\langle r_i^{-3} \rangle_{13}$ vanish and $\langle r_i^{-3} \rangle_{02}$ goes over to $\langle r^{-3} \rangle_{n1}$. Hence the only difference between the relativistic and non-relativistic treatment is that in the former case three radial parameters are needed to account for the quadrupole effect where as in the later case one is sufficient. It should also be noted that relativistic effects are very small and it is sufficient if only the first term is taken into consideration for calculations. It should also be pointed out that electronic part in the quadrupole term represents the electric field gradient created by the electrons at the nucleus.

* Comments and deductions from the Casimir formula eq (14),

1. Hyperfine structure is present only for levels with $I \neq 0$ and $J \neq 0$.

2. When $J \geq I$ ($I \geq J$) the number of hyperfine components is equal to $2I + 1$ ($2J + 1$).

3 In the absence of electric interactions the hyperfine splittings obey Lande's interval rule

$$E_F - E_{F-1} = A.F \quad \text{-----(22)}$$

4 Largest splittings are produced by unpaired electrons which approach the nucleus most closely ie. unpaired s electrons.

5. Electric interaction occurs exclusively from electrons with $J \geq 1$, whose superposition does not produce a spherical symmetric charge distribution.

6. Electric interaction energy is non zero only for $I \geq 1$.

7. The quadrupole moment Q measured in experiments is called the spectroscopic quadrupole moment, which is related to the intrinsic quadrupole moment Q_0 of the nucleus by

$$Q = Q_0 I(2I-1)/(I+2)(2I+3) \quad \text{-----}(23)$$

8. The centre of gravity of the hyperfine splitting does not shift since

$$\sum_F (2F+1)E_F = 0 \quad \text{-----}(24)$$

IV.2. HYPERFINE STRUCTURE OF La-I

Lanthanum occurs naturally in two isotopic forms, ^{138}La (0.089%) and ^{139}La (99.911%). The neutral atom has $(5d+6s)^3$ electron scheme which provides a number of closely spaced levels strongly interacting with each other. Presence of such closely packed levels may be regarded as a complication. However, La structure is still sufficiently simple to be susceptible for theoretical treatment.

The study of hfs of La has been going on from nineteen thirties. Anderson [21] has recorded and analyzed the hfs of 512.2 nm, 523.4 nm and 625.0 nm lines of ^{139}La using Fabry-Perot Interferometers (FPI) and confirmed the nuclear spin of ^{139}La as 7/2. Luhrs [22] has conducted similar experiments but with a

higher resolution and has reported the nuclear magnetic dipole and electric quadrupole constants (A and B) of 18 terms of La I and 7 of La II. Murakawa [23,24] and Murakawa and Kamei [25] conducted experiments on La I and La II using FPI to measure the Quadrupole moment (Q) of ^{139}La nuclei. The $5d6s^2\ ^2D_{3/2,5/2}$ levels have been investigated using Atomic Beam Magnetic Resonance (ABMR) technique by Yu Ting [26] to extract the A and B constants of these levels. He has also estimated the Q of ^{139}La to a better accuracy. Similar high resolution ABMR experiments have been performed by Childs and Goodman [27] on $5d^26s$, $5d6s^2$ and $5d^3$ configurations of La I, for levels upto 9000 cm^{-1} from the ground state. They have analyzed their spectra using the effective operator Hamiltonian. They have not only reported the A, B, g and g_J constants of these levels but also have reported C the octupole constant for many levels. Hfs investigations have been conducted by Fischer et al. [28,29] on the unstable ^{137}La and less abundant ^{138}La and they have confirmed I of ^{139}La as 7/2, and reported I of both ^{137}La and ^{138}La as 7/2. They have also reported μ of ^{137}La as 2.69 nuclear magnetons and Q of ^{135}La as 0.51 ± 0.09 barns. Laser-atomic beam fluorescence experiments have been conducted by Childs and Goodman [30,31] using laser radiation of a single frequency dye laser crossed with a well collimated ^{139}La beam. They have recorded Doppler reduced hfs spectra of many ^{139}La transitions. They have reported A and B constants of eleven odd levels of ^{139}La . Behrens and Gutherlein [32] have performed Intermodulated Optogalvanic Spectroscopy (IMOGS) of four La I transitions and have reported A and B

constants of seven levels.

To summarize, the hfs of many La I levels have been investigated in the past to measure the I , μ and Q values. The presently accepted values of I , μ and Q are $7/2$, $+2.7781$ nuclear magneton, 0.23 barns respectively. However, there are still many lines of La which need to be investigated, the study of which will lead to better understanding of the nature of hyperfine interactions in lanthanum.

IV.3. EXPERIMENTAL PROCEDURE

Employing a setup shown in Fig. II.5, we have conducted high resolution Optogalvanic spectroscopy of La I. Lanthanum vapor was produced by the sputtering process in a La/Ne hollow cathode discharge lamp purchased from Laboratory Instruments Inc. With the help of the SPEX double monochromator and the OG lines of neon, we coarsely tuned the ring dye laser to the La optogalvanic lines of interest. Then the electronic controls of the dye laser were utilized to perform the high resolution scans. Hfs of many transitions of La I were recorded after proper choice of lamp currents and scan rates.

As mentioned in Chapter II, the dye laser frequency was monitored using a FPI of 300 MHz FSR. The transmission peaks of this interferometer were recorded along with the signal to serve as frequency markers. These marker peaks also gave information regarding the jumps, mode-hops and non-linearities and intensity variations of the ring dye laser during the scans. Each line was recorded many times to check the repeatability. The linewidth of

the laser was estimated to be $< 10\text{MHz}$. The linear dispersion of the scans were about 150 MHz/mm . The estimated accuracy of the measurements were about $\pm 30\text{MHz}$.

IV.4. RESULTS AND DISCUSSION

We have studied 14 transitions of La I using high resolution optogalvanic spectroscopy. Out of these hfs studies of seven lines are reported for the first time. These studies were conducted over a range 570 nm to 625 nm . Information regarding the lines studied is presented in Table IV.1. The table also contains comments on the recorded profile of each of these lines. In Fig IV.1, part of the level structure scheme of La I atoms containing the transitions and the levels studied in the present work is shown.

Since Doppler limited techniques are employed, the linewidth of the recorded spectrum are dominated by Doppler broadening. Typically the ions of the discharge have $\sim 25\text{ eV}$ energy when they bombard the cathode surface. The atoms and ions emitted by the cathode surface have an energy spectrum upto $\sim 10\text{ eV}$. These ions and atoms are expected to get thermalized soon because of the collisions with the atoms of the buffer gas. However it is interesting to obtain the approximate temperature of the La atoms from the observed widths of the transitions. Assuming that the entire broadening of the hyperfine spectra is due to the Doppler broadening alone which is valid for our experimental arrangement, we calculate the effective temperature T of the atoms in the vapour phase to be 834 K . Because of the Doppler broadening hfs

Table IV.1

List of transitions of La I for which hfs is studied

S. No.	Wavelength (nm)	Transition	Energy (cm ⁻¹)		Comments
			Lower level	Upper level	
1	623.485	$b^2D_{5/2} \rightarrow x^2D_{5/2}^o$	9183.77	25218.25	Six distinct peaks all with shoulders.
2	616.569	$a^4P_{3/2} \rightarrow x^4D_{3/2}^o$	7490.46	23704.76	Four resolved peaks.
3	593.068	$a^2D_{3/2} \rightarrow y^2F_{5/2}^o$	0.00	16856.82	Broad line with pedestal on which are two resolved peaks. FWHM of the structure \sim 4 GHz
4	593.062	$a^2D_{5/2} \rightarrow y^2F_{7/2}^o$	1053.20	17910.18	Broad line with pedestal on which are three resolved peaks. FWHM of the structure \sim 4.5 GHz.
5	585.558	$a^4F_{5/2} \rightarrow y^4F_{3/2}^o$	3010.01	20083.02	Five distinct peaks with fifth having a shoulder.
6	584.8	$J''=5/2 \rightarrow J'=7/2$?	?	Fully resolved structure with twelve alternating big and small peaks
7	582.972	$a^4P_{3/2} \rightarrow z^4S_{3/2}^o$	7490.46	24639.27	Seven visible peaks with seventh one being very broad.
8	582.382	$a^2F_{7/2} \rightarrow x^2D_{5/2}^o$	8052.15	25218.25	Six distinct peaks.

cont'd...

S. No.	Wavelength (nm)	Transition	Energy (cm ⁻¹)		Comments
			Lower level	Upper level	
9	582.199	$a^2G_{7/2} \rightarrow y^2G_{7/2}^o$	9960.96	27132.50	Six distinct peaks with sixth peak with a broad shoulder.
10	579.134	$a^4F_{9/2} \rightarrow y^4F_{9/2}^o$	4121.61	21384.06	Seven distinct peaks with eighth in shoulder
11	576.997	$a^2F_{7/2} \rightarrow v^2F_{7/2}^o$	8052.15	25378.46	Seven distinct peaks with eighth in shoulder
12	574.441	$a^4P_{5/2} \rightarrow x^4D_{7/2}^o$	7679.94	25083.42	Six resolved peaks.
13	574.039	$a^4F_{3/2} \rightarrow y^4F_{3/2}^o$	2668.20	20083.02	Four peaks.
14	573.495	$a^2G_{7/2} \rightarrow u^2F_{5/2}$	9960.96	27393.00	

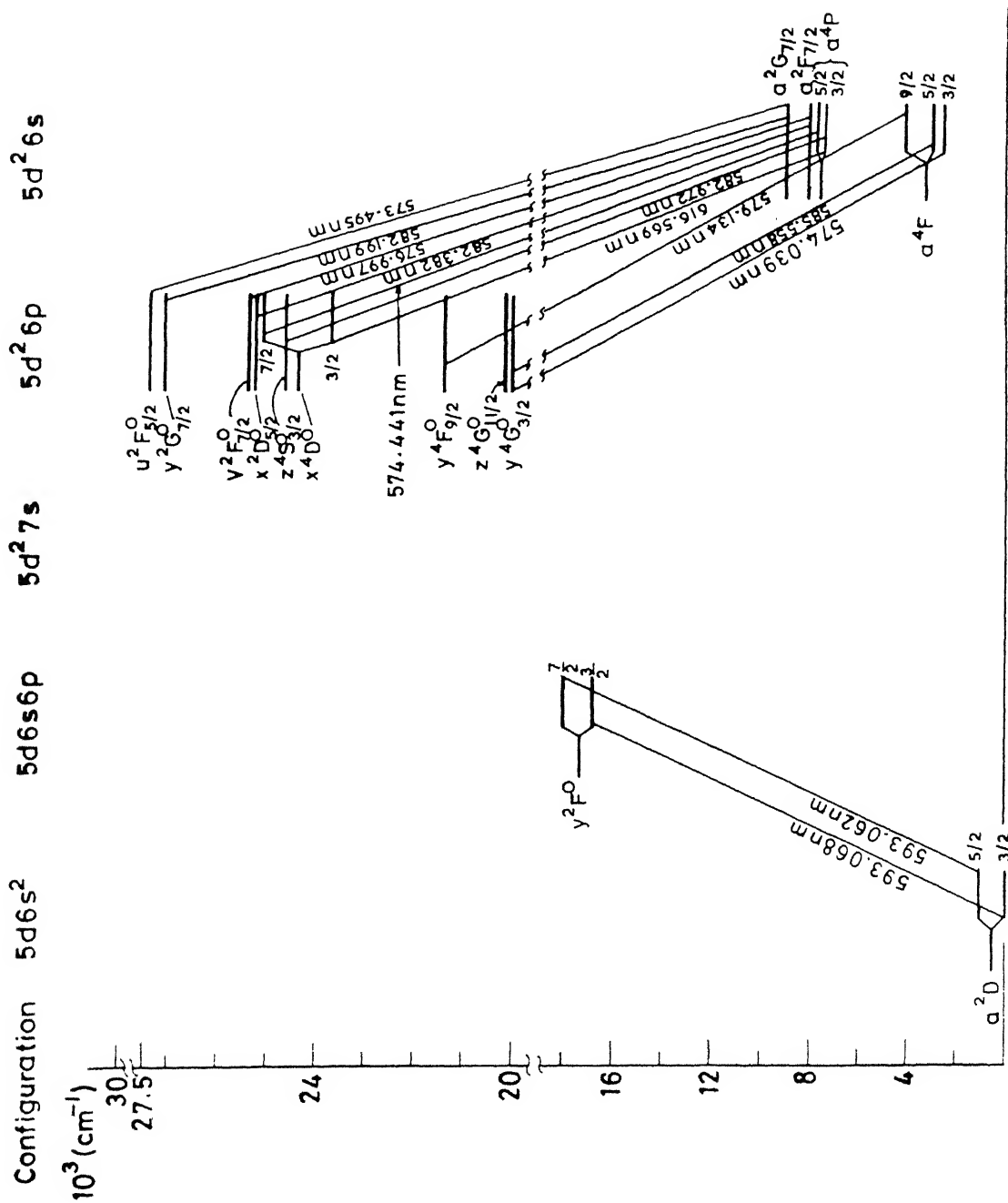


Fig.IV.1 Sketch of the fine structure level scheme of the LaI spectrum. Only the investigated transitions are shown.

of many of the transitions were only partially resolved. However well resolved hyperfine spectra were observed in the transitions 582.972 nm and 584.8 nm. Even with the hollow cathode lamp operating at such low currents as used by us the observed signals were strong with good signal to noise ratio. No appreciable variation of linewidth with the lamp current was observed in any of the transitions studied.

The observed OG relative intensities of different components of the hyperfine structure was not found to follow the relative theoretical intensities strictly [19]. However, there was a qualitative agreement between them in all the lines studied. For example, we have presented observed relative intensities and expected relative theoretical intensities for two of the transitions in Table IV.2. The reason for this non adherence to the theoretical intensity may be due to the fact that the OG signals depend on the saturation properties of the different hyperfine components [34] and the fact that all the hyperfine components are not fully resolved in our spectra. However, the trends of the relative intensities of the hyperfine components compare very well with the expected values and enabled us to obtain precise and unambiguous A values.

Each transition was analyzed in the following way. The configuration, term and J value of upper and lower levels of the transitions were known from the classified transitions table [35]. Nuclear spin of ^{139}La is known as ($I=7/2$). This is also confirmed from the hf splittings of the lines studied in the present work. From these information the hyperfine level schemes of upper and lower levels of the transitions studied are derived.

Table IV.2

Comparison of observed relative O.G. intensities with relative theoretical intensities of some of the hfs components of 576.997 and 574.441 nm transitions of La I

(i) 576.997 nm $a^2F_{7/2} \rightarrow v^2F_{7/2}$

Components	Observed intensity	Theoretical intensity	Sums of theoretical intensities for $F'' \rightarrow F''_{\pm}$ and F'' transitions
7-7	100	100	100
6-6	88	65	87
5-5	89	39	74
4-4	54	21	61
3-3	39	10	47
2-2	29	4	32

(ii) 574.441 nm $a^4P_{5/2} \rightarrow x^4D_{7/2}$

Components	Observed intensity	Theoretical intensity	Sums of theoretical intensities for $F'' \rightarrow F''_{\pm}$ and F'' transitions
6-7	100	100	100
5-6	87	85	85
4-5	76	76	69
3-4	65	56	54
2-3	50	41	38
1-2	35	24	23

It is also possible to draw the theoretical hyperfine structure of each of these lines. We have presented hyperfine structure scheme of the levels involved and the theoretical structures of some of the transitions studied in Fig. IV.2, IV.4, IV.6 and IV.8. By comparing the recorded spectra with the theoretical hyperfine structure we could assign the different peaks to respective hyperfine transitions. Partial resolution of the structure and saturation of lines were taken into considerations while doing these assignments. After the assignment the peak separation were measured to calculate the splitting constants. We have presented the recorded profiles of seven of the transitions studied in Figs IV.3, IV.5, IV.7 and IV.9 to IV.12.

The measured splittings were used to extract A constants of these levels. As can be seen from Casimir formula eq (14) the contribution of electric quadrupole interaction to the splitting is generally less than that of the magnetic dipole interaction, and particularly in the case of La the B values are much smaller than the A values. Hence the effect of B on the hfs splittings is very small. The Doppler limited resolution of our recorded structures and the small dispersion of our recorded spectra limit the accuracy of measurement of the separations of hfs components. So we have neglected the effect of quadrupole interaction in our analysis. Moreover, when the A constants are the dominant factors in determining the structure, the splittings follow the Lande interval rule and the overall structure has the so called Flag Pattern [19]. These features were found in almost all the spectra recorded by us. This is a further justification for neglecting the contribution of B constant in our analysis.

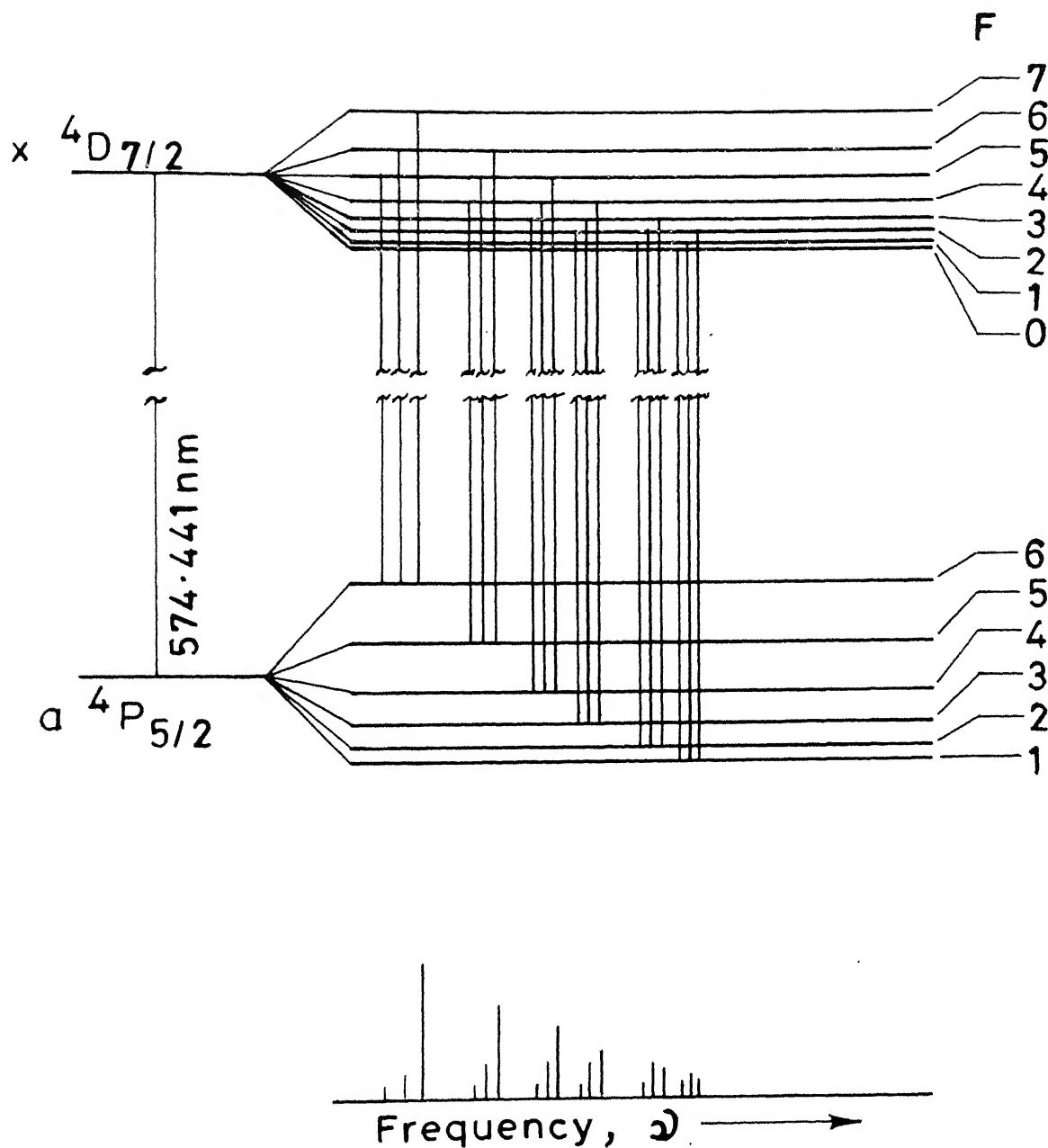


Fig.IV.2 Hyperfine level scheme and theoretical hfs of the La I line $\lambda = 574.441 \text{ nm}$.

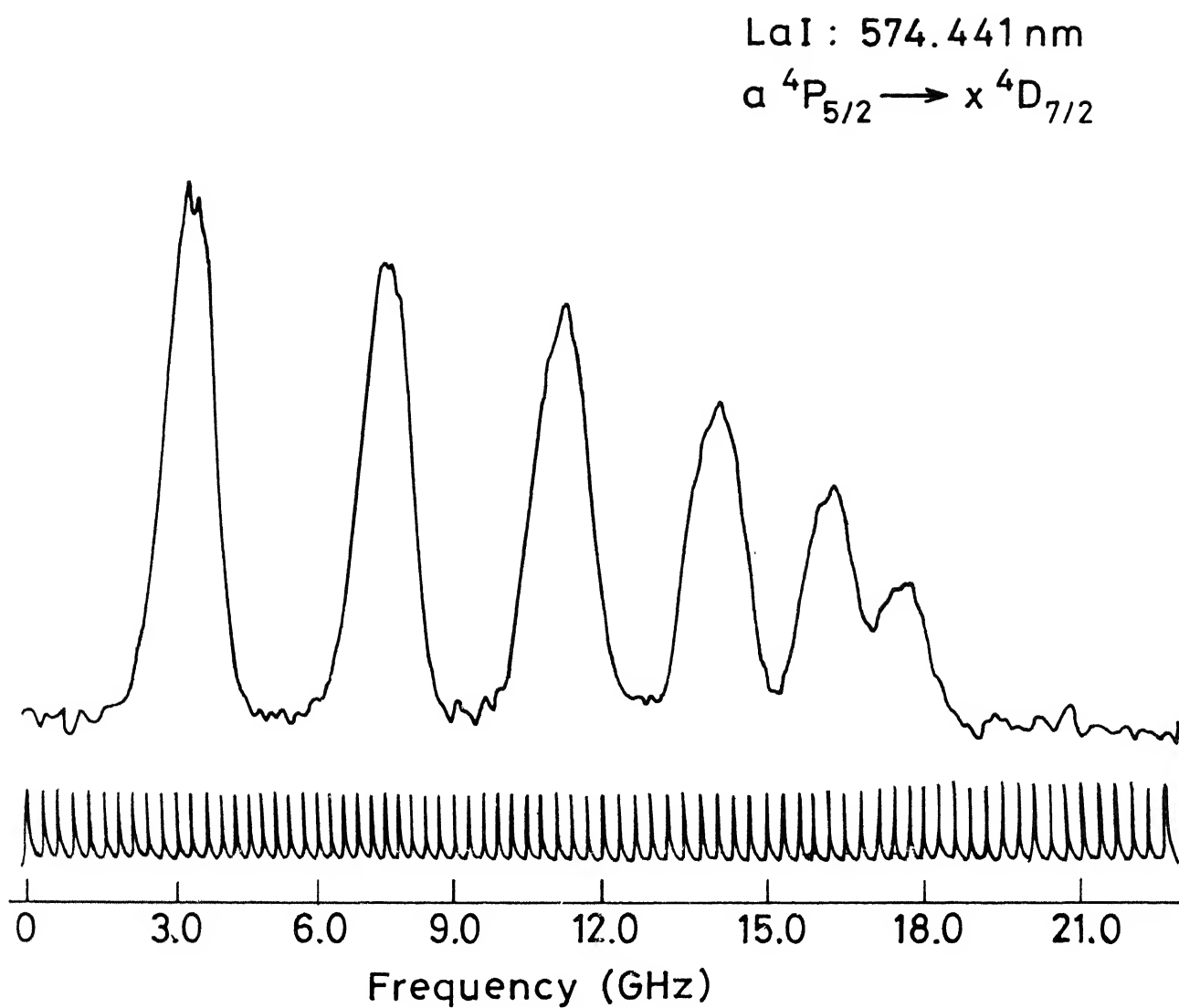


Fig. IV.3 Recorded hyperfine structure of 574.441 nm transition of LaI .

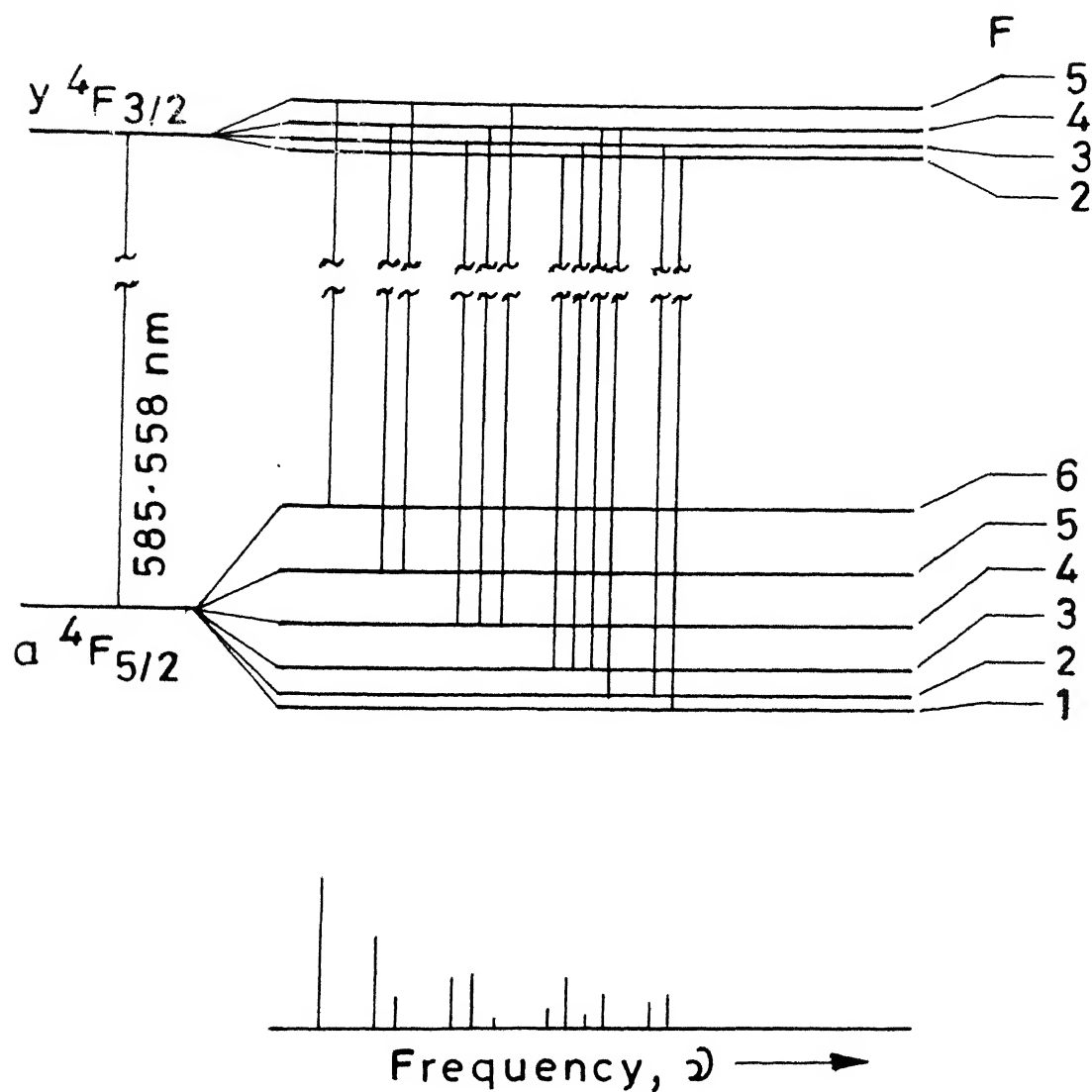


Fig.IV.4 Hyperfine level scheme and theoretical hfs of LaI line $\lambda = 585.558\text{ nm}$.

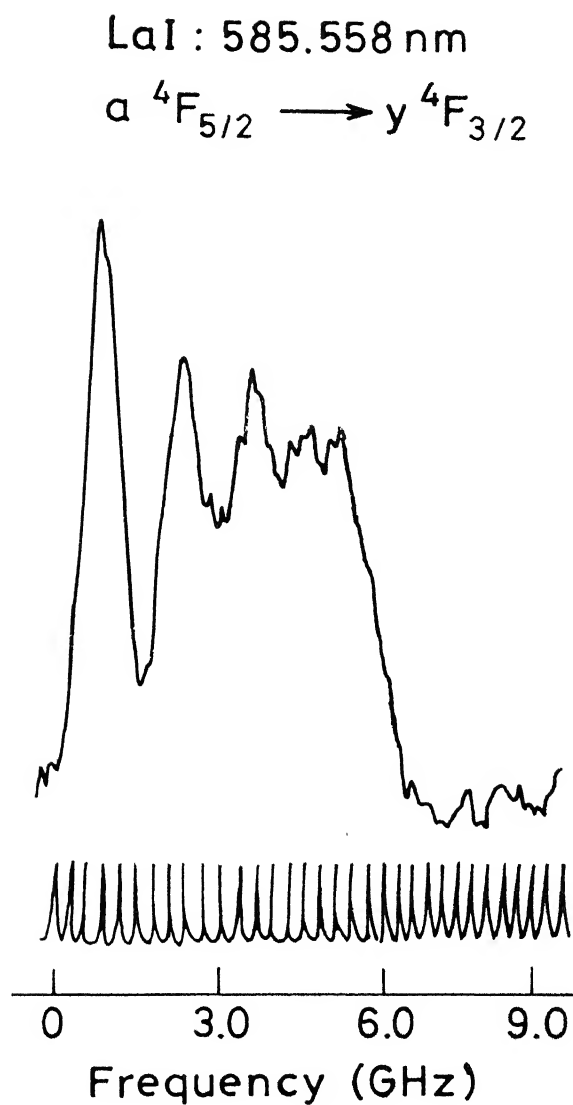


Fig. IV.5 Recorded hyperfine structure of 585.558 nm transition of LaI.

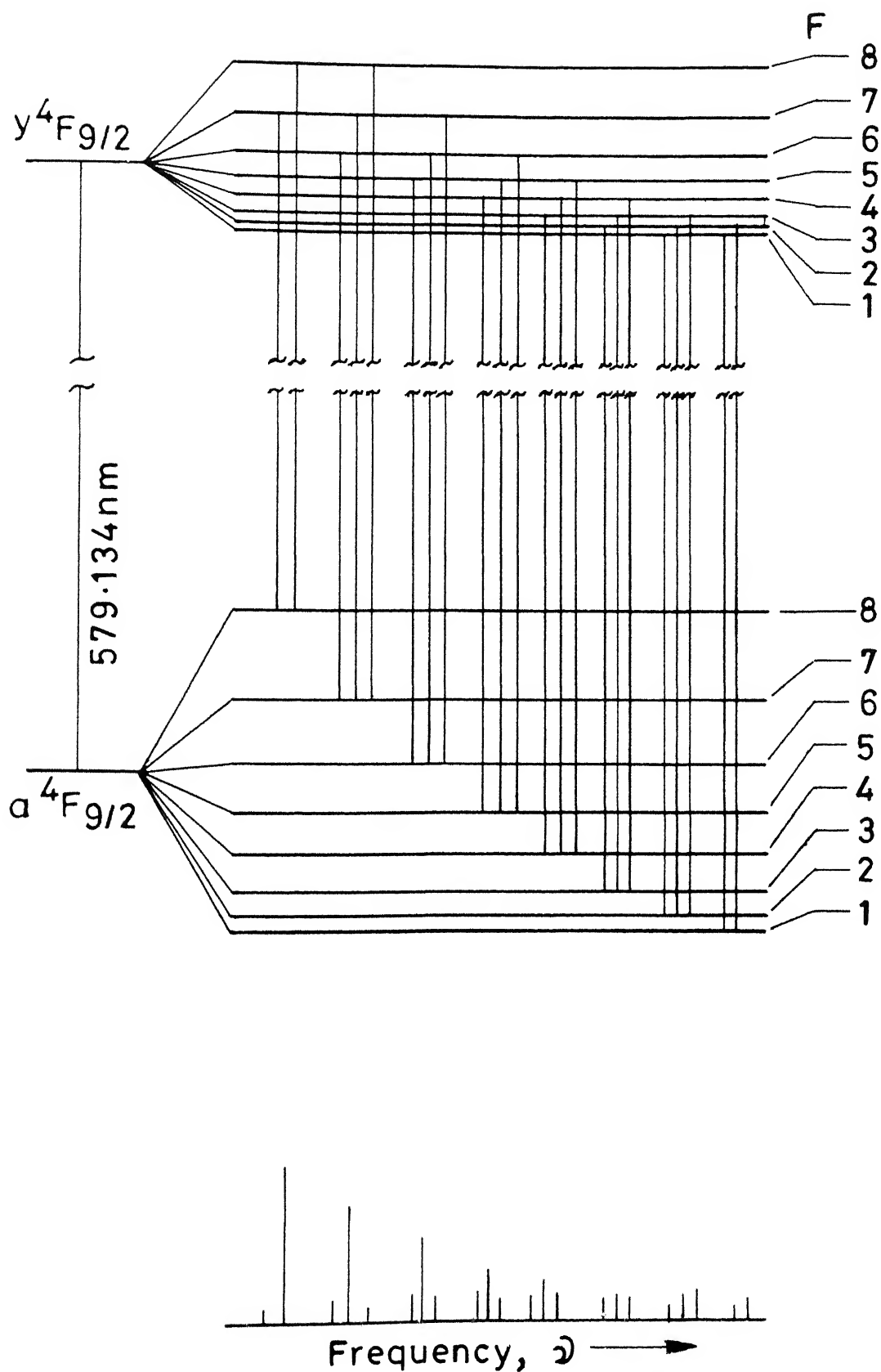


Fig.IV.6 Hyperfine level scheme and theoretical hfs of the LaI line $\lambda = 579.134 \text{ nm}$.

LaI : 579.134 nm
 $a\ ^4F_{9/2} \longrightarrow y\ ^4F_{9/2}$

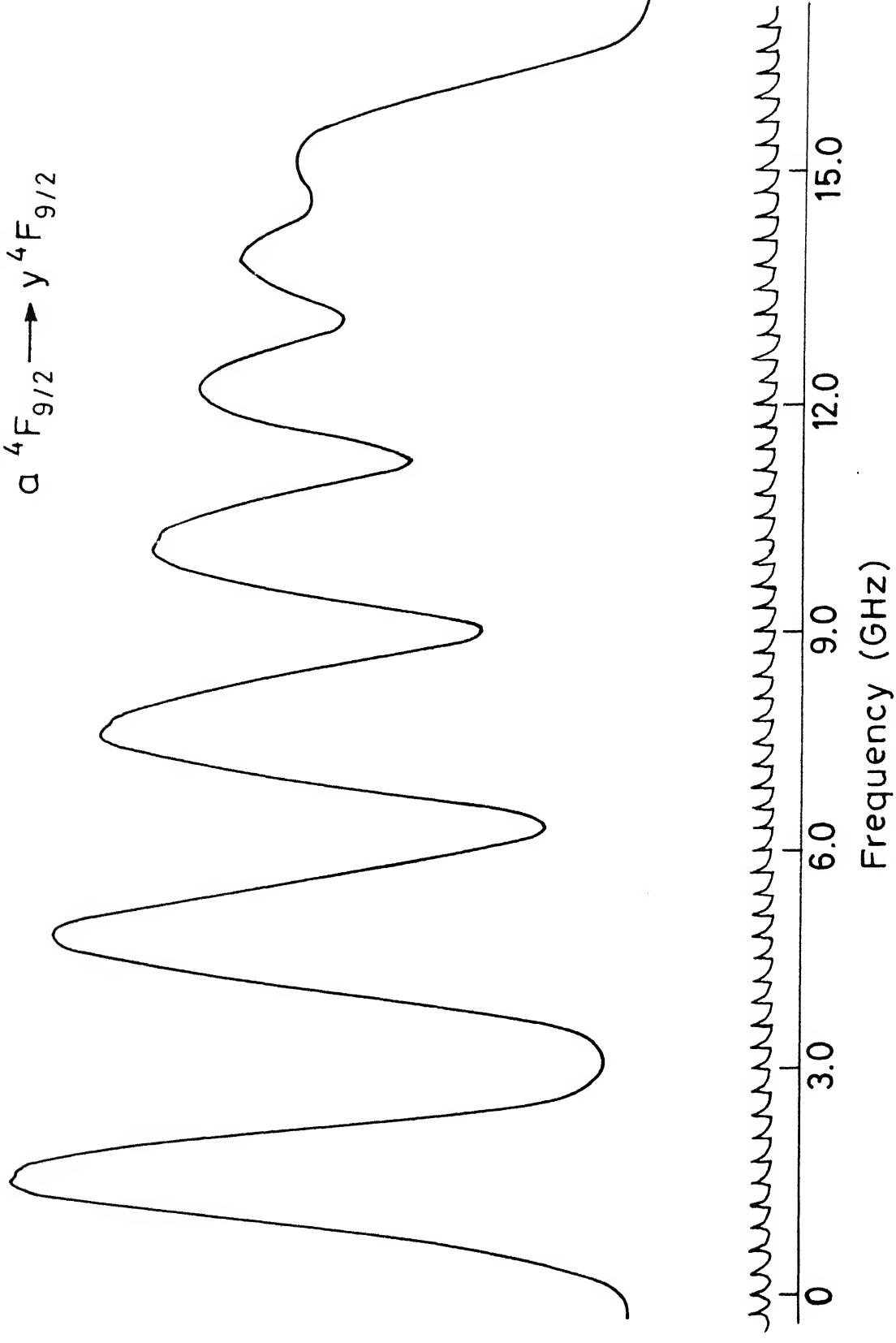


Fig.IV.7 Recorded hyperfine structure of 579.134 nm transition of LaI .

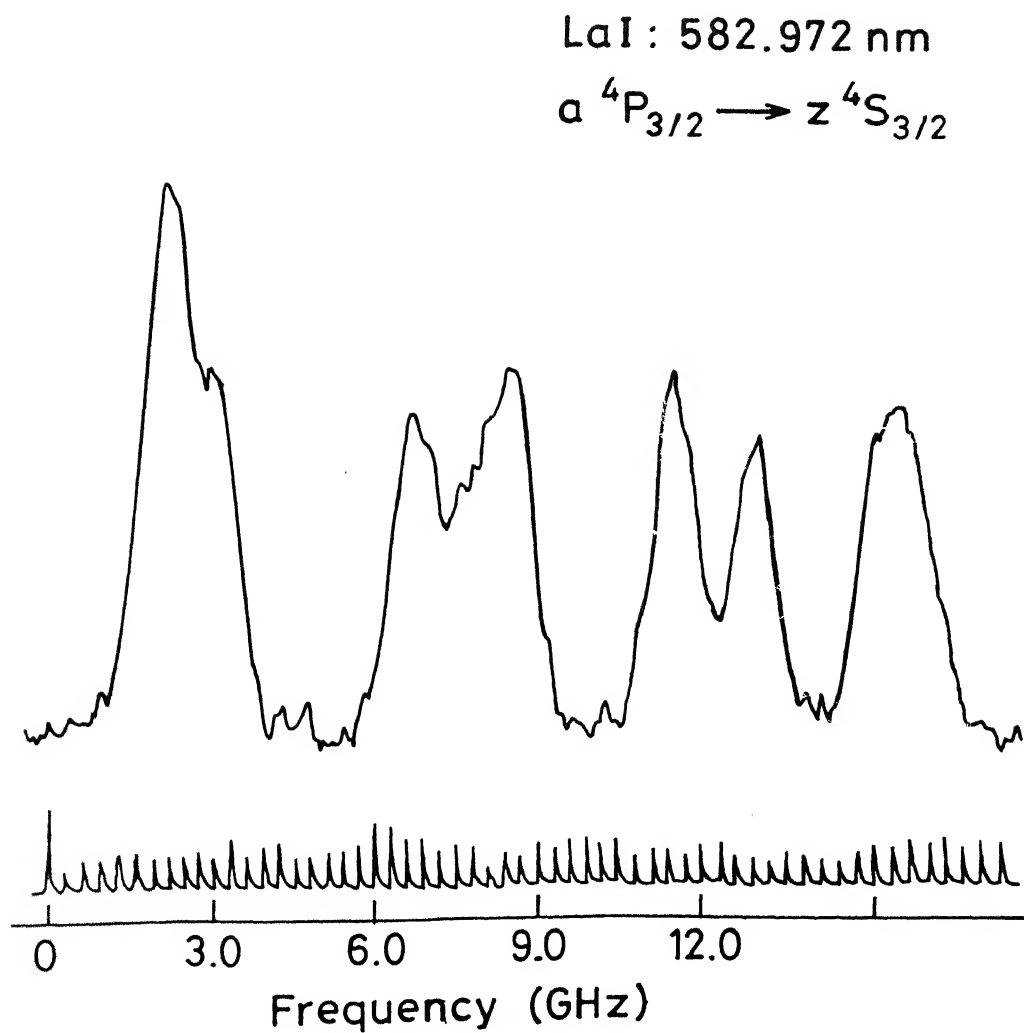


Fig. IV.9 Recorded hyperfine structure of 582.972 nm transition of LaI.

LaI : 584.8 nm

$J'' = 5/2 \rightarrow J' = 7/2$

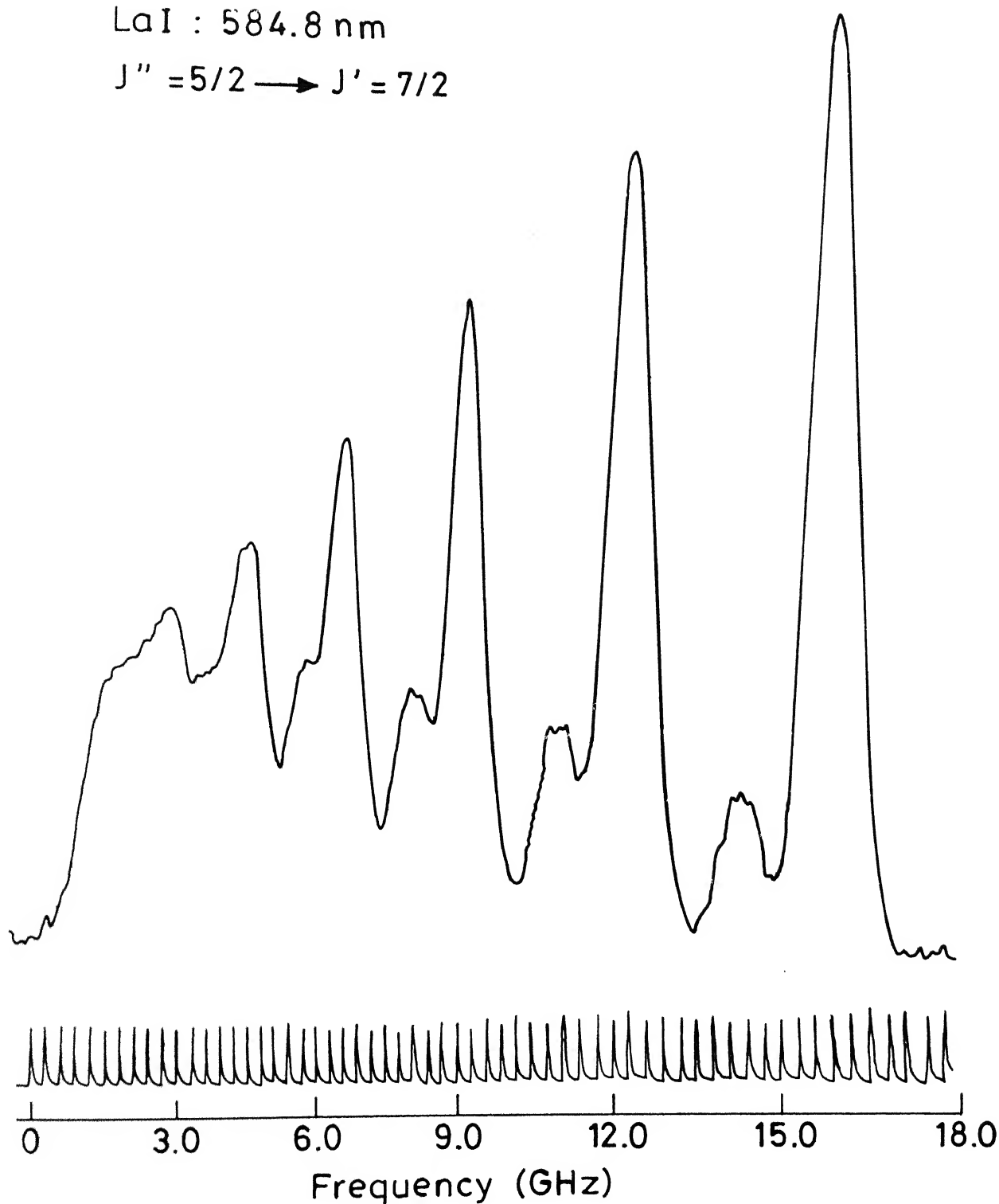


Fig. IV.10 Recorded hyperfine structure of some transition of LaI near 584.8 nm.

LaI : 576.997 nm

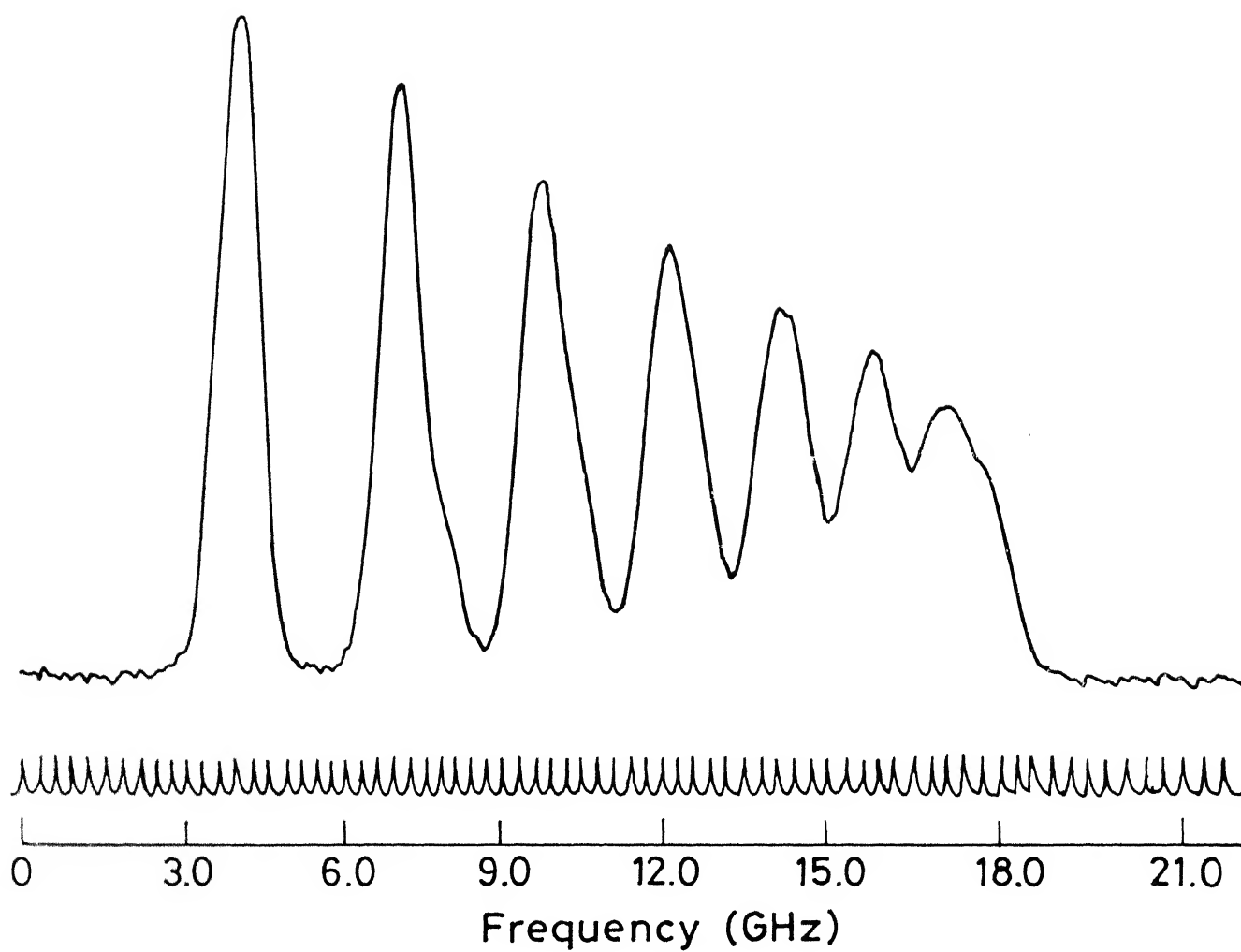


Fig. IV.11 Recorded hyperfine structure of 576.997 nm transition of LaI .

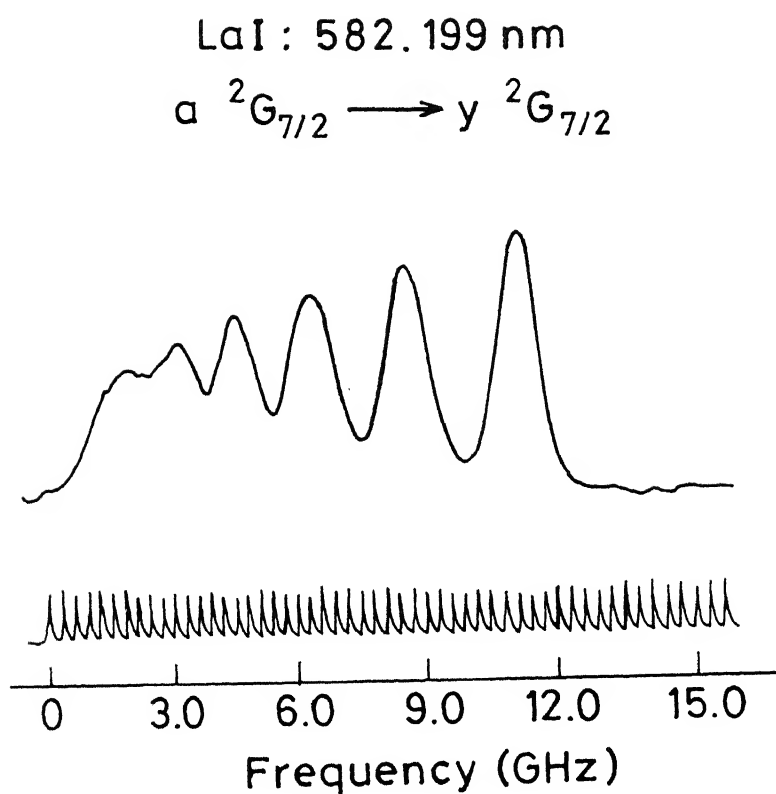


Fig. IV.12 Recorded hyperfine structure of 582.199 nm transition of LaI .

By neglecting the electric quadrupole interaction term in the Casimir formula eq (14) we get an expression for the difference in energy between levels of an hfs multiplet as,

$$W_{F1} - W_{F2} = A/2 (K_1 - K_2) \quad \text{-----(25)}$$

where,

A = Magnetic dipole constant of that level

$F1$ & $F2$ = Total angular momentum quantum numbers of those levels

$$K_i = F_i(F_i+1) - I(I+1) - J(J+1)$$

Eq (25) is used in all our analysis.

Further analysis was performed in two stages. In the first stage, both the upper and lower level A constants (A' and A'' resp.) were treated as unknowns. Then from the measured splittings and the equations derived from Eq (25) A'' and A' were extracted. Whenever there are two or more lines starting from a common level the A values are calculated observing the self consistency. We have also compared the lower level A constants calculated with those reported in the literature. We have presented these results in Table IV.3. It can be seen that the A'' calculated compare well with those available in the literature, within the limits of our experimental accuracy, thus confirming our assignment. The disagreement between our value and the value available in the literature for a $^2D_{5/2}$ level is probably because the hyperfine splittings in this case are small. Doppler free techniques are necessary to obtain more precise A values.

In the second stage of the analysis, in order to increase the accuracy of the calculated upper A constants (A') we used A''

Table IV.3

Experimental A constants (in MHz) for lower levels of some
transitions of ^{139}La

S. No.	Level	Energy (cm^{-1})	A (MHz)		Ref.
			This work	Other work	
1	$5d6s^2 a^2 D_{3/2}$	0.00	147(6)	141	[26]
2	$5d6s^2 a^2 D_{5/2}$	1053.20	210(5)	182	[26]
3	$5d^2 6s a^4 F_{3/2}$	2668.20	-480(6)	-480.312(2)	[27]
4	$5d^2 6s a^4 F_{5/2}$	3010.01	300(5)	300.563(1)	[27]
5	$5d^2 6s a^4 F_{9/2}$	4121.61	495(4)	489.534(1)	[27]
6	$5d^2 6s a^4 P_{3/2}$	7490.46	936(6)	930.0 ± 0.2	[27]
7	$5d^2 6s a^4 P_{5/2}$	7679.94	810(5)	802.8 ± 0.5	[27]
8	$5d^2 6s a^2 F_{7/2}$	8052.15	-197(4)	-197.066(6)	[27]
9	$5d^2 6s a^2 G_{7/2}$	9060.96	-300(4)	-289.113(23)	[32]
10	$5d^2 6s b^2 D_{5/2}$	9183.77	520(5)	-	
11	? $5/2$?	325(5)	-	

values from the literature. This is due to the fact that these A'' values were more accurate than ours, since Doppler free ABMR [27], Laser atomic beam fluorescence [30-31], IMOGS [32] techniques were employed by these authors.

In this way we have calculated A constants of upper levels of all the transitions studied. Table IV.4 presents these A' values. We have also presented previously reported values of A' wherever applicable.

The spectrum of the transition with wavelength 582.972 nm was analyzed in a slightly different way owing to the better resolution of its structure. This line is a $a^4P_{3/2} \rightarrow z^4S_{3/2}^o$ transition and should have 10 hfs components where one of the components ($F'' = 3 \rightarrow F' = 3$) has zero theoretical intensity. Observation of Fig. IV.9 shows seven of these components are well resolved. We used a computer program to least square fit Gaussian curves (Doppler profiles) of the type

$$I(v) = I_0 \text{Exp} -[(v - v_0)/\delta v]^2 \quad \text{-----}(26)$$

to each of the peaks expected in the whole profile. In the above expression I_0 is the relative intensity, v_0 is the position and δv is the linewidth of each peak. I_0 , v_0 , δv were treated as free parameters. It was assumed that v is constant for all the peaks fitted. Using the initial guess for I_0 , v_0 , δv we have fitted 9 peaks to the recorded profile. The results of the computer fits are presented in Table IV.5. Once again we see that the fitted relative intensities follow the theoretical ones only qualitatively. From the calculated positions we extracted the A constants in the same way as was done for the other lines.

Table IV.4

Experimental A constants (in MHz) for upper levels of some transitions of ^{139}La

S. No.	Level	Energy (cm^{-1})	A (MHz)		Ref.
			This work	Other work	
1	$5d6s6p \ y \ ^2F_{3/2}^o$	16856.82	268(6)	262.5 ± 0.3	[30]
2	$5d6s6p \ y \ ^2F_{7/2}^o$	17910.18	280(4)	279.4 ± 0.3	[30]
3	$5d^26p \ y \ ^4F_{3/2}^o$	20083.02	91(6)	87.0 ± 0.5	[31]
4	$5d^26p \ y \ ^4F_{9/2}^o$	21384.06	96(4)	93.4 ± 0.3	[31]
5	$5d^26p \ x \ ^4D_{3/2}^o$	23704.76	156(6)	-	
6	$5d^26p \ z \ ^4S_{3/2}^o$	24639.27	-232(6)	-	
7	$5d^26p \ x \ ^4D_{7/2}^o$	25083.42	77(4)	-	
8	$5d^26p \ x \ ^2D_{5/2}^o$	25218.25	100(5)	$96.624(9)$	[32]
9	$v \ ^2F_{7/2}^o$	25378.46	197(4)	-	
10	$5d^26p \ y \ ^2G_{7/2}^o$	27132.50	-88(4)	$73.935(76)$	[32]
11	$5d^26p \ u \ ^2F_{5/2}^o$	27393.00	-153(5)	-	
12	? $7/2$?	336(4)	-	

Table IV.5

Pertinent data for hfs components of the transition
 $^4P_{3/2} \rightarrow ^4S_{3/2}$ (582.972 nm) shown in Fig. IV.9.

Sl. No.	Calculated relative position MHz	Calculated relative intensity	J→J'	F→F'	Expected relative intensity Ref [19]
1	0	100.0	3/2→3/2	5→5	100.0
2	1008	63.2	"	5→4	38.8
3	4749	58.0	"	4→5	38.8
4	5808	41.9	"	4→4	24.2
5	6501	56.0	"	4→3	50.4
6	9465	58.5	"	3→4	50.4
7	10881	57.9	"	3→2	37.8
8	13059	49.2	"	2→3	37.8
9	13746	37.4	"	2→2	25.2

In our measurements the errors were mainly due to the visual estimates made between the marker peaks. Estimates could be done upto 0.2 of the marker to marker distance. This works out to an error of 60 MHz. Because of this the final calculated errors in A' can be given as

$$\begin{aligned}\delta v_{\text{error}} &= E(v)/(F-1) && \text{for } \Delta J = -1 \text{ Transitions} \\ &= E(v)/F && \text{for } \Delta J = 0 \text{ Transitions} \\ &= E(v)/(F+1) && \text{for } \Delta J = +1 \text{ Transitions}\end{aligned}$$

where $E(v)$ is the measurement error in splitting.

These are the errors quoted in Table IV.4.

Observation of Table IV.4 shows that the values of A' reported by us compare well with those reported for them previously. We are presenting A constants of 8 levels of ^{139}La for the first time. These levels have the excitation energies, 9183.77 cm^{-1} , 20117.4 cm^{-1} , 23704.7 cm^{-1} , 24639.2 cm^{-1} , 25083.4 cm^{-1} , 25378.4 cm^{-1} , 27393.0 cm^{-1} and an unknown level. Some of these A values reported are for highly excited levels. This was possible because of LOGS technique employed for these studies.

In addition to the above discussed lines we have also recorded a line near 584.8 nm. Initially it was thought to be 584.838 line corresponding to $z^4F_{3/2} \rightarrow e^4F_{5/2}$ transition of La I. But neither the intensities of the components nor the separations between them are consistent with the above assignment. Hence attempts were made to see if it is any other transition near by. But none of the reported lines near 584.8 nm explain the observed hfs. So different $J'' \rightarrow J'$ combinations

were tried to account for the observed splittings and the relative intensities of the components. It was found that a $J'' = 5/2 \rightarrow J' = 7/2$ transitions account for the observed intensity pattern to a good extent. For this transition one expects $\Delta F = -1$ to have high intensity, $\Delta F = 0$ to be less intense and $\Delta F = +1$ to be of negligible intensity. In the present spectrum we observed 12 well resolved components with their intensities fairly following the theoretical intensities. The recorded spectrum is shown in Fig. IV.10 and the observed and theoretical intensities are tabulated in Table IV.6. With this assignment the A constants for the upper and lower levels are calculated to be $A'' = 248$ MHz and $A' = 336$ MHz. These constants are the averages of the values obtained from different combinations, which show very good agreement among themselves. These A values were compared with the previously reported values for other $5/2$ and $7/2$ levels and it was found that $y^2F_{5/2}$ and $y^4F_{5/2}$ [31] have comparable values. No such agreement was found for $J = 7/2$. Attempts are made to assign the exact terms corresponding to the upper and lower level of the transition. We believe that these data correspond to another transition close to the 584.8 nm line which is not reported so far.

As detailed earlier, collection of precise hyperfine structure data of a number of levels is of considerable importance. For example, the large number of precise experimental dipole and quadrupole hfs constants (A and B values) can be reduced to a much smaller number of radial integrals and best values of the single electron parameters [30,31]. These values

Table IV.6

Pertinent data for hfs components of the transition
 $J''=5/2 \rightarrow J'=7/2$ (near 584.8 nm) shown in Fig. IV.10.

Sl. No.	Measured relative position MHz	Measured relative intensity	$J \rightarrow J'$	$F \rightarrow F'$	Expected relative intensity Ref [19]
1	0	100	5/2- \rightarrow 7/2	6- \rightarrow 7	100
2	1740	17	"	6- \rightarrow 6	14
3	3690	84	"	5- \rightarrow 6	72
4	5190	24	"	5- \rightarrow 5	23
5	6810	69	"	4- \rightarrow 5	50
6	8040	28	"	4- \rightarrow 4	26
7	9390	54	"	3- \rightarrow 4	31
8	10380	31	"	3- \rightarrow 3	24
9	11430	43	"	2- \rightarrow 3	17
10	12180	--	"	2- \rightarrow 2	20
11	12870	36	"	1- \rightarrow 2	7
12	-	--	"	1- \rightarrow 1	13

can be compared with ab initio relativistic self consistent theoretical calculations [36].

IV.5. CONCLUSIONS

In summary, we have conducted high resolution optogalvanic spectroscopy experiments on 14 allowed transitions of ^{139}La to study the hyperfine structures. These structures were recorded with good signal to noise ratio using laser optogalvanic spectroscopy. Seven of the transitions were studied for the first time in high resolution.

A constants have been extracted for 23 levels of ^{139}La . These values compare well with those previously reported in the literature. A constants of 8 of these levels are reported for the first time. These values are useful in further understanding the nature of the hyperfine interactions in La. The hyperfine interaction studies using high resolution spectroscopy techniques are extremely useful for the classification of the spectral lines. Precise hyperfine structure data of a number of levels is of considerable importance to check the validity of the ab initio theoretical calculations.

Both A and B values can be obtained with better accuracy by Doppler free experimental techniques like IMOGS. The studies conducted in this thesis are necessary preliminaries for such high resolution studies. Presently, experiments are underway to carry out IMOGS on the lines studied.

REFERENCES

- [1] Michelson, A., Phil. Mag., 31, 338, (1891)
- [2] Fabry, C., and Perot, A., Ann. Chem. et. Phys., 12, 459, (1897)
- [3] Lummer, O., and Gehrcke, E., Ann. Phys., 10, 457, (1903)
- [4] Pauli, W., Naturwissenschaften, 12, 74, (1924)
- [5] Fermi, E., Z. Physik, 60, 320, (1930)
- [6] Breit, G., Phys. Rev., 37, 51, (1931)
- [7] Goudsmith, S., Phys. Rev., 37, 663, (1931)
- [8] Breit, E., Phys. Rev., 38, 465, (1931)
- [9] Racah, G., Z. Physik, 71, 431, (1931); Racah, G., Nuevo Cimento, 8, 178, (1931)
- [10] Schuler, H., and Schmidt, T., Z. Physik, 94, 457, (1935)
- [11] Casimir, H.B.G., 'On the Interactions between Atomic Nuclei and Electrons' (Teyler's Tweede Genootschap, Haarlem, 1936; W.H. Freeman, San Francisco, 1963)
- [12] Casimir, H.B.G., and Karreman, G., Physica, 9, 494, (1942)
- [13] Racah, G., Phys. Rev., 62, 438, (1942); Racah, G., Phys. Rev., 63, 367, (1943); Racah, G., Phys. Rev., 76, 1352, (1949)
- [14] Trees, R.E., Phys. Rev., 92, 308, (1953)
- [15] Schwartz, C., Phys. Rev., 97, 380, (1955)
- [16] Sanders, P.G.H., and Beck, J., Proc. Roy. Soc. (London), **A289**, 97, (1965)
- [17] Lindgren, I., and Rosen, A., Case Stud. At. Phys., 4, 93 - 197, (1974)
- [18] Armstrong, L., Jr., 'Theory of Hyperfine Structure of Free Atoms', Wiley - Interscience, New York, (1971)
- [19] Kopfermann, H., 'Nuclear Moments', Academic Press Inc., New York, (1958)
- [20] Rotenberg, M., Birens, R., Metropolis, N., and Wooten, J.K., Jr., 'The 3-j and 6-j symbols', The Technology Press, MIT, Cambridge, Mass., (1958)

- [21] Anderson, O.E., Phys. Rev., **45**, 685, (1934)
- [22] Luhrs, G., Z. Physik, **144**, 486, (1955)
- [23] Murakawa, K., J. Phy. Soc. Jap., **9**, 391, (1954)
- [24] Murakawa, K., J. Phy. Soc. Jap., **10**, 927, (1955)
- [25] Murakawa, K. and Kamai, T., Phys. Rev., **92**, 325, (1953)
- [26] Yu Ting, Phys. Rev., **108**, 295, (1957)
- [27] Childs, W.J. and Goodman, L.S., Phys. Rev., **A 3**, 25, (1971)
- [28] Fisher, W., Huhnermann, H. and Mandrek, K., Z. Physik, **254**, 127, (1972)
- [29] Fisher, W., Huhnermann, H. and Mandrek, K., Phys. Lett., **40B**, 87, (1972)
- [30] Childs, W.J. and Goodman L.S., J. Opt. Soc. Am., **67**, 1230, (1977)
- [31] Childs, W.J. and Goodman L.S., J. Opt. Soc. Am., **68**, 1348, (1978)
- [32] Behrens, H.O. and Guthohrlein, J. de Physique, **44**, Coll 7, C7-149, (1983)
- [33] Demtroder, W., 'Lasers Spectroscopy - Basic Concepts and Instrumentation', Second Corrected Printing, Spri. Ser. in Chem. Phys. 5, Spri. Verlag, Berlin, 1982.
- [34] Engleman Jr and Keller, R.A., J. Opt. Soc. Am., **B2**, 897, (1985)
- [35] Russel, H.N., and Meggers, W.F., J. Res. Nat. Bur. Stand. (USA), **9**, 625, (1932)
- [36] Cheng, K.T., and Childs, W.J., Phys. Rev., **A31**, 2775, (1985)

C H A P T E R V

STUDY OF RYDBERG STATES OF ATOMIC CESIUM

V.1. INTRODUCTION

V.1.1. Rydberg states and Rydberg spectroscopy

Rydberg states are the highly excited states of an atom, with its valence electron in a state with high principle quantum number n . Atoms in Rydberg states are called Rydberg atoms. Rydberg spectroscopy studies the physical and dynamical characteristics of the Rydberg atoms. The properties of the Rydberg atoms are dramatically different from that of atoms in the low excited states. As an illustration, some properties of Rydberg states of Sodium and their scaling with respect to n are given in Table V.1 [1].

In Rydberg atoms the valence electron spends most of its time in a region far away from the nucleus and the core electrons. Because of this reason the valence electron is loosely bound to the atom and the system as a whole is very fragile. These atoms have very large radius and are highly susceptible to external perturbations like electric, magnetic and electromagnetic fields. They also have large collisional cross sections compared to atoms in low excited states. Since the overlap between the wavefunction of the valence electron and the core electron is small the transition probabilities from these states to lower states are also small. This explains the long lifetimes of the Rydberg levels, sometimes extending even to milliseconds. However the transitions between Rydberg states are highly probable since they

TABLE V.1

Properties of Rydberg atoms and their dependence on 'n'

Property	n-Dependence	Na (4d)	Na (10d)
Atomic Radius	n^2	$21 a_0$	$147 a_0$
Binding Energy	n^{-2}	0.68 eV	0.14 eV
Energy between adjacent n - states	n^{-3}	0.31 eV	0.023 eV
Geometric cross section	n^4	$1400 a_0^2$	$68000 a_0^2$
Dipole Moment $\langle nd / r / nf \rangle$	n^2	$16 a_0$	$143 a_0$
Polarizability	n^7	115 MHz/KV/cm^2	0.21 MHz/V/cm^2
Radiative Life time	n^3	57 nsec	1.0 usec
Fine structure	n^{-3}	-1028 MHz	-92 MHz

interact strongly.

After the pioneering work by Rydberg [2] and others at the end of the last century and the beginning of this century, this branch of spectroscopy was dormant for many decades. This is due to the fact that it is very difficult to create, maintain and detect the Rydberg states by conventional spectroscopy. But due to the availability of stable, highly intense, highly monochromatic and tunable lasers and due to the development of high sensitive techniques and instruments there is a rejuvenation of Rydberg spectroscopy in the past two decades. Much work has already been reported on the Rydberg states of hydrogen, alkali and alkaline earth atoms. The Rydberg states of even the complex rare gas and rare-earth atoms have been studied. The development of this field can be gauged by the review articles by Edelstein and Gallagher [1], Feneuille and Jaquinot [3], Gallas et al. [4], Kleppner [5] and from the book on this field edited by Stebbing and Dunning [6].

V.1.2. Experimental techniques of Rydberg spectroscopy

The experiments typically consist of a 'preparatory stage', where the Rydberg levels are selectively populated, an 'evolution stage', where the prepared stage evolve freely or under external perturbation, and a 'detection stage', where the evolution undergone in the previous stage is observed.

V.1.2.1. Preparation of the Rydberg states

One method of generation of Rydberg state is to impinge high energy ion beam of the atom of interest on solid or gas target.

In this process the ions pick up electrons from the target and they end up in Rydberg states of the atom. However the prepared state selectivity is very difficult to achieve by this method. Another method employed is the collision of monoenergetic beam of electrons on the atom of interest. Here the selectivity of the final state is achieved by controlling the energy of the electron beam. But optical excitation is the most often used method of Rydberg state preparation. Either conventional light sources or lasers are used for this type of preparation. There are several types of optical excitation as given in Fig. V.1. Fig. V.1(a) shows a Rydberg state preparation, from a lower state, by the absorption of a single photon. Since the cross section of absorption for these processes are very small, mostly high intensity pulsed lasers are employed. The selectivity of the prepared state is determined by the linewidth of the laser used. In Fig. V.1(b) the preparation is achieved by two - step excitation. This may even be a multistep excitation. For good selectivity of states the laser used in the last step should have a narrow linewidth. A similar technique is the multistep excitation in a discharge, where the lowest step is excited by the collisions of the atoms with ions and electrons of the discharge. This is shown in Fig. V.1(c). In discharges some metastable levels always have enough population for further excitations to higher levels. Fig. V.1(d) shows stepwise excitation involving spontaneous decay. Finally, as shown in Fig. V.1(e), two-photon and multiphoton excitations can also be employed to reach very high levels. The added advantage of the last method is that the levels that cannot be reached by single

photon absorption because of parity considerations can be reached. In many cases the energy levels of the Rydberg atoms are so near each other that they are merged together by Doppler broadening. Here it becomes necessary to employ some Doppler free technique. In Rydberg spectroscopy the most often used Doppler free techniques are Two - photon absorption spectroscopy [7], Quantum beat spectroscopy [8], Level crossing spectroscopy [9] and Double resonance spectroscopy [10].

V.1.2.2. Detection of Rydberg states

Many types of detection techniques are employed in the Rydberg spectroscopy. This subsection describes few sensitive ones among them.

(a) Detection by field ionization: This is the most sensitive method of detecting Rydberg atoms. Rydberg atoms have low ionization thresholds in d.c. electric fields. In the field ionization technique the electrons which are produced by ionization are accelerated and are counted by channeletron electron multipliers. Depending upon the need, two types of electric fields are applied. One type is the electric pulse and the other is an electric ramp. The ionization threshold depends upon the n , l and m_l values of the Rydberg state. Hence, these states ionize at different times in an electric ramp. In this way selectivity of the levels can be achieved even in the detection. By field ionization method even a single atom in a well defined state can be detected. This method is well suited when the atom of interest is in the form of a beam.

(b) Space charge detection method: This method, also called

thermionic detection is a very sensitive and convenient technique while working with atomic cells. These cells have two electrodes between which a low electric potential is applied. In the absence of Rydberg atoms the current in the cell is space charge limited. If Rydberg atoms are present they may get ionized by collisions and move towards the electrodes. This further ionizes many neutral atoms. This ion current neutralizes the space charge, which is detected as the change in current in the external circuit. Since there is an internal gain of 10^5 to 10^6 , this method of detection is very sensitive. The main disadvantage of this technique as compared to the field ionization method is that, this detection method is not state selective.

(c) Optogalvanic detection method: This method has been covered in detail in Chapter II of this thesis. This is a convenient and suitable detection technique while working with discharge media.

(d) Fluorescence detection method: In this method the fluorescence from the Rydberg levels to a lower level is monitored. Since the fluorescence yield by these transitions is very low this is not a very sensitive method. However under favorable conditions this technique can be employed for detection of medium excited levels (n between 10 and 20).

V.1.3. Theoretical framework for the analysis of Rydberg spectra

In Rydberg spectroscopy physical parameters of Rydberg states like energy, fine structure, lifetime etc. over a long series is studied. It is found that a few parameters like quantum defects are enough to explain these variations. Rydberg states

can be classified into two types, penetrating and non-penetrating. The classification depends upon the angular momentum l of the valence electron and the maximum angular momentum l_0 of the core electrons. It is independent of the n quantum number of the valence electron. All states with $l > l_0$ are non-penetrating and $l < l_0$ are penetrating states. For example states with $l > 1$ for Li, $l > 2$ for Na and K and $l > 3$ for Rb and Cs are non-penetrating states.

V.1.3.1 Non-penetrating states

In these states the overlap between the valence and the core electron wavefunctions are assumed to be negligible. The resulting wavefunctions are the regular Coulombic functions given in Ref [11] as

$$R_{vl} = f(v, l, \rho) / r \quad \text{-----(1)}$$

with $\rho = r/a_0$

a_0 = Bohr radius

and

$$f(v, l, \rho) = \sum_{q=0}^{\infty} (v)^{-2q} \sum_{p=2q}^{3q} a_{q,p} (1) (2\rho)^{1/2(p+1)} J_{(2l+1+p)}(\sqrt{8\rho}) \quad \text{-----(2)}$$

with $a_{qp} = 0$ unless $2q < p < 3q$

$$a_{00} = 1 \quad a_{12} = (1 + 1)/4 \quad a_{13} = 1/12$$

$$\text{and } a_{pq} = 1/4p \{ (2l+p) a_{q-1,p-2} - a_{q-1,p-3} \} \quad \text{-----(3)}$$

$q > 1 \quad p > 3$

where $J_i(x)$ are the Bessel Functions

Following Ref. [12] it can be shown that the term values

$T_{n,l}$ can be given as

$$T_{n,l} = T_{\infty} - R_m / (n - \mu_l) \quad \text{-----(4)}$$

The above is the familiar Rydberg Formula with μ_l the quantum defect; which mainly depends on l and not much on n of the valence electron. T_{∞} is the ionization energy and R_m is the Rydberg constant for that element.

In case of the non-penetrating states the atomic core can be considered as a source of electrostatic potential $V(r)$, which can be expanded in multipolar form as

$$V(r) = -e^2/r + V'(r) \quad \text{-----(5)}$$

$$\text{where } V'(r) \simeq -1/2(\alpha'_d/r^4 - \alpha'_q/r^6) \quad \text{-----(6)}$$

In the above it is assumed that the main contribution is due to the induced dipolar and quadrupolar terms only. Now $V'(r)$ can be treated as a perturbation and it is shown in Ref. [12,13]

$$\mu_l = 3\alpha'_d/4 l^5 + 35\alpha'_q/16 l^9 \quad \text{-----(7)}$$

where α'_d and α'_q are the dipolar and quadrupolar polarizabilities of the core.

V.1.3.2 Penetrating states

The valence electrons in these states strongly interact with the core. Hence a simple treatment as given before for the non - penetrating states will not be valid. For treating penetrating orbitals Hartree [14], Ham [15], and Seaton [16] have developed a theory called Quantum Defect Method (QDM). The assumptions of QDM are,

- (1) The interaction between the valence electron and the core is limited to a small region of radius r_0 around the core.
- (2) For $r > r_0$, the potential is Coulombic and the wavefunction is

Coulombic functions satisfying boundary conditions at $r = r_0$ and $r = \infty$.

(3) The details of the wavefunction at $r = r_0$ is determined by the short range core - valence electron interaction.

With certain assumptions on the regularities of the core wavefunction, it has been shown by Ham [15], that the total wavefunction must be an analytical function of energy in the whole space.

A possible basis of space of analytical Coulomb wavefunction is the set of two functions $f(v, l; g)$ and $g(v, l; g)$ as given in Ref. [17], with the following asymptotic form,

$$f(v, l; g) \simeq (-1)^l v^{1/2} [\Gamma(v-l) \Gamma(v+l+1)]^{1/2} * \\ [(1/\pi)(2r/v)^{-v} e^{-r/v} \sin \pi v - (2r/v)^v e^{-r/v} e^{i\pi v}] \quad \text{---(8)}$$

and

$$g(v, l; g) \simeq (-1)^l v^{1/2} [\Gamma(v-l) \Gamma(v+l+1)]^{1/2} * \\ [-(1/\pi)(2r/v)^{-v} e^{r/v} \cos \pi v + (2r/v)^v e^{-r/v} e^{i\pi(v+1/2)}] \quad \text{-----(9)}$$

with the following properties for f and g ,

- (1) f is regular at $r = 0$ and g is irregular there.
- (2) When $r \rightarrow \infty$, g is in quadrature with f .
- (3) Both f and g correspond to the same energy

$$E = -R_m/v^2 \quad \text{-----(10)}$$

Since we are interested only in the single electron atoms like alkali atoms, the core wavefunction ϕ can be assumed not to depend upon the properties of the outer electron. The total wavefunction of the system can be given as,

$$\Psi = \varphi R_{v1}^{QDM}(r) \quad \text{-----(11)}$$

where $R_{v1}^{QDM}(r)$ is the outer electron wavefunction, which is given as the linear combination of f and g as,

$$R_{v1}^{QDM}(r) = \cos \pi \mu f(v, l; \varphi) - \sin \pi \mu g(v, l; \varphi) \quad \text{for } r > r_0 \quad \text{--(12)}$$

So the problem reduces to finding the coefficients $\cos \pi \mu$ and $\sin \pi \mu$, which in turn are determined by the boundary conditions at $r = \infty$. Besides the radial boundary condition $R_{v1}^{QDM}(r) \rightarrow 0$ as $r \rightarrow \infty$ gives the energy quantization condition as,

$$\sin \pi (v + \mu_1) = 0 \quad \text{-----(13)}$$

The above condition imply $v + \mu_1 = n$ an integer or alternatively

$$v = n - \mu_1 \quad \text{-----(14)}$$

from above it can be shown that the term values of the levels are given as,

$$T_{n1} = T_{\infty} - R/(n - \mu_1) \quad \text{-----(15)}$$

which is once again the Rydberg Formula for the energy of a level in a series. Here μ_1 , the quantum defect, which was introduced as a phenomenological constant by Rydberg has now a physical meaning. The parameter v in the equation is called the effective quantum number.

Most of the properties of the Rydberg atoms depend upon the nature of the wavefunction when $r \gg r_0$. Hence the asymptotic solutions of $R_{v1}^{QDM}(r)$ can be used to calculate them. To give examples,

(1) The oscillator strengths f involving the Rydberg states $|v, l\rangle$ and $|v' l'\rangle$ can be given as,

$$f = |R(vl, v'l')|^2 = \int r R_{v1}^{QDM}(r) R_{v'1}^{QDM}(r) \quad \text{-----(16)}$$

where $R(vl, v'l')$ is the dipole matrix element.

(2) In a similar way the lifetime τ of a level $|v, l\rangle$ can be given

as

$$\frac{1}{\tau} = \frac{4}{3} \alpha \max(l, l') \frac{(E_{v'l} - E_{v'l'})^3 (R(vl, v'l'))^2}{(2l+1) h^3 c^2} \quad \text{-----}(17)$$

where α is the fine structure constant and $|v', l' \rangle$ are the allowed levels to which $|v, l \rangle$ can decay.

From above we see that the calculation of many Rydberg state properties depend upon the calculation of the radial matrix element $R(vl, v'l)$. Bebb [18] and Gounand [19] have assumed the initial bound state Coulomb wavefunctions as

$$R_{vl}^{QDM}(r) = N e^{-r/v} \sum_{t=0}^{\infty} a_t r^{(v-t)} \quad \text{-----}(19)$$

where

$$N = (-1)^{(n-l-1)} (2/v)^v [\rho(v) v^2 \Gamma(v-1) \Gamma(v-1+1)] \quad \text{-----}(20)$$

with, $\rho(v)$ differing from unity only if quantum defect differs significantly with n and the coefficients a_t are given as recursion relations as

$$a_0 = 1 \quad \text{and} \quad a_t = a_{t-1} (v/2t) [1(l+1) - (v-t)(v-t-1)] \quad \text{---}(21)$$

Then the radial matrix elements were derived as,

$$R(vl, v'l') = NN' \left\{ \sum_{p=0}^{P_{\min}-1} F(p) + 1/2[F(P_{\min}) + F(P_{\min} + 1)] \right\} \quad \text{-----}(22)$$

where

$$F(p) = A_p (1/v + 1/v')^{-(a-p+1)} (a-p+1) \quad \text{-----}(23)$$

with

$$a = v + v' + 1 \quad \text{and} \quad A_p = \sum_t a_t (a_{p-t}),$$

The value of the $R(vl, v'l')$ depends critically on the termination criteria of the series.

V.1.4. Rydberg spectroscopy of cesium

Alkali atoms have been the work-horses of Rydberg spectroscopy due to the ease with which the experiments can be conducted and due to their simple atomic structure. Much work has already been reported on the Rydberg levels of alkali atoms [20].

Cesium is the heaviest stable alkali atom with $Z = 55$ and $[\text{Xe}]6s^2S_{1/2}$ ground state configuration. Much work has been done by optical spectroscopy and many of the Cs levels are well tabulated [21-22]. By now the term values of $^2S_{1/2}$ states up to $n=35$ [23-26], $^2P_{1/2,3/2}$ states up to $n = 83$ [23,25,27-29], $^2D_{3/2,5/2}$ states up to $n = 58$ [23-28], $^2F_{5/2,7/2}$ states up to $n = 109$ [23,25,28-32], and $^2G_{7/2,9/2}$ for $n = 15-17$ and $27-36$ [28,31-32] have been reported.

Some authors [23,26] have least square fitted the measured values of the term energies into an extended Rydberg-Ritz formulae of the type

$$\mu_n = n - n^* \\ = a' + b't_n + c't_n^2 + d't_n^3 + e't_n^4 \quad \text{-----(24)}$$

From the fits fitting coefficients are extracted. The calculated quantum defect is used to obtain the series limit or the ionization limit, T_∞ . By this procedure Lorenzen et al. [26] have reported the ionization limit of cesium as $31406.468 + 0.006 \text{ cm}^{-1}$. Sansonetti et al. [29] have used the fitted values for the effective quantum number n^* to calculate the fine structure constants, by an expression as given by Pendrill [35],

$$\Delta_{fs} = A/(n^*)^3 + B/(n^*)^4 + C/(n^*)^5 + D/(n^*)^7 \quad \text{-----(25)}$$

They have also compared the calculated Δ_{fs} values with their highly accurate 2P_J and 2F_J series fine structure data. Lorenzen

et al. [33] have reported a surprisingly non-monotonic variation of Cs n^2D_J series' quantum defects. Fredrickson et al. [35] have observed that the 2F_J series of Cs is inverted. But it is very surprising that very few people have reported the oscillator strengths of the transitions of the Rydberg states in Cs. For lower level transitions f values have been reported by Marr and Creak [36]. Popsecu et al. [24] were the only one to report the f values of transitions of the principal series of Cs from their experiment.

This thesis reports the results of the optogalvanic experiments conducted on a Cesium/Neon discharge. These experiments were performed to measure the term values of the different Rydberg series. The main series identified were the $5d^2D_{3/2} \rightarrow nf^2F_{5/2}$, $5d^2D_{5/2} \rightarrow nf^2F_{5/2,7/2}$, $5d^2D_{5/2} \rightarrow np^2P_{3/2}$ and $5d^2D_{3/2} \rightarrow np^2P_{1/2,3/2}$. All these had their series limit within the range of the dye used.

V.2. EXPERIMENTAL

V.2.1. Experimental Arrangement

Optogalvanic experiments were conducted to measure the term values of $n^2F_{5/2,7/2}$ and $n^2P_{1/2,3/2}$ Rydberg levels of Cesium. The arrangement used was similar to that employed by Bridges [25] but with some differences. We used a cesium/neon discharge while Bridges used a pure cesium discharge. In this way we could use the neon lines as the calibration lines and measure the Rydberg transitions of cesium to a greater accuracy.

Fig. V.2 gives the partial energy diagram of the relevant

cesium energy levels. The 6p and 5d levels get populated by electron and ion collisions with the neutral cesium atoms. Laser light right wavelength excites the atoms from these levels to higher Rydberg levels. The absorption of the laser light is detected by the change in the impedance of the discharge. Since the theory of the Optogalvanic effect has already been discussed in Chapter II, only the experimental details will be briefed here.

The experimental setup employed is give in Fig. V.3, which is very similar to the one described in Chapter II. The main difference was the use of a constructed Cesium/Neon glow discharge lamp. The details of construction of this lamp are given in the next subsection.

V.2.2. Construction of the glow discharge lamp

The schematic of the glow discharge cell used is given in Fig. V.4. The cell was made of pyrex glass with nickel electrodes at both ends of a capillary of 70 mm length and 5.0 mm internal diameter. Nickel was selected as the cathode material after many trails with other material like copper, tungsten and stainless steel. Pyrex windows of 25 mm diameter were fused at both ends of the cell. The ring shaped electrodes were held by glass sealed tungsten pins, which were taken out of the cell through high vacuum uran seals. This unit was annealed at 600 °C for 24 hours in a furnace. The cell was evacuated to $< 10^{-5}$ Torr pressure and then filled with high purity Cesium (99.999%) in the following way.

The schematic of the filling station is given in Fig. V.5.

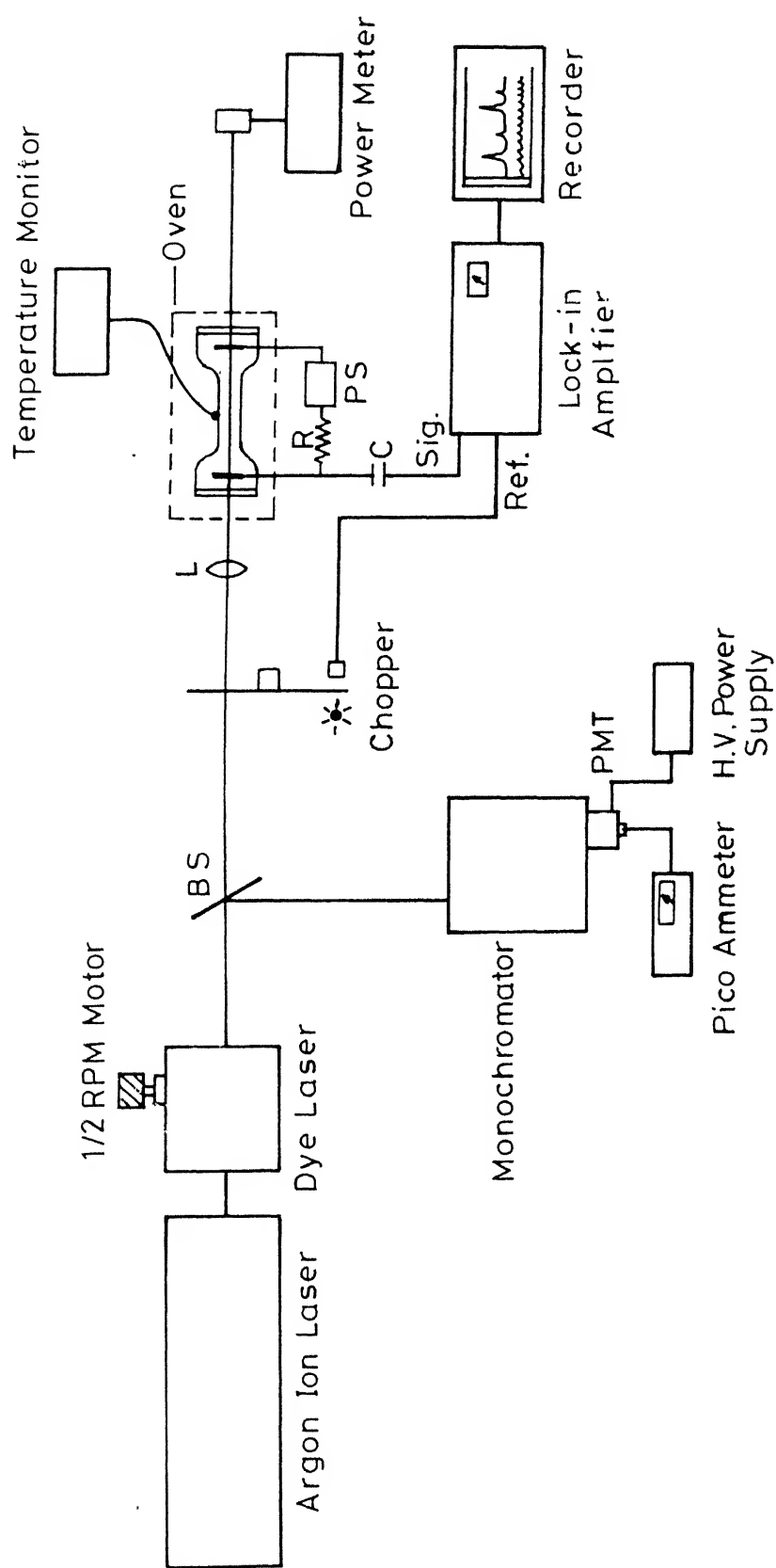


Fig.V.3 Experimental setup for cesium optical spectroscopy.

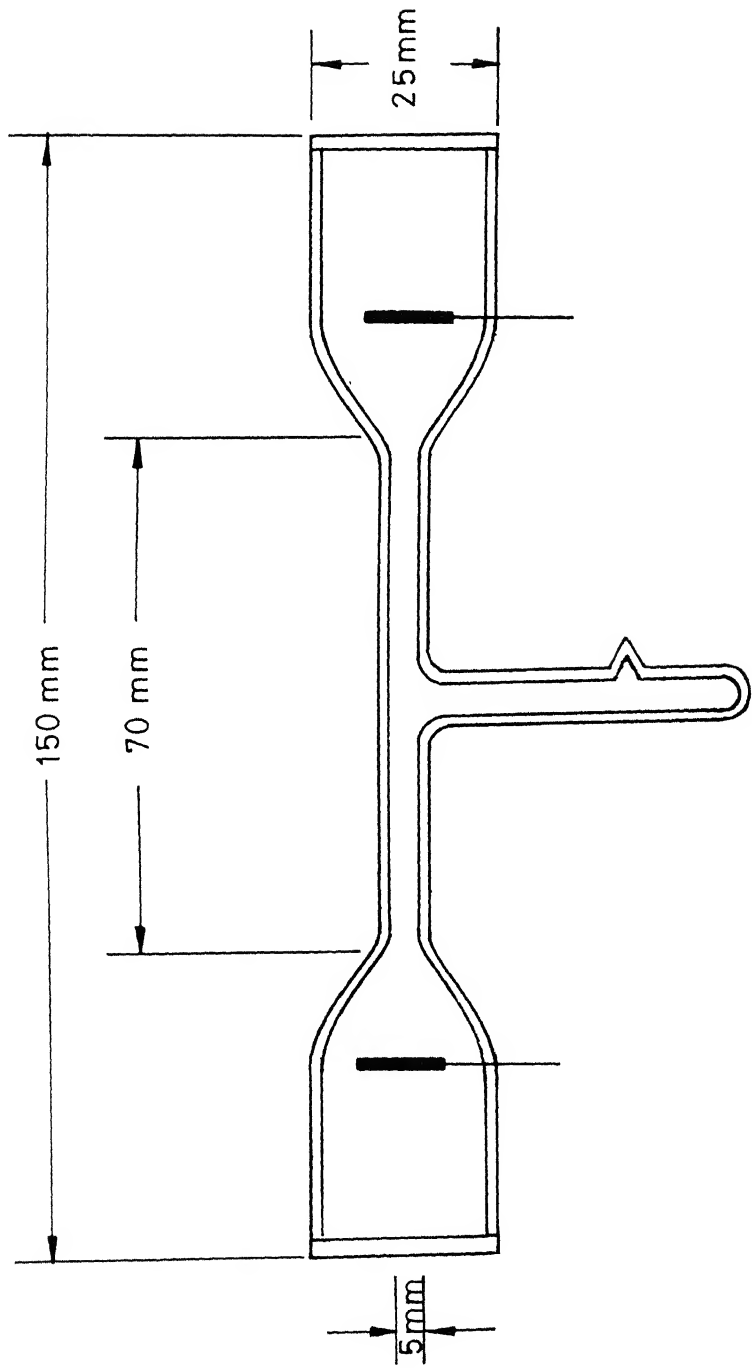


Fig.V.4 Cesium discharge cell .

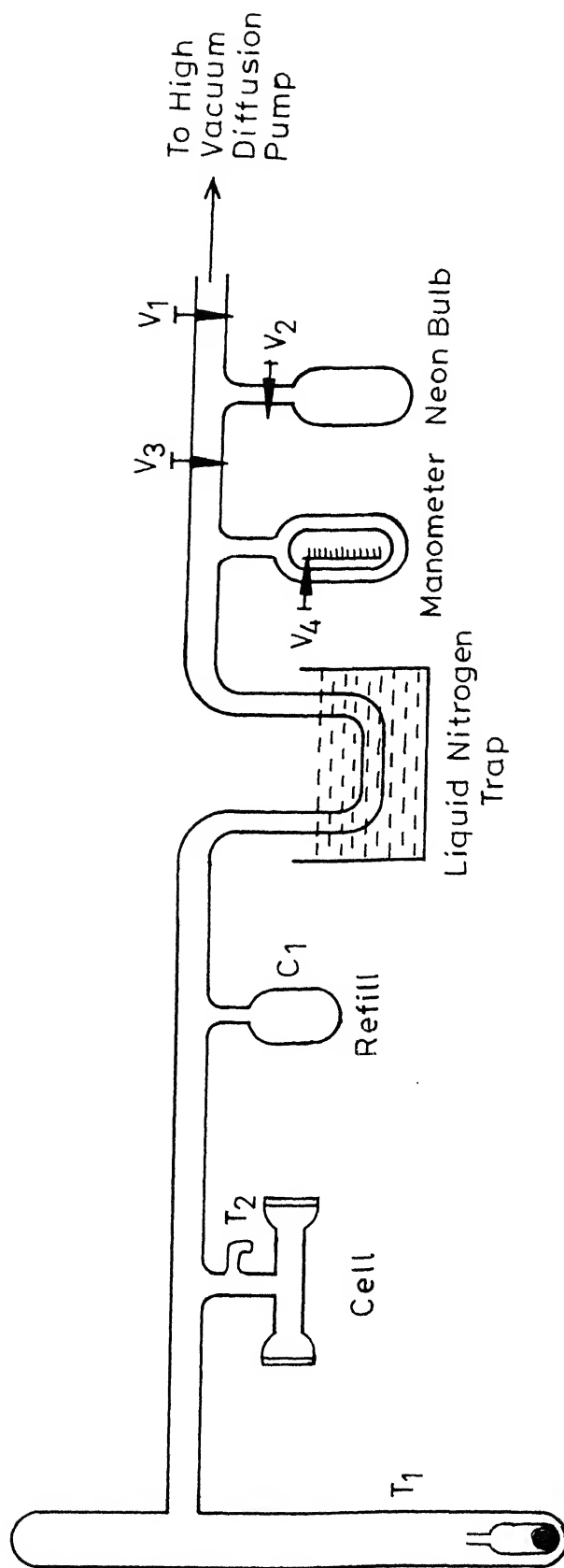


Fig.V.5 Schematic of cesium filling station.

Since Cesium reacts with atmospheric moisture it can not be kept exposed to air. Cesium was available in the form of ampules, under argon atmosphere. The ampule was chilled in liquid nitrogen for 15 mts. and then the seal was broken. The reaction rates are slow at this temperature and the broken ampule can be kept exposed to atmosphere without much oxidation for roughly eight minutes. This was then dropped into the sidearm T_1 and the top of the sidearm was then sealed. Then the whole system was evacuated to $< 10^{-5}$ Torr. The system was also degassed many times. Then using a hand torch flame the sidearm T_1 was heated and the cesium was evaporated and driven into the sidearm T_2 of the cell. This sidearm was kept at liquid nitrogen temperature during this process. The excess cesium was filled into the refill cell C_1 and sealed off for future use. Then the cell was filled with 2 Torr of neon. This pressure was measured with a U-tube manometer.

Neon in the cell acts as a buffer gas and prevents the cell windows being coated with cesium during operation. Neon also helps in the easy and low voltage striking of the discharge in the cell. Besides as mentioned earlier the neon OG lines present themselves as good calibration lines for the Rydberg spectra.

While the cell was still fixed to the filling station, the discharge was struck and maintained for many hours. Then the direction of the discharge was reversed and the same operation was repeated. This process cleans the electrodes. After that the cell was pinched off from the filling station.

V.2.3. Experimental Procedure

During the experiments the cell was heated to 190°C by

heating tapes wrapped around the cell. Asbestos tapes were wrapped around this to prevent temperature instabilities due to radiation and convection losses. The temperature of the cell was monitored by a chromel - alumel thermocouple. The windows of the cell were kept roughly 10°C above the rest of the cell to prevent them from getting coated with cesium metal. The cell needed at least half an hour temperature stabilization before the experiments, to minimize the temperature caused instabilities in the discharge. This glow discharge cell was operated at 6 mA current during the experiments. This figure was arrived at after repeated trials for stable, low noise discharge which maximizes the signal strength. The dye laser was scanned through whole of the R6G dye range by the 1/2 RPM motor and signals recorded. It was found during the experiments that the discharge plasma oscillates and the signals were noisy for some current and temperature values. These combinations were avoided during the final runs. Many scans were taken for repeatable, low noise spectra with good dispersion.

V.3. RESULTS AND DISCUSSION

Observation of many runs showed that there are 102 lines in the range of the dye laser used. The whole spectrum is presented in Fig. V.6. As a first step the neon lines in the spectrum were identified with the help of a monochromator during the experiment and then by comparing the final spectrum with that of Zalewski [37]. These neon lines which were used as calibration lines are presented in Table V.2. Accurate values of these neon lines were

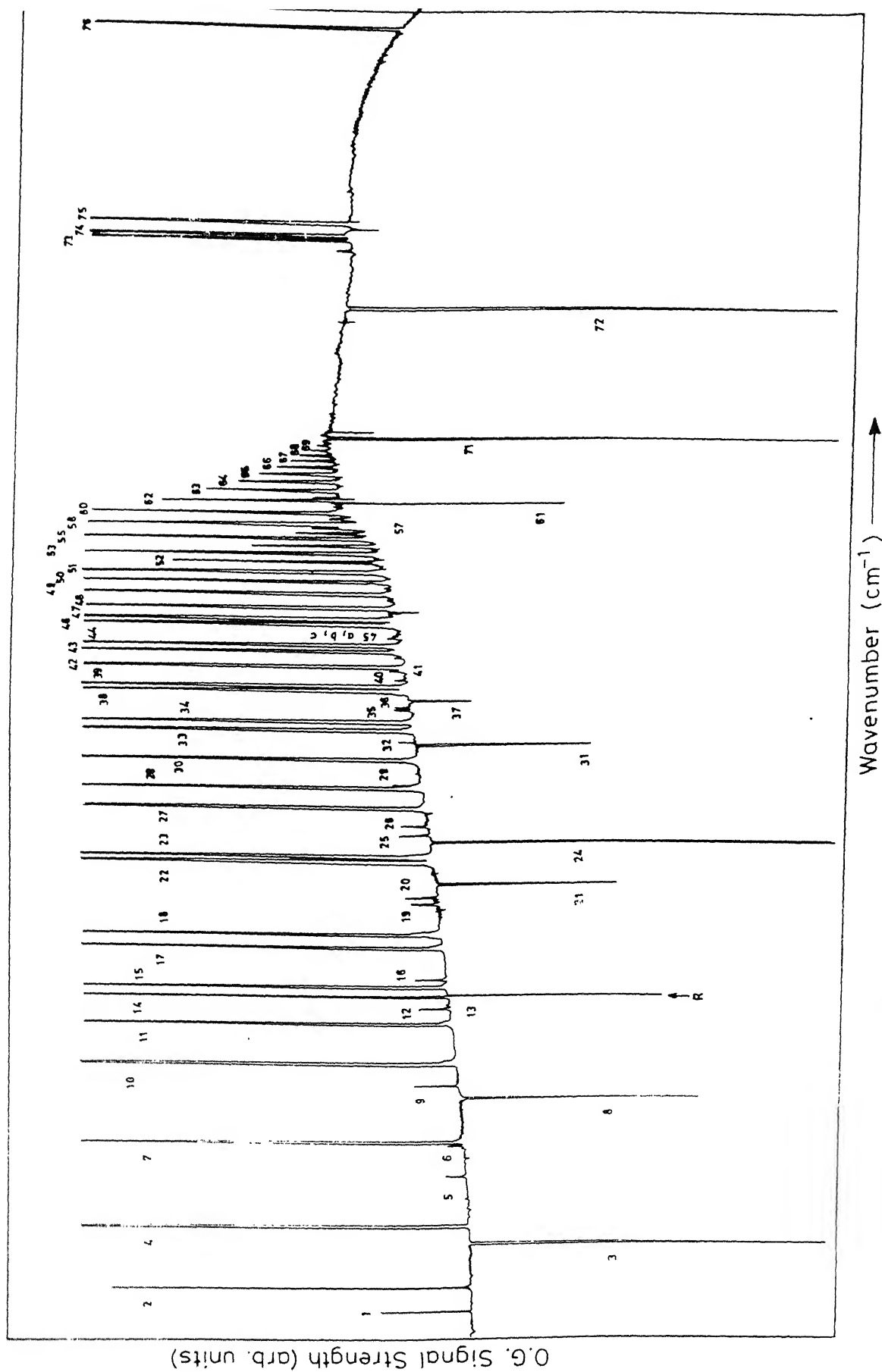


Fig. I.6 Optogalvanic spectrum of Cs/Ne discharge.

TABLE V.2

Neon calibration lines

S.No.	Peak No.	Wavelength ^[38] (nm)	Wave number ^[38] (cm ⁻¹)	Transition ^[22]
1	3	633.4426	15782.386	3s[3/2] ₂ -3p[5/2] ₂
2	8	626.6494	15953.473	3s'[1/2] ₀ -3p'[3/2] ₁
3	21	616.3593	16219.813	3s'[1/2] ₀ -3p'[1/2] ₁
4	24	614.3062	16274.023	3s[3/2] ₂ -3p[3/2] ₂
5	31	609.6163	16399.223	3s[3/2] ₁ -3p'[3/2] ₂
6	37	607.4337	16458.147	3s[3/2] ₁ -3p[1/2] ₀
7	N	602.9996	16579.167	3s'[3/2] ₁ -3p'[1/2] ₁
8	61	597.5534	16730.272	3s[3/2] ₂ -3p'[3/2] ₁
9	71	594.4834	16816.669	3s[3/2] ₂ -3p'[3/2] ₂
10	72	588.1894	16996.615	3s[3/2] ₂ -3p'[1/2] ₁
11	73(a)	585.2523	17082.017	3s'[1/2] ₁ -3p'[1/2] ₀

taken from Ref.[38]. The average dispersion of the spectra in the different charts was around $3.89 \text{ cm}^{-1}/\text{mm}$. A small random non-linearity of the order of $0.3 \text{ cm}^{-1}/\text{mm}$ was observed in the calculated dispersion within the same scan. This was attributed to non uniform scanning of the dye laser and the recorder. The overall accuracy of the measurement was about $\pm 0.5 \text{ cm}^{-1}$.

Table V.3 presents the measured wavenumbers of all the lines in the spectrum. The table also presents the visually estimated peak heights of these OG lines. Normalization with respect to laser power was not performed. It was found that many of the lines were saturated.

With the help of the Moors' Table [21] $5d^2D_{5/2} \rightarrow np^2P_{3/2}$ series and the $5d^2D_{3/2} \rightarrow np^2P_{1/2,3/2}$ series were identified. For identification of these series the energy of the $5d^2D_{3/2}$ and $5d^2D_{5/2}$ states were taken as 14499.49 cm^{-1} and 14597.08 cm^{-1} respectively. The former series was identified from $n = 16$ to $n = 24$ and the later could be observed from $n = 14$ to $n = 21$. Then making use of the Rydberg formula for cesium

$$T_{nl} = T_{\infty} - R_{Cs}/n^* \quad \text{-----}(24)$$

with

$$n^* = n - \delta \quad \text{-----}(25)$$

The effective quantum number n^* and the quantum defect δ were calculated for each of these levels. The Rydberg constant for cesium R_{Cs} was taken as $109736.86 \text{ cm}^{-1}$ and the ionization limit T_{∞} as 31406.47 cm^{-1} [26]. These results are presented in Table V.4.

In a similar way, with the help of data in references [21-22,30-31] two more series, $5d^2D_{3/2} \rightarrow nf^2F_{5/2}$ and $5d^2D_{5/2} \rightarrow$

Table V.3
Transitions classification chart

S. No.	Peak No.	Measured Wavenumber (cm ⁻¹)	Element	Transition	Signal Strength
1	1			--	22
2	2	15704.70	Cs	5d ² D[5/2]-10f ² F[5/2,7/2]	89
3	3	15782.386	Ne	3s[3/2] ₂ -3p[5/2] ₂	-87
4	4	15802.42	Cs	5d ² D[3/2]-10f ² F[5/2]	S
5	5	15863.15		--	5
6	6	15898.48	{ Cs { { Cs	{ 5d ² D[3/2]-11f ² F[5/2,7/2] } { { 5d ² D[3/2]-14p ² P[1/2,3/2] }	4
7	7	16092.68		--	S
8	8	15953.473	Ne	3s'[3/2] ₀ -3p'[3/2] ₁	-59
9	9	15973.20		--	10
10	10	15998.996	Cs	5d ² D[3/2]-11f ² F[5/2]	S
11	11	16047.97	Cs	5d ² D[5/2]-12f ² F[5/2,7/2]	S
12	11(a)	16049.73		--	3
13	12	16067.84	Cs	5d ² D[3/2]-15p ² P[1/2,3/2]	7
14	13	16072.72		--	<1
15	14	16083.18	Cs	6p ² P[3/2]-8d ² D[3/2]	S
16	15	16093.74	Cs	6p ² P[3/2]-8d ² D[5/2]	S
17	16	16102.55	Cs	5d ² D[5/2]-16p ² P[3/2]	8
18	17	16141.02	Cs	5d ² D[3/2]-12f ² F[5/2]	S
19	17(a)	16141.05		--	3
20	18	16157.25	Cs	5d ² D[5/2]-13f ² F[5/2,7/2]	S

Resolution?

133

S. No.	Peak No.	Measured Wavenumber (cm ⁻¹)	Element	Transition	Signal Strength
21	18(a)				
22	71	16188.29		--	8
23	19	16193.74		--	7
24	20	16202.73		--	<<1
25	21	16219.813	Cs	5d ² D[5/2]-17p ² P[5/2]	8
26	72	16222.14	Ne	3s'[1/2] ₀ -3p'[1/2] ₁	-44
27	73	16226.78		--	<<1
28	74	16231.88		--	<<1
29	75	16234.20		--	<<1
30	22	16247.68		--	<<1
31	23	16254.74	Cs	5d ² D[5/2]-14f ² F[5/2,7/2]	S
32	24	16274.023	Cs	5d ² D[3/2]-13f ² F[5/2]	S
33	25	16282.69	Ne	3s[3/2] ₂ -3p[3/2] ₂	S
34	26	16295.23	Cs	5d ² D[5/2]-18p ² P[3/2]	8
35	26(a)	16298.56	Cs	5d ² [3/2]-17p ² P[1/2,3/2]	7
36	76	16310.70		--	<1
37	27	16317.39		--	<<-1
38	28	16344.54	Cs	5d ² D[5/2]-15f ² F[5/2,7/2]	S
39	29	16348.38	Cs	5d ² D[3/2]-14f ² F[5/2]	S
40	30	16380.49	Cs	5d ² D[5/2]-19p ² P[3/2]	6
41	31	16399.223	{ Cs	5d ² D[5/2]-16f ² F[5/2,7/2] }	S
			{ Cs	5d ² D[3/2]-18p ² P[1/2,3/2] }	
42	32	16404.23	Ne	3s[3/2] ₁ -3p'[3/2] ₂	-42
			Cs	5d ² D[5/2]-20p ² P[3/2]	5

S. No.	Peak No.	Measured Wavenumber (cm ⁻¹)	Element	Transition	Signal Strength
43	33	16418.96	Cs	5d ² D[3/2]-15f ² F[5/2]	S
44	34	16429.53	Cs	5d ² D[5/2]-17f ² F[5/2,7/2]	S
45	35	16445.26		--	4
46	36	16448.96	{ Cs { { Cs	5d ² D[5/2]-21p ² P[3/2] 5d ² D[3/2]-19p ² P[1/2,3/2]	{ } }
47	37	16458.147	Ne	3s[3/2] ₁ -3p[1/2] ₀	-14
48	38	16470.22	Cs	5d ² D[5/2]-18f ² F[5/2,7/2]	S
49	39	16477.54	Cs	5d ² D[3/2]-16f ² F[5/2]	S
50	40	16487.34	Cs	5d ² D[5/2]-22p ² P[3/2]	3
51	41	16499.86	Cs	5d ² D[3/2]-20p ² P[1/2,3/2]	
52	42	16504.46	Cs	5d ² D[5/2]-19f ² F[5/2,7/2]	S
53	*1	16517.51	Cs	5d ² D[5/2]-23p ² P[3/2]	2
54	43	16525.892	Cs	5d ² D[3/2]-17f ² F[5/2]	S
55	44	16533.80	Cs	5d ² D[5/2]-20f ² F[5/2,7/2]	S
56	45(a)	16545.37	Cs	5d ² D[5/2]-24p ² P[3/2]	2
57	45(b)	16548.04	Cs	5d ² D[3/2]-21p ² P[1/2,3/2]	1
58	45(c)	16511.234		--	<1
59	46	16561.95	Cs	5d ² D[5/2]-21f ² F[5/2,7/2]	S
60	47	16569.67	Cs	5d ² D[3/2]-18f ² F[5/2]	S
61	N	16579.167	Ne	3s'[3/2] ₁ -3p'[3/2] ₁	-6
62	48	16584.55	Cs	5d ² D[5/2]-22f ² F[5/2,7/2]	S
63	*2	16594.19		--	<1
64	*3	16596.72		--	<1

cont'd..

S. No.	Peak No.	Measured Wavenumber (cm ⁻¹)	Element	Transition	Signal Strength
65	49	{ 16603.25 { { 16603.68	Cs Cs	5d ² D[3/2]-19f ² F[5/2] 5d ² D[5/2]-23f ² F[3/2,7/2]	S
66	*4	16613.57		--	<1
67	50	16619.87	Cs	5d ² D[5/2]-24f ² F[5/2,7/2]	74
68	51	16634.26	{ Cs { { Cs	5d ² D[3/2]-20f ² F[5/2] 5d ² D[5/2]-25f ² F[3/2,7/2]	S
69	*5	16643.04		--	1
70	52	16648.85	Cs	5d ² D[5/2]-26f ² F[5/2,7/2]	51
71	?7	16653.29		--	<1
72	53	{ 16657.43 { { 16658.83	Cs Cs	5d ² D[5/2]-21f ² F[5/2] 5d ² D[5/2]-27f ² F[5/2,7/2]	S
73	*6	16665.89		--	1
74	54	16669.73	Cs	5d ² D[5/2]-28f ² F[5/2,7/2]	30
75	55	{ 16679.54 { { 16679.91	Cs Cs	5d ² D[3/2]-22f ² F[5/2] 5d ² D[5/2]-29f ² F[5/2,7/2]	S
76	56	16687.20	Cs	5d ² D[5/2]-30f ² F[5/2,7/2]	16
77	57	16694.33	Cs	5d ² D[5/2]-31f ² F[5/2,7/2]	12
78	58	16697.55	Cs	5d ² D[3/2]-23f ² F[5/2]	66
79	*7	16701.95	Cs	5d ² D[5/2]-32f ² F[5/2,7/2]	10
80	59	16707.43	Cs	5d ² D[5/2]-33f ² F[5/2,7/2]	5.5
81	60	16714.27	{ Cs { { Cs	5d ² D[3/2]-24f ² F[5/2] 5d ² D[5/2]-34f ² F[5/2,7/2]	62
82	*8	16717.35	Cs	5d ² D[5/2]-35f ² F[5/2,7/2]	2

cont'd..

S. No.	Peak No.	Measured Wavenumber (cm^{-1})	Element	Transition	Signal Strength
83	*9	16723.27	Cs	$5d^2D[5/2]-36f^2F[5/2,7/2]$	1
84	61	16730.272	Ne	$3s[3/2]_2-3p'[3/2]_1$	-54
85	62	16731.49	Cs	$5d^2D[3/2]-25f^2F[5/2]$	44
86	63	16743.82	Cs	$5d^2D[3/2]-26f^2F[5/2]$	33
87	64	16755.93	Cs	$5d^2D[3/2]-27f^2F[5/2]$	25
88	65	16766.00	Cs	$5d^2D[3/2]-28f^2F[5/2]$	19
89	66	16775.76	Cs	$5d^2D[3/2]-29f^2F[5/2]$	15
90	67	16793.39	Cs	$5d^2D[3/2]-30f^2F[5/2]$	11
91	68	16793.39	Cs	$5d^2D[3/2]-31f^2F[5/2]$	7
92	69	16800.12	Cs	$5d^2D[3/2]-32f^2F[5/2]$	5
93	70	16806.08	Cs	$5d^2D[3/2]-33f^2F[5/2]$	3
94	70(a)	16811.86	Cs	$5d^2D[3/2]-34f^2F[5/2]$	1
95	71	16816.669	Ne	$3s[3/2]_2-3p'[3/2]_2$	-S
96	72	16996.615	Ne	$3s[3/2]_2-3p'[1/2]_1$	-S
97	73(a)	17082.017	Ne	$3s'[1/2]_1-3p'[1/2]_0$	-4
98	73	17096.19	Cs	$6p^2P[3/2]-9d^2D[3/2]$	S
99	74	17102.58	Cs	$6p^2P[3/2]-9d^2D[5/2]$	S
100	75	17119.38	Cs	$6p^2P[1/2]-10s^2S[1/2]$	S
101	76	17391.30	Cs	$6p^2P[3/2]-11s^2S[1/2]$	S
102	*0	16198.82	Cs	$5d^2D[3/2]-16p^2P[1/2,3/2]$	<1

S Saturated lines

TABLE V.4

Wavenumbers (cm^{-1}), Effective Quantum numbers (N^*), And
Quantum Defects (δ) Of n^2P_j Levels

S.No.	--> n^2P_j	Average Wavenumber (cm^{-1}) $5^2D_{5/2} \rightarrow n^2P_{3/2}$	n^*	δ
1	14p	30397.97	10.438	3.569
2	15p	30567.33	11.436	3.564
3	16p	30698.97	12.454	3.546
4	17p	30797.27	13.421	3.579
5	18p	30879.84	14.435	3.565
6	19p	30946.96	15.454	3.546
7	20p	31000.41	16.439	3.561
8	21p	31046.96	17.472	3.528
9	22p	31084.42	18.460	3.540
10	23p	31114.59	19.389	3.610
11	24p	31142.45	20.387	3.613

$nf^2F_{5/2,7/2}$ were identified. Once again the effective quantum numbers and the quantum defects of each of these Rydberg levels were calculated and presented in Table V.5. The first series could be traced from $n = 10$ to $n = 34$ and the second series from $n = 10$ to $n = 36$. As can be seen from Fig. V.6, all these series have their series limit well within the dye laser range. Fig. V.7 shows part of the two 2F_J series with their upper level reached.

Besides the above, some transitions from $6p^2P_{1/2,3/2}$ to $ns^2S_{1/2}$ and $nd^2D_{3/2,5/2}$ states were also observed. All those identified transitions are reported in Table V.3. There are 23 lines which could not be assigned to CsI, CsII, Rb, Ni, W or Cs two photon transitions. These lines are also identified in Table V.3.

As discussed in detail in the beginning of this chapter, the quantum defect is a slowly varying function of the angular momentum l . Rydberg electrons with high angular momenta never penetrates the core whereas the Rydberg electrons with angular momentum $l \leq l_{\text{core}}$ penetrates the core and introduces a perturbation which causes a precession of the elliptical orbits in the classical sense. Quantum mechanically, it introduces a phase shift in the radial wave function. The measured quantum defects would be valuable to obtain information on these phase shifts ie the quantum defect is a direct measure of the phase introduced by the core potential.

In general, any central force of short range perturbation ie perturbation of the form r^{-n} where $n > 2$ gives rise to shifts in the energy levels which can be expressed in terms of quantum defects.

Table V.5

Wavenumbers(cm^{-1}), Effective Quantum numbers(n^*), and Quantum Defects(δ) of n^2F_J series of Cesium

S.No.	Upper level reached --> nf	Average wavenumber (cm^{-1}) $5d^2D_{3/2}-nf^2F_{5/2,7/2}$	n^*	(δ)
1.	10f	30301.83	9.967	0.033
2.	11f	30494.18	10.968	0.032
3.	12f	30640.51	11.969	0.031
4.	13f	30754.28	12.971	0.029
5.	14f	30844.40	13.973	0.027
6.	15f	30916.42	14.964	0.036
7.	16f	30977.33	15.911	0.009
8.	17f	31026.61	16.997	0.003
9.	18f	31067.30	17.874	0.126
10.	19f	31102.14	18.989	0.011
11.	20f	31130.88	19.955	0.045
12.	21f	31157.43	20.992	0.008
13.	22f	31179.06	21.967	0.033
14.	23f	31198.90	22.993	0.007
15.	24f	31215.36	23.963	0.037
16.	25f	31230.96	25.004	(-0.004)
17.	26f	31243.31	25.993	0.007
18.	27f	31255.67	26.976	0.024
19.	28f	31266.15	27.965	0.035
20.	29f	31275.25	28.919	0.081
21.	30f	31284.50	29.995	0.005
22.	31f	31292.15	30.982	0.018
23.	32f	31299.03	31.958	0.042
24.	33f	31305.00	32.887	0.114
25.	34f	31311.35	33.966	0.034

In this picture, polarization of the core by the Rydberg electron, fine and hyperfine interactions and other short range perturbations such as Lamb shift can also be described by quantum defect formalism.

The quantum defects are valuable to obtain the wavefunctions of the electrons of the Rydberg atoms which in turn are helpful to calculate a number of quantities such as oscillator strengths, Rydberg atom lifetimes, collision cross section etc.

V.4. CONCLUSIONS

Employing the optogalvanic detection technique in cesium discharge the following Rydberg series have been measured

$$5d^2D_{3/2} \rightarrow np^2P_{1/2,3/2} \text{ for } n = 14 \text{ to } 21$$

$$5d^2D_{5/2} \rightarrow np^2P_{3/2} \text{ for } n = 16 \text{ to } 24$$

$$5d^2D_{3/2} \rightarrow nf^2F_{5/2} \text{ for } n = 10 \text{ to } 34$$

$$5d^2D_{5/2} \rightarrow nf^2F_{5/2,7/2} \text{ for } n = 10 \text{ to } 36$$

From the spectra term values, effective quantum numbers and quantum defects have been calculated for $np^2P_{1/2,3/2}$ levels for $n=14$ to 24 and for $nf^2F_{5/2,7/2}$ levels for $n=10$ to 34. The values of the quantum defects reported here would be valuable to obtain the phase shifts in the radial wave functions of the electrons in the Rydberg states which in turn could be used to calculate oscillator strengths, Rydberg atom lifetimes, Rydberg atom collision cross section etc.

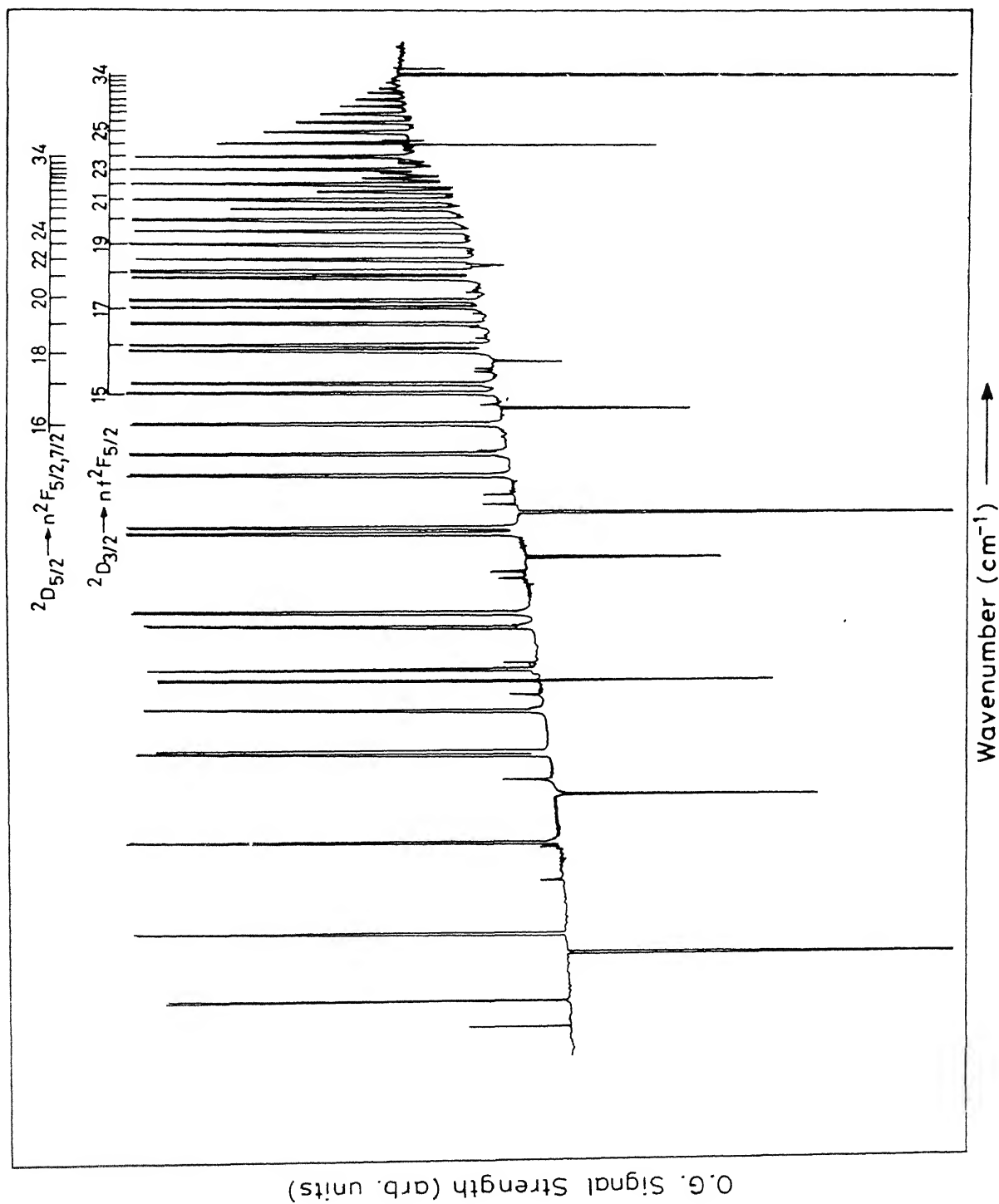


Fig.V.7 $5d^2D_{5/2} \rightarrow n^2F_{5/2,7/2}$ and $5d^2D_{3/2} \rightarrow n^2F_{5/2}$ series of cesium.

REFERENCES

- [1] Edelstein, S.A., and Gallagher, T.F., Adv. Atm. and Mol. Phys., **17**, 365, (1978)
- [2] Rydberg, J.R., Z. Physik Chem. (Leipzig), **5**, 227, (1890)
- [3] Feneuille, S., and Jaqcicot, P., Adv. Atm. and Mol. Phys., **17**, 99, (1981)
- [4] Gallas, J.A.C., Leuchs, G., Walther, H., and Figger, H., Adv. Atm. and Mol. Phys., **20**, 414, (1985)
- [5] Kleppner, D., "Atoms in unusual situations", J.P.Briand (ed.), Plenum Press, to be published (1987), Lecture notes on International Workshop on Modern Optics, Lasers and Laser Spectroscopy, I.I.T., Kanpur, Jan 19 - 29, 1987
- [6] Stebbings, R.F., and Dunning, F.B. eds., 'Rydberg states of atom and molecules', Cambridge Univ. Press, Cambridge (1983)
- [7] Sansonetti, C.J., Lorenzen, C.J., Phys.Rev.A **30**, 1805 (1984)
- [8] Haroche, S., 'High Resolution Spectroscopy', ed. Shimoda, K., Topics in Applied Physics, **13**, 253 (Springer Verlag, Berlin 1976)
- [9] Demtroder, W., 'Lasers Spectroscopy - Basic concepts and Instrumentation', Second corrected printing, Spri. Ser. in Chem. Phys. **5**, Spri. Verlag, Berlin, 1982
- [10] Cooke, W.E., Gallaghev, T.f., Edelstein, S.A., and Hill, R.M., Phys.Rev. **16**, 2473 (1977)
- [11] Seaton, M.J., Mon.Note.R.Astron.Soc., **A118**, 504 (1958)
- [12] Freeman, R., Kleppner, D., Phys.Rev.A, **14**, 1614 (1976)
- [13] Spruch, L., Kelsey, E., Phys.Rev.A. **18**, 1055 (1978)
- [14] Hatree, D., Proc.Cambridge.Philo.Soc., **25**, 310 (1929)
- [15] Ham, F., Solid State Phys., **1**, 127 (1955)
- [16] Seaton, M.J., Mon.Note.R.Astron.Soc., **A118**, 504 (1958)
- [17] Fabre, c., Haroche, S., Ref 6, chapter 4, 120-123
- [18] Bebb, H.B., Phys.Rev. **149**, 25 (1966)
- [19] Gounand, J.F., J.Physique(Paris), **40**, 457 (1979)

- [20] Fabre,C., Haroche,S., Chapter2, Ref 6 and the references there in.
- [21] Moors,C.E., 'Table of atomic energy Levels III', National Bureau of Standards, Circ 467 (1958)
- [22] Striganov,H., Sventiskii,N.S., 'Tables of Spectral Lines of neutral and ionized atoms', IFI/ Plenum Data Corp.NY (1968)
- [23] Kleiman,H., J.Opt.Soc.Am., 52, 441 (1962)
- [24] Popescu,D., Collins,C.B., Johnson, B.W., and Popsecu,I., Phys.Rev.A 9, 1182 (1974)
- [25] Bridges,W.B., J.Opt.Soc.Am., 68, 352 (1978)
- [26] Lorenzen,C.J., Webber,K.H., and Niemax,K., Opt.Comm., 33, 271 (1980)
- [27] Libberman,S., and Pinard,J., Phys.Rev.A, 20, 507 (1979)
- [28] Pendrill,L.R., Delande,D. and Goy,J.C., J.Phys, B12, L603 (1979)
- [29] Sansonetti,C.J., and Lorenzen,C.J., Phys.Rev.A, 30, 1805 (1984)
- [30] Mirza,M.Y. and Dulley,W.W., J.Phys., B11, 1917 (1978)
- [31] Ruff.G.A., Safinya, K.A., and Gallagher,T.F., Phys.Rev.A.,22, 183 (1980)
- [32] Sansonetti,C.J., and Andrew,K.L., J.Opt.Soc.Am., 71, 423 (1981)
- [33] Lorenzen,C.J. and Niemax,K., Z.Phys.A Atom & Mol. Phys. 311, 249 (1983)
- [34] Fredrison,K., Lundberg,H., and Svanberg,S., Z.Physik, A284, 429 (1978)
- [35] Pendrill,L.R., Physica Scripta, 27, 371 (1983)
- [36] Marr,G.V., and Creek,D.M., Proc. R. Soc. Lond., A304, 233 (1968)
- [37] Zalewski,E.F., Keller, R.A., and Engelman Jr.,R., J. Chem. Phys., 70, 1015, (1979)
- [38] Palmer,B.A., Emgleman,R.,Jr., 'Atlas of Thorium Spectrum', Appendix B, LA-9615, Los Almos National Laboratory Report, Los Almos, New Mexico, U.S.A., Issued: Feb. 1983.

8106275

PHN-1987-D-GOV-STU